Universitat Politècnica de Catalunya
Institut d'Estudis Espacials de Catalunya

Latest generation white dwarf cooling models: theory and applications

by

Isabel Renedo Rouco

A thesis submitted for the degree of

Doctor of Philosophy

Advisors:
Prof. Enrique García–Berro Montilla
Prof. Leandro G. Althaus

Barcelona, May 2014

Dedicat especialment als meus pares, al meu germà, a la Gemma i a l'àvia

Contents

Acknowledgements

I would like to thank all the people and institutions that have contributed to making this thesis possible. In particular, I would like to thank the Spanish Ministry of Education and Science, through a research training fellowship (*Formación del Profesorado Universitario*) and generous funding for international stages (in the United Kingdom and Argentina).

I wish to express my gratitude to my director, Prof. Dr. Enrique García–Berro Montilla, without whom this thesis would not exist, to my co-director, Prof. Dr. Leandro G. Althaus, for guiding me through the `LPCODE` code and through La Plata, and to both of them for their assistance, dedication, and patience. I have fond memories of our initial three-way meetings. They are great mentors, and their knowledge knows no bounds.

It has been a privilege to work at the Department de Física Aplicada of the Universitat Politècnica de Catalunya (UPC) and especially with the Astronomy and Astrophysics Group. I am particularly grateful to them for proving me with the opportunity to be a lecturer for undergraduate students. I am grateful for having the chance to stay at the Astrophysics Research Institute of the Liverpool John Moores University (LJMU), supervised by Prof. Dr. Maurizio Salaris, as well as the opportunity to stay at the Instituto de Astrofísica de La Plata of the Universidad Nacional de La Plata (UNLP), with the La Plata Stellar Evolution and Pulsation Research Group supervised by Prof. Leandro G. Althaus. I would also like to express my deepest recognition to Santiago Torres (UPC), to Maurizio Salaris (LJMU), Alejandro H. Córsico (UNLP), Marcelo M. Miller Bertolami (UNLP), and to Alejandra, Felipe, and Jorge (UNLP).

Thanks also to fellow students and colleagues with whom I shared office, corridors and smiles in Castelldefels, Birkenhead, and La Plata. Thanks also to all people who made my life easier abroad. Specially to Betty for her initial help and welcome in La Plata.

Finally, I wish to express my gratitude to my parents, my brother Jordi, my grandmother, Gemma, Toni, and Yolanda, and to all friends and family who encouraged me and gave me care and support.

List of Figures

List of Tables

Chapter 1

Introduction

White dwarfs are the most common stellar evolutionary end-point. As a matter of fact, more than 97% of all stars, including our Sun, are expected to ultimately end their lives passively, getting rid of their outer layers and forming white dwarfs. These stellar remnants are the cores of low- and intermediate-mass hydrogen burning stars, and have no appreciable sources of nuclear energy. Hence, as time passes by, white dwarfs will slowly cool and radiate the stored thermal energy, becoming dimmer and dimmer. Their evolution is a relatively well-understood process and can be basically described as a simple cooling process (Mestel, 1952) which lasts for very long periods of time in which the decrease in the thermal heat content of the ions constitutes the main source of luminosity.

Moreover, since these fossil stars are abundant and long-lived objects, they convey important information not only on the evolution of stars from birth to death but also about the properties of all Galactic populations (Hansen & Liebert, 2003). Thus, the study of white dwarfs has potential applications to different fields of astrophysics. In particular, white dwarfs can be used as independent reliable cosmic clocks, and can also provide valuable information about the fundamental parameters of a wide variety of stellar populations, like our Galaxy and open and globular clusters. For this reason, it is important to realize that an accurate determination of the rate at which white dwarfs cool down constitutes a fundamental issue. Detailed evolutionary models for these stars, based on increasing degrees of sophistication of their constitutive physics and energy sources, have proved to be valuable at determining interesting properties of many Galactic populations, including the disk (Winget et al., 1987; Garcia-Berro et al., 1988a,b; Hernanz et al., 1994; García-Berro et al., 1999), the halo (Isern et al., 1998; Torres et al., 2002) and globular and open clusters (Kalirai et al., 2001; Richer et al., 1997; von Hippel & Gilmore, 2000; Hansen et al., 2002, 2007; von Hippel et al., 2006; Winget et al., 2009). This important application of white dwarf stars has also been possible thanks to a parallel effort devoted to the empirical determination of the observed white dwarf cooling sequences in stellar

clusters, as well as the determination of the luminosity function of field white dwarfs, which also provides a measure of the white dwarf cooling rate. They also provide helpful information about the past history of the star formation rate of our Galaxy (Diaz-Pinto et al., 1994).

In addition, the high densities and temperatures characterizing white dwarfs allow to use these stars as cosmic laboratories for studying physical processes under extreme conditions that cannot be achieved in terrestrial laboratories. Last but not least, since many white dwarf stars undergo pulsational instabilities, the study of their properties constitutes a powerful tool for applications beyond stellar astrophysics. In particular, white dwarfs can be used to constrain fundamental properties of elementary particles such as axions and neutrinos (Isern et al., 1992; Córsico et al., 2001a; Isern et al., 2008), and to study problems related to the variation of fundamental constants (Garcia-Berro et al., 1995; Benvenuto et al., 2004). Recent reviews on the properties and evolution of white dwarfs and of their applications are those of Althaus et al. (2010b), Winget & Kepler (2008) and Fontaine & Brassard (2008).

1.1 Basic properties of white dwarf stars

Most white dwarfs stars begin their evolution as nuclei of planetary nebulae, and are the products of intermediate- and low-mass main sequence star evolution. Namely, they are the descendants of stars with initial masses less than about $10 \pm 2\,M_{\odot}$ (Ritossa et al., 1999; Siess, 2007). Most of the mass of a typical white dwarf is contained in its core, which is made of the products of He burning, mostly carbon and oxygen. Small amounts of H and He are left over after the mass-loss phases have ended. Taking into account the previous thermonuclear history and the efficiency of gravitational settling, it is expected that the structure of a typical white dwarf corresponds to that of a compositionally stratified object with a mass of about $0.6\,M_{\odot}$ consisting of a carbon-oxygen core surrounded by a thin, He-rich envelope — of at most $0.01\,M_{\odot}$ — surrounded itself by a thinner H-rich layer of $\sim 10^{-4}\,M_{\odot}$. Although very thin, the outer layers are extremely opaque to radiation and regulate the energy outflow of the star, thus playing a crucial role in the evolution of a white dwarf.

Comparing the limit of progenitor masses with the mass distribution on the main sequence at birth, this means that certainly more than 95% of all stars will become white dwarfs. Typically, an $8\,M_{\odot}$ progenitor leads to a remnant of $\sim 1\,M_{\odot}$ and a $1\,M_{\odot}$ star to one of about $0.5\,M_{\odot}$. Because the exceedingly large time required for a low-mass main sequence star (less than $0.8\,M_{\odot}$) to become a white dwarf, most white dwarfs with stellar masses smaller than $0.4\,M_{\odot}$ are expected not to be the result of single stellar evolution, but instead, the result of mass transfer in binary systems. The fact that the maximum mass of a white dwarf is about $1.4\,M_{\odot}$ — the Chandrasekhar limiting mass — hints at the occurrence of strong mass loss during the progenitor star evolution.

White dwarfs span a wide range of both effective temperatures and luminosities. Values of $T_{\rm eff}$ range from about 150 000 K for the hottest members to 4 000 K for the coolest degenerate dwarfs. The stellar luminosity ranges from roughly 10^3 to about $10^{-5}\ L_\odot$ for the faintest observed white dwarfs. The majority of known white dwarfs have temperatures higher than the Sun and hence the "white" in their name. Because the intrinsic faintness of most white dwarfs, quantitative studies of these stars, traditionally based on photometric and spectroscopic observations, are restricted to nearby objects. Hence, the vast majority of observed white dwarfs are representative of the solar neighborhood. Other observational techniques and the advent of large-scale ground-based surveys and deep Hubble Space Telescope exposures, have revealed the presence of white dwarf populations located well beyond our own neighborhood, such as in distant open and globular clusters and, most probably, in the Galactic halo, thus enabling us to extract information and to constrain the properties of such populations.

1.1.1 Stellar evolution

After the main sequence phase, the long-lived stage of central H burning, the progenitor star evolves to the red giant phase to burn He in its core. In this phase the carbon-oxygen core composition that will characterize the emerging white dwarf remnant is built up. After the end of core He burning, evolution proceeds to the Asymptotic Giant Branch (AGB). There, the He burning shell becomes unstable and the star undergoes recurrent thermal instabilities commonly referred to as *thermal pulses*. As evolution proceeds along the AGB, the mass of the carbon-oxygen core increases considerably by virtue of the outward-moving He burning shell. Also, during this stage most of the remaining H-rich envelope is ejected through very strong mass-loss episodes. When the mass fraction of the remaining envelope is reduced to $\sim 10^{-3}\,M_\odot$ the remnant star moves rapidly to the left in the Hertzsprung-Russell diagram to the domain of the planetary nebulae. If the departure from the AGB takes place at an advanced stage in the He shell flash cycle, the post-AGB remnant may experience a last He thermal pulse on its early cooling branch, and eventually totally exhausts its residual H content, thus giving rise to a H-deficient white dwarf (see below). When the remaining H envelope is reduced to $\sim 10^{-4}\,M_\odot$, nuclear energy generation becomes virtually extinct. The surface luminosity decreases rapidly, and the star enters the terminal phase of its life as a white dwarf. The newly formed white dwarf is left mostly with only gravitational and thermal energy sources available. In fact, during most of its final evolution, the gravothermal (gravitational plus thermal energy) contribution drives the evolution. Since electrons are already degenerate in the interior, the stellar radius is not far from the equilibrium radius of the zero-temperature model, and the remaining contraction is small, but not entirely negligible. Hence, the star evolves almost at constant radius along a diagonal straight line in the white dwarf region of the Hertzsprung-Russell diagram.

1.1.2 Mass distribution

Studying mass distribution of white dwarfs is possible to constrain the late stages of stellar evolution since it reveals the amount of mass lost during the lifetime of the star from the main sequence (Liebert et al., 2005). The surface gravities and effective temperatures of white dwarfs are usually determined from model atmosphere fits to spectral lines. On average, it turns out that white dwarfs are characterized by surface gravities $\log g \simeq 8$. Coupled with theoretical mass-radius relations, this yields average masses of $M \approx 0.6\,M_{\odot}$. Typical white dwarf mass distributions show that the values of the masses of most white dwarfs cluster around this value (Kepler et al., 2007), with a tail extending towards high stellar masses. The rather narrow mass distribution of white dwarfs is a remarkable characteristic of these stars. Massive white dwarfs have spectroscopically determined masses within 1.0 and $1.3\,M_{\odot}$ and are believed to harbor cores composed mainly of oxygen and neon — at least for non-rotating stars (Dominguez et al., 1996; Ritossa et al., 1996) — in contrast to average-mass white dwarfs, for which carbon-oxygen cores are expected. The existence of such massive white dwarfs has been suggested to be the result of the merger of two averaged-mass white dwarfs in close binaries (Guerrero et al., 2004; Lorén-Aguilar et al., 2009) or of the evolution of heavy-weight intermediate-mass single stars that have experienced repeated carbon-burning shell flashes (Ritossa et al., 1999). Finally, the white dwarf mass distribution comprises a population of low-mass remnants. Because low-mass progenitors would need exceedingly large ages to reach the white dwarf stage, these low-mass white dwarfs are mostly produced in binary systems, where the stellar evolution has been truncated by mass transfer (Sarna et al., 1999).

1.1.3 Spectroscopic classification

White dwarfs have been classified into two distinct families according to the main constituent of their surface. Most white dwarfs surface composition consists almost entirely of H with at most traces of other elements. These are the so-called DA white dwarfs and they comprise about 85% of all white dwarfs (see Eisenstein et al. (2006) and references therein). To the other family belong the H-deficient white dwarfs with He-rich atmospheres, usually known as non-DA white dwarfs, which make up to almost 15% of the total population. H-deficient white dwarfs are thought to be the result of late thermal flashes experienced by post-AGB progenitors or of merger episodes. The non-DA white dwarfs are usually divided into several different subclasses: the DO spectral type (with effective temperatures $45\,000\ \mathrm{K} \leq T_{\mathrm{eff}} \leq 200\,000\ \mathrm{K}$) that shows relatively strong lines of singly ionized He (HeII), the DB type ($11\,000\ \mathrm{K} \leq T_{\mathrm{eff}} \leq 30\,000\ \mathrm{K}$), with strong neutral He (HeI) lines, and the DC, DQ, and DZ types ($T_{\mathrm{eff}} < 11\,000\ \mathrm{K}$) showing traces of carbon and metals in their spectra. As a DO white dwarf evolves, the HeII recombines to form HeI, ultimately transforming into a DB white dwarf. The transition from DO to the cooler DB

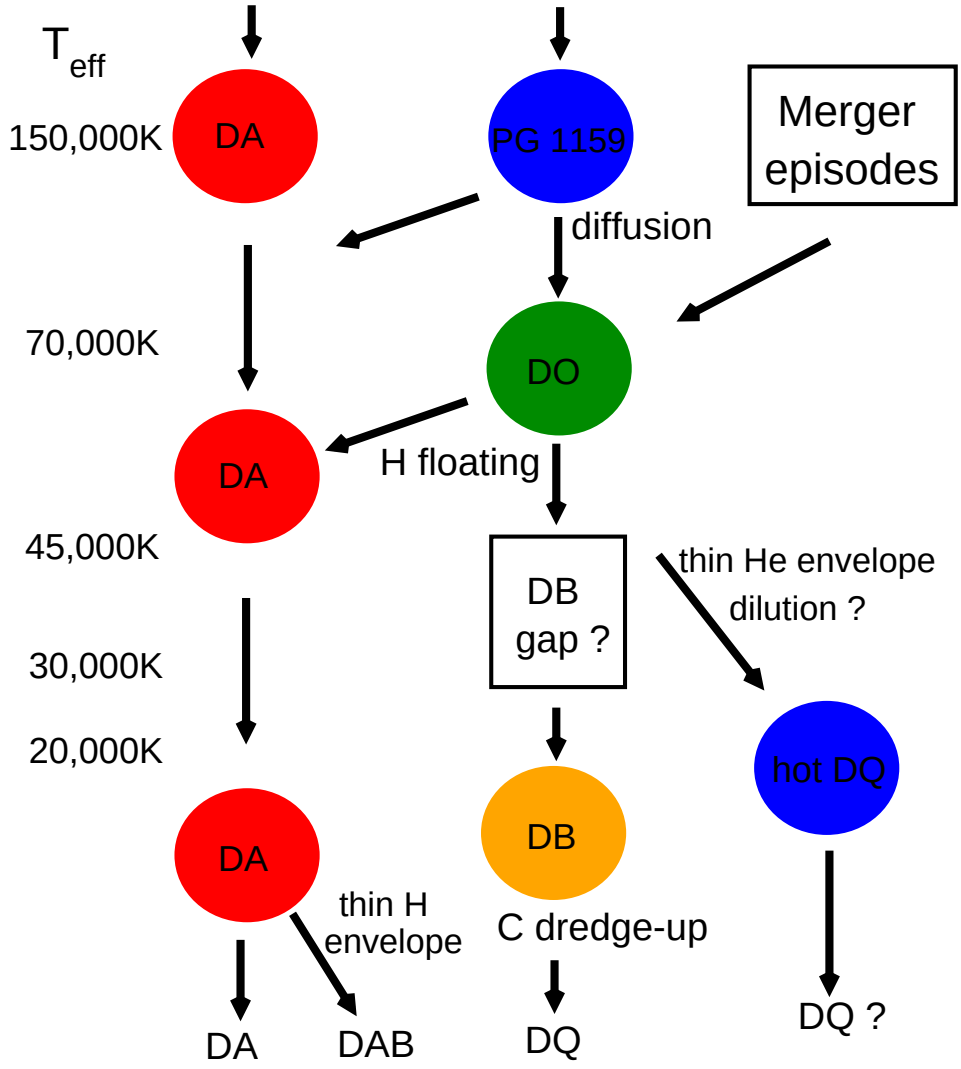

Figure 1.1: A scheme of the several evolutionary paths that hot white dwarfs may follow as they evolve. The left column gives the effective temperature. Most white dwarfs are formed with H-rich envelopes (DA spectral type), and remain as such throughout their entire evolution (second column). H-deficient white dwarfs like DOs may follow different paths, either from the hot and He-, carbon-, and oxygen-rich PG 1159 stars or from post-merger events. Traces of H in PG 1159s and DOs may lead to other white dwarf varieties. PG 1159 stars are also believed to be the predecesors of the recently discovered new class of white dwarfs: the hot DQs, with carbon-rich atmospheres. Accretion of metals by cool He-rich white dwarfs from interstellar medium or from circumstellar matter may lead to DZ white dwarfs. From Althaus et al. (2010b)

stage is interrupted by the non-DA gap (that occurs at 30 000 K $< T_{\rm eff} <$ 45 000 K) where few objects with H-deficient atmospheres have been observed Eisenstein et al. (2006). To this list, we have to add those white dwarfs with hybrid atmospheres or peculiar abundances, and the recent discovery of a new white dwarf spectral type with carbon-dominated atmospheres, the "hot DQ" white dwarfs, with $T_{\rm eff} \sim 20\,000$ K (Dufour et al., 2007, 2008). Hot DQ white dwarfs are thought to be the cooler descendants of some PG 1159 stars, and the result of convective mixing at smaller effective temperatures (Dufour et al., 2008; Althaus et al., 2009b)).

Although this classification is in line with our understanding that most giant stars will evolve into white dwarfs with either H-rich atmospheres or H-deficient composition, the existence of some of these white dwarfs poses a real challenge to the theory of stellar evolution, which cannot adequately explain their origin. Finally, there is ample observational evidence that individual white dwarfs undergo spectral evolution, i.e., the surface composition of a given white dwarf may change as it evolves as a result of competing processes such as convection, mass-loss episodes, accretion, radiative levitation and gravitational settling. The interplay between these processes may help to understand the different evolutionary paths that white dwarfs may follow as the surface temperature decreases, see Fig. 1.1. For instance, the empirical evidence that the ratio of DA to non-DA white dwarfs changes with effective temperature and the existence of the non-DA gap are interpreted as the result of changes in the surface composition from He-dominated to H-dominated and vice versa as evolution proceeds. Also, the presence of traces of H in the outer layers of the hot H-deficient white dwarfs like PG 1159s or DOs can turn the spectral type of these white dwarfs into that of a DA type as a result of gravitational settling.

1.1.4 ZZ Ceti stars

Pulsating DA (H-rich atmospheres) white dwarfs, also called ZZ Ceti or DAV stars, are the most numerous class of degenerate pulsators, with over 143 members known today (Winget & Kepler, 2008). Since the discovery of the first ZZ Ceti star, HL Tau 76, by Landolt (1968), there has been a continuous effort to model the interior of these variable stars. ZZ Ceti stars are found within a very narrow strip of effective temperatures (10 500 K $\lesssim T_{\rm eff} \lesssim$ 12 500 K). They are characterized by multiperiodic brightness variations of up to 0.30 mag caused by spheroidal, non-radial g-modes of low degree ($\ell \leq 2$) with periods between 100 and 1200 s. The driving mechanism thought to excite the pulsations near the blue edge of the instability strip is the $\kappa - \gamma$ mechanism that takes place in the hydrogen partial ionization zone (Dolez & Vauclair, 1981) bib:DziembowskiKoester1981, Winget et al. (1982). Also, the "convective driving" mechanism has been proposed — first by Brickhill (1991) and later re-examined by Goldreich & Wu (1999). It appears to be the responsible of mode driving once a thick convection zone has developed at the stellar surface.

The comparison of the observed pulsation periods in white dwarfs and the periods

computed for appropriate theoretical models (white dwarf asteroseismology) allows to infer details of their origin, internal structure and evolution (Winget & Kepler, 2008; Fontaine & Brassard, 2008). In particular, the stellar mass, the thickness of the outer envelopes, the core chemical composition, magnetic fields and rotation rates can be determined from the observed periods. In addition, the asteroseismology of ZZ Ceti stars is a valuable tool for studying axions (Isern et al., 1992; Córsico et al., 2001a; Bischoff-Kim et al., 2008; Isern et al., 2010) and the physics of crystallization (Montgomery et al., 1999; Córsico et al., 2004, 2005; Metcalfe et al., 2004; Kanaan et al., 2005). Finally, the temporal changes in the observed periods can help detect planets orbiting around white dwarfs (Mullally et al., 2008).

The first published complete set of DA white dwarf models suitable for asteroseismology was that of Tassoul et al. (1990). A large parameter space was explored in such a monumental study, and for a long time (since the early eighties) this set of models represented the state-of-the-art in the area. The pulsation properties of these models were thoroughly explored in a series of important papers by Brassard et al. (1991), Brassard et al. (1992a), and Brassard et al. (1992b). As important as these models were at that time, they suffer from a number of shortcomings. For instance, the core of the models is made of pure carbon, while stellar evolution calculations indicate that cores of typical white dwarfs are made of a mixture of carbon and oxygen. Also, the carbon/helium (C/He) and helium/hydrogen (He/H) chemical interfaces are modeled on the basis of the assumption of the diffusive equilibrium in the "trace element approximation", an approach that involves a quasi-discontinuity in the chemical profiles at the transition regions which, in turn, leads to peaked features in the Brunt-Väisälä frequency and exaggerated mode-trapping effects (Córsico et al., 2002b,a). These models were employed for asteroseismological inferences of the DAVs G 226−29 (Fontaine et al., 1992) and GD 154 (Pfeiffer et al., 1996). More recently, Pech et al. (2006) and Pech & Vauclair (2006) have presented asteroseismological analysis on HL Tau 76 and G 185−32, respectively, by employing similar DA white dwarf models, although with updated input physics.

The models of Bradley (1996) constituted a substantial improvement in the field. These models have carbon-oxygen cores in varying proportions, and the C/He and He/H chemical interfaces are more realistic. Perhaps the most severe shortcoming of these models is the (unrealistic) ramp-like shape of the core carbon-oxygen chemical profiles. These DA models were the basis of the very important asteroseismological studies on the DAVs G 29−38 (Bradley & Kleinman, 1997), G 117−B15A and R 548 Bradley (1998), GD 165 and L 19−2 Bradley (2001), and G 185−32 Bradley (2006).

The next step in improving the modeling of DAVs was given by Córsico et al. (2002a) and Benvenuto et al. (2002b), who employed evolutionary models characterized by He/H chemical interfaces resulting from a time-dependent element diffusion treatment (Althaus & Benvenuto, 2000), and the carbon-oxygen core chemical structure extracted from the evolutionary computations of Salaris et al. (1997). The use of very smooth outer chemical interfaces, as shaped by chemical diffusion, revealed

that the use of the trace element approximation turns out to be inappropriate to model the shape of the chemical interfaces in a DA white dwarf. This grid of models was employed in an asteroseismological study of G 117−B15A (Benvenuto et al., 2002b). For these sequences, the starting configurations for the white dwarf evolution were obtained through an artificial procedure, and not as result of evolutionary computations of the progenitor stars.

Recently, Castanheira & Kepler (2008) and Castanheira & Kepler (2009) have carried out an extensive asteroseismological study of DAVs by employing DA white dwarf models similar to those of Bradley (1996), but with a simplified treatment of the core chemical structure, by somewhat arbitrarily fixing the central abundances to 50% oxygen and 50% carbon. The He/H chemical interfaces adopted for these models are a parametrization of the realistic chemical profiles resulting from time-dependent element diffusion (Althaus et al., 2003). The study includes the "classical" DAVs and also the recently discovered Sloan Digital Sky Survey DAVs. In total, 83 ZZ Ceti stars are analyzed. An important result of these studies is that the thickness of the H envelopes inferred from asteroseismology is in the range $10^{-4} \gtrsim M_{\rm H}/M_* \gtrsim 10^{-10}$, with a mean value of $M_{\rm H}/M_* = 5 \times 10^{-7}$. This suggests that an important fraction of DAs characterized by envelopes substantially thinner than predicted by the standard evolution theory could exist, with the consequent important implications for the theory of white dwarf formation. However, these results are preliminary and do not include the possible effects of realistic carbon-oxygen profiles on the asteroseismological fits.

Almost simultaneously with the studies of Castanheira & Kepler (2008) and Castanheira & Kepler (2009), Bischoff-Kim et al. (2008) performed a new asteroseismological study on G 117−B15A and R 548 by employing DA white dwarf models similar to those employed by Castanheira & Kepler (2008) and Castanheira & Kepler (2009), but incorporating realistic core chemical profiles according to Salaris et al. (1997). The results of this work are in reasonable agreement with previous studies on these ZZ Ceti stars. However, the mass and effective temperatures found by Bischoff-Kim et al. (2008) for G 117−B15A are rather high (especially the mass, at $0.66\,M_\odot$). Recently, Bognár et al. (2009) have employed the same asteroseismological modeling to study the pulsations of the ZZ Ceti star KUV 02464+3239. Finally, Bischoff-Kim (2009) presented the results of an asteroseismological analysis of two DAVs with rich pulsation spectrum, G 38−29 and R 808 based on similar models, with parametrized, smooth ramp-like core profiles. These models are able to reproduce the observed period spectra reasonably well, though some assumptions about the m and ℓ identification of modes were made.

White dwarf stellar models with realistic chemical profiles are crucial to correctly assess the adiabatic period spectrum and mode-trapping properties of the DAVs, which lies at the core of white dwarf asteroseismology (Brassard et al., 1992a; Bradley, 1996; Córsico et al., 2002b).

1.2 Thesis objectives and outline

This thesis is focused on the study of cooling white dwarf models with two different angles. From a theoretical perspective, we computed new theoretical evolutionary cooling sequences for white dwarfs appropriate for precision white dwarf cosmochronology and for asteroseismological studies of ZZ Ceti stars. Moreover, we studied the role of ^{22}Ne diffusion on the evolution of white dwarf stars with high-metallicity progenitors. We employed the `LPCODE` evolutionary code, based on detailed and updated constitutive physics. Our evolutionary sequences have been self-consistently evolved from the zero age main sequence, through the core hydrogen and helium burning evolutionary phases to the thermally pulsing asymptotic giant branch and, ultimately, to the white dwarf stage. We want to mention that detailed non-gray model atmospheres are used to derive the outer boundary condition for the evolving sequences.

This work is organized as follows. First we elaborate on the theoretical approach. This is done in chapter 2 where we explain how we model evolutionary cooling sequences for hydrogen-rich DA white dwarfs. We adopt two different metallicities, a metallicity typical of most Galactic globular clusters, $Z = 0.001$, thus allowing to obtain accurate ages for metal-poor stellar systems. We also compute sequences for a metallicity representative of the solar neighborhood, $Z = 0.01$, which allows us to obtain accurate ages for white dwarfs in the local Galactic disk. To the best of our knowledge, this is the first set of self-consistent evolutionary sequences covering different initial masses and metallicities. In chapter 3 we produce a set of new chemical profiles for the core and envelope of white dwarfs which are intentd for asteroseismological studies of ZZ Ceti stars that require realistic chemical profiles throughout the white dwarf interiors, these profiles were derived from the full and complete evolution of progenitor stars (see chapter 2) with Solar metallicity from the zero age main sequence, through the thermally-pulsing and mass-loss phases on the asymptotic giant branch (AGB). Extra-mixing episodes during central hydrogen and helium burning, time-dependent element diffusion during the white dwarf stage and chemical rehomogenization of the inner carbon-oxygen composition by Rayleigh-Taylor instabilities were considered. In chapter 4 we present a grid of white dwarf evolutionary sequences with high-metallicity progenitors that incorporates for the first time the energy contributions arising from both ^{22}Ne sedimentation and carbon-oxygen phase separation.

From an applied point of view, in chapters 5 and 6 we use observations of the white-dwarf cooling sequences to constrain important properties of the cluster stellar population, such as the age, the existence of a putative population of massive helium-core white dwarfs, and the properties of a large population of unresolved binary white dwarfs. We also investigate the use of white dwarfs to disclose the presence of cluster subpopulations with a different initial chemical composition, and we obtain an upper bound to the fraction of hydrogen-deficient white dwarfs. We presented our results

for NGC 6791, a well studied metal-rich open cluster (Bedin et al., 2005) that it is so close to us that can be imaged down to luminosities fainter than that of the termination of its white-dwarf cooling sequence (Bedin et al., 2008a), thus allowing for an in-depth study of its white dwarf population. This is done using a Monte Carlo simulator that employs our up-to-date evolutionary cooling sequences for white dwarfs with hydrogen-rich and hydrogen-deficient atmospheres, with carbon-oxygen and helium cores. The cooling sequences for carbon-oxygen cores account for the delays introduced by both ^{22}Ne sedimentation in the liquid phase and by carbon-oxygen phase separation upon crystallization. The final chapter (chapter 7) summarizes the main contributions of the present work.

Chapter 2

Evolutionary cooling sequences for hydrogen-rich DA white dwarfs

In this chapter, we present full evolutionary calculations appropriate for the study of hydrogen-rich DA white dwarfs. This is done by evolving white dwarf progenitors from the zero age main sequence, through the core hydrogen burning phase, the helium burning phase and the thermally pulsing asymptotic giant branch phase to the white dwarf stage. Complete evolutionary sequences are computed for a wide range of stellar masses and for two different metallicities: $Z = 0.01$, which is representative of the solar neighborhood, and $Z = 0.001$, which is appropriate for the study of old stellar systems, like globular clusters. During the white dwarf cooling stage we compute self-consistently the phase in which nuclear reactions are still important, the diffusive evolution of the elements in the outer layers and, finally, we also take into account all the relevant energy sources in the deep interior of the white dwarf, like the release of latent heat and the release of gravitational energy due to carbon-oxygen phase separation upon crystallization. We also provide colors and magnitudes for these sequences, based on a new set of improved non-gray white dwarf model atmospheres, which include the most up-to-date physical inputs like the Lyα quasi-molecular opacity. The calculations are extended down to an effective temperature of 2 500 K. Our calculations provide a homogeneous set of evolutionary cooling tracks appropriate for mass and age determinations of old DA white dwarfs and for white dwarf cosmochronology of the different Galactic populations.

2.1 Introduction

Previous recent evolutionary calculations of hydrogen-rich white dwarfs are those of Fontaine et al. (2001), Salaris et al. (1997), Salaris et al. (2000), Hansen (1998),

Hansen (1999), Benvenuto & Althaus (1999), Wood (1992), and Wood (1995). All these works have studied different aspects of the evolution of white dwarfs with hydrogen-rich envelopes. For instance, the most commonly used models, those of Wood (1995), cover a wide range of stellar masses and envelope masses and, until recently, were considered to be a standard reference in the field of white dwarf cosmochronology. However, we emphasize that these models were computed using gray atmospheres, a severe drawback (especially at low luminosities) that more recent calculations have overcome. Among these models we mention the works of Hansen (1998) and Hansen (1999). This set of cooling models pioneered the usage of detailed model atmospheres as surface boundary conditions in cooling calculations for old white dwarfs. This is an important issue since it affects the location of the base of the convective envelope. These calculations also showed that collision-induced absorption processes affect the colors of old white dwarfs. Salaris et al. (1997) and Salaris et al. (2000) focused on the question of the interior abundances of carbon and oxygen, which is of critical importance to derive reliable ages and on the effects of phase separation of carbon and oxygen upon crystallization, while Fontaine et al. (2001) were the firsts to discover the importance of convective coupling between the atmosphere and the degenerate core. This last issue also bears importance for the determination of accurate ages. Nevertheless, all these works suffer from the same shortcoming. All of them evolved intial white dwarf configurations which were not obtained self-consistently from models evolving from the main-sequence. As a consequence, the chemical stratification of the inner, degenerate core was simplistic in most of the cases, except in the case of the cooling sequences of Salaris et al. (1997) and Salaris et al. (2000). Also, the envelope mass and the outer layer chemical distribution were idealized ones in all the cases. Additionally, the oldest sequences used physical inputs which are nowadays outdated and, finally, most of them disregarded the energy release of carbon-oxygen phase separation (Garcia-Berro et al., 1988b,a).

The aim of this chapter is to compute a set of new cooling sequences for hydrogen-rich white dwarfs, incorporating the most up-to-date physical inputs. We emphasize that our evolutionary sequences are derived from a full and self-consistent treatment of the complete evolutionary history of progenitor stars with different masses evolved with two different metallicities ($Z = 0.01$ and $Z = 0.001$) appropriate for the study of the solar neighborhood and of metal-poor stellar systems, like globular clusters or the galactic halo. Thus, our calculations constitute a comprehensive set of evolutionary tracks which allow to study the evolution of hydrogen-rich white dwarfs in a wide variety of stellar systems. Moreover, since our calculations encompass the pre-white dwarf evolutionary phases, the white dwarf evolutionary calculations presented here are not affected by inconsistencies arising from artificial procedures to generate starting white dwarf configurations. In particular, the calculation of the evolutionary history of progenitor stars provides us with the amount of H left in the white dwarf, and with the chemical profiles expected not only for the carbon-oxygen core, but also for the partially degenerate regions above the core, of relevance for

the white dwarf cooling phase.

The chapter is organized as follows. In Sect. 2.2 we describe the main physical inputs of our models. We also describe the main characteristics of the initial models, the model atmospheres employed in this work and some details of the evolutionary computations. In Sect. 2.3 we present the results of the pre-white dwarf evolutionary sequences, paying special attention to the derived initial-to-final-mass relationship, and also the white dwarf cooling tracks. In this section we also discuss in detail the effects of phase separation upon crystallization. Finally, in Sect. 2.4 we summarize our results, we discuss their significance and we draw our conclusions.

2.2 Computational details

2.2.1 Input physics

The evolutionary calculations presented in this work were done with an updated version of the LPCODE stellar evolutionary code — see A.1 as well as Althaus et al. (2003) and Althaus et al. (2005c). We used this code to compute both the evolution of white dwarfs and that of their progenitor stars. LPCODE is able to follow the complete evolution of the star model from the main sequence through the core helium flash and, finally, for many thermal pulses on the AGB almost without hand intervention, except for the latest stages of the TP-AGB phase of the more massive sequences, where numerical instabilities arise. These instabilities, also found by other authors, are the result of the large radiation pressure in the convective envelope. To circumvent them, we found computationally convenient to artificially modify the opacity profile in those regions close to the base of the convective envelope. This procedure bears no relevance for the evolution during the white dwarf regime. In what follows, we only comment on the main physical input physics, namely, those that are relevant for the evolutionary calculations presented in this chapter.

Our cooling sequences have been computed taking into account reliable initial configurations, with the appropriate inner chemical profiles resulting from the previous evolution of the progenitor stars and also realistic thicknesses of the helium and hydrogen layers. We also incorporate the release of nuclear energy from residual hydrogen and helium burning during the early phases of the evolution of the white dwarf. Chemical diffusion in the outer layers is included in a realistic way. Finally, at very low luminosities, when the inner regions of the white dwarf crystallize we include not only the release of latent heat but also the release of gravitational energy (Isern et al., 1997, 2000) resulting from carbon-oxygen phase separation (Garcia-Berro et al., 1988b; Segretain et al., 1994).

2.2.2 Model atmospheres

A proper treatment of the evolutionary behavior of cool white dwarfs requires the use of outer boundary conditions as provided by detailed non-gray model atmospheres. To this end, we considered model atmospheres that incorporate non-ideal effects in the gas equation of state and chemical equilibrium, collision-induced absorption from molecules, and the Lyα quasi-molecular opacity. Specifically, for $T_{\rm eff} < 10\,000$ K, we derived starting values of the pressure, temperature, radial thickness and outer mass fraction at an optical depth $\tau = 25$ from a grid of non-gray model atmospheres which covers a surface gravity range between $\log g = 6.5$ and 9. For larger values of τ, the use of Rosseland mean opacities is justified, and the diffusion approximation for the radiative transfer can be assumed. The use of non-gray model atmospheres to derive outer boundary conditions gives rise to shallower outer convection zones, as compared with the standard gray treatment of the atmosphere (Bergeron et al., 1997). At advanced stages of white dwarf evolution, the central temperature becomes strongly tied to the temperature stratification of the outer layers. Thus, using non-gray model atmospheres is highly desired for an accurate assessment of cooling times of cool white dwarfs (Prada Moroni & Straniero, 2007).

In the present work, model atmospheres were specifically computed on the basis of improved LTE model atmospheres. Colors and magnitudes were evaluated for effective temperatures lower than 60 000 K, because NLTE effects become important above this temperature. Calculations were done for a pure hydrogen composition and for the HST ACS filters (Vega-mag system) and $UBVRI$ photometry. The numerical code used is a new and updated version of the one described in Rohrmann et al. (2002). Models were computed assuming hydrostatic and radiative-convective equilibrium. Convective transport present in the cooler atmospheres was treated within the usual mixing-length (ML2) approximation, adopting the same value of α used in the evolutionary calculations. The microphysics included in the model atmospheres comprises non-ideal effects in the gas equation of state and chemical equilibrium based on the occupation probability formalism as described in Rohrmann et al. (2002). The code includes H, H_2, H^+, H^-, H_2^+, H_3^+, He, He^-, He^+, He^{2+}, He_2^+, HeH^+, and e^-. The level occupation probabilities are self-consistently incorporated in the calculation of the line and continuum opacities. Collision-induced absorptions due to H_2-H_2, H_2-He, and H-He pairs are also taken into account (Rohrmann et al., 2002).

For the purpose of the present work, the model atmospheres explicitly included the Lyα quasi-molecular opacity according to the approximation used by Kowalski & Saumon (2006). Quasi-molecular absorption results from perturbations of hydrogen atoms by interactions with other particles, mainly H and H_2. Here, we considered extreme pressure-broadening of the line transition H($n = 1$)$\rightarrow$H($n = 2$) due to H-H and H-H_2 collisions, with the red wing extending far into the optical region. On the basis of the approximations outlined in Kowalski & Saumon (2006),

we evaluated the red wing absorption within the quasi-static approach using theoretical molecular potentials to describe the interaction between the radiator and the perturber. We also considered the variation in the electric-dipole transition moment with the interparticle distance. The H_3 energy-potential surfaces contributing to collisions H-H_2 were taken from Kulander & Guest (1979) and Roach & Kuntz (1986), and the dipole transition moments were calculated from Petsalakis et al. (1988). Broadening of Lyα line by H–H collisions plays a minor role compared to H–H_2 encounters. The potential interactions for H–H configurations were taken from Kołos & Wolniewicz (1965) and the transition probability was assumed constant in this case. The main effect of the Lyα quasi-molecular opacity is a reduction of the predicted flux at wavelength smaller than 4 000 Å for white dwarfs cooler than $T_{\rm eff} \approx 6\,000$ K.

2.2.3 Initial models

The initial models for our white dwarf sequences correspond to stellar configurations derived from the full evolutionary calculations of their progenitor stars. The initial He content of our starting models at the main sequence were provided by the relation $Y = 0.23+2.41Z$, as given by present determinations of the chemical evolution of the Galaxy (Flynn, 2004; Casagrande et al., 2007). Two metallicities for the progenitor stars were considered: $Z = 0.01$ and 0.001. Hence, the initial compositions of our sequences are, respectively, $(Y, Z) = (0.254, 0.01)$ and $(Y, Z) = (0.232, 0.001)$. All the sequences were evolved from the ZAMS through the thermally-pulsing and mass-loss phases on the AGB and, finally, to the white dwarf cooling phase. Specifically, we computed 10 full evolutionary sequences for $Z = 0.01$ and six for $Z = 0.001$. In Table 2.1, we list the initial masses of the progenitor stars at the ZAMS, together with other evolutionary quantities which will be discussed below.

2.3 Evolutionary results

2.3.1 From the ZAMS to the white dwarf stage

The evolution in the Hertzsprung-Russell diagram of our sequences from the ZAMS to advances stages of white dwarf evolution is shown in Fig. 2.1, for the case in which $Z = 0.01$ is adopted. Note that the less massive sequence experiences a hydrogen subflash before entering its final cooling track. The initial masses at the ZAMS and the final white dwarf masses of these sequences can be found in Table 2.1, for both metallicities. In this table we also list the main-sequence lifetimes, which, as well known, for solar-metallicity sequences are larger than those of their metal-poor counterparts. We mention that our models have main-sequence lifetimes longer than those recently published by Weiss & Ferguson (2009). Differences are less than 8% however, except for the main-sequence lifetime of the solar sequence, which is 25% larger. One of the reasons for such a discrepancy is due to our simplified treatment of

Table 2.1: Initial and final stellar mass (in solar units), total masses of H and He left in the white dwarf (in solar units), main-sequence lifetimes (in Gyr), mass lost on the AGB and number of thermal pulses on the AGB for the two metallicities studied here.

	$Z = 0.01$						$Z = 0.001$					
$M_{\rm ZAMS}$	$M_{\rm WD}$	$\log M_{\rm H}$	$\log M_{\rm He}$	$t_{\rm MS}$	$\Delta M_{\rm AGB}$	$N_{\rm TP}$	$M_{\rm WD}$	$\log M_{\rm H}$	$\log M_{\rm He}$	$t_{\rm MS}$	$\Delta M_{\rm AGB}$	$N_{\rm TP}$
0.85	—	—	—	—	—	—	0.505	−3.441	−1.567	11.885	−0.016	2
1.00	0.525	−3.586	−1.589	9.040	−0.104	5	0.553	−3.577	−1.635	6.406	−0.213	3
1.25	—	—	—	—	—	—	0.593	−3.777	−1.840	2.781	−0.499	7
1.50	0.570	−3.839	−1.703	2.236	−0.795	7	0.627	−4.091	−2.010	1.558	−0.757	10
1.75	0.593	−3.950	−1.851	1.444	−1.081	10	0.660	−4.174	−1.936	1.049	−1.012	12
2.00	0.609	−4.054	−1.826	0.974	−1.357	15	0.693	−4.195	−2.125	0.735	−1.272	18
2.25	0.632	−4.143	−1.957	0.713	−1.601	22	—	—	—	—	—	—
2.50	0.659	−4.244	−2.098	0.543	−1.825	21	—	—	—	—	—	—
3.00	0.705	−4.400	−2.270	0.341	−2.279	19	0.864	−4.860	−2.496	0.279	−2.02	34
3.50	0.767	−4.631	−2.376	0.232	−2.688	15	—	—	—	—	—	—
4.00	0.837	−4.864	−2.575	0.166	−3.104	17	—	—	—	—	—	—
5.00	0.878	−4.930	−2.644	0.099	−4.029	12	—	—	—	—	—	—

The mass of the hydrogen and helium contents is given at the point of maximum effective temperature at the beginning of the white dwarf cooling branch

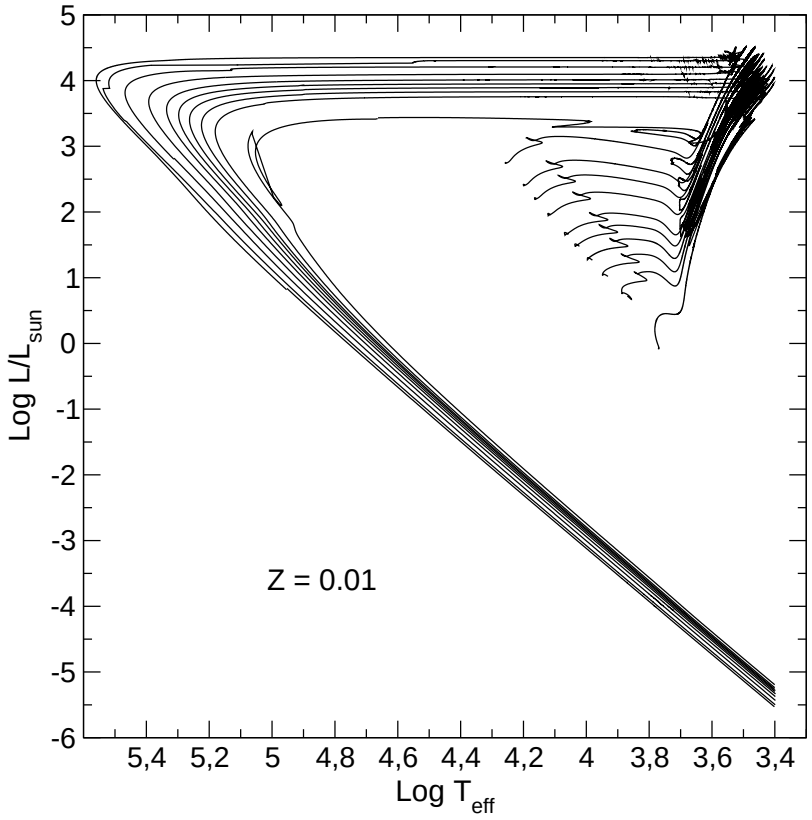

Figure 2.1: Hertzsprung-Russell diagram of our evolutionary sequences for $Z = 0.01$. From bottom to top: evolution of the $1.0\,M_{\odot}$, $1.5\,M_{\odot}$, $1.75\,M_{\odot}$, $2.0\,M_{\odot}$, $2.25\,M_{\odot}$, $2.5\,M_{\odot}$, $3.0\,M_{\odot}$, $3.5\,M_{\odot}$, $4.0\,M_{\odot}$ and $5.0\,M_{\odot}$ model stars. Evolutionary tracks are shown from the ZAMS to advanced stages of white dwarf evolution. Note that the less massive sequence experiences a hydrogen subflash before entering its final cooling track.

the equation of state during the evolutionary stages prior to white dwarf formation. Also listed in this table are the total masses of the residual hydrogen and helium content left in the white dwarfs at the evolutionary stage corresponding to the point of maximum effective temperature in the Hertzsprung-Russell diagram. Note that the residual hydrogen content decreases with the white dwarf mass, a well-known result. For the case of solar metallicity progenitors, the hydrogen mass differs by a factor of 20 for the stellar mass range considered. This general trend is also observed for the mass of the helium content, where the mass of the residual helium ranges from 0.025 to $0.0022\,M_{\odot}$. The hydrogen and helium masses listed in Table 2.1 should be considered as upper limits for the maximum hydrogen and helium content left in

a white dwarf resulting from the evolution of single star progenitors. However, the occurrence of a late thermal pulse after departure from the TP-AGB may reduce the hydrogen mass considerably, see Althaus et al. (2005b).

Note also that for a given white dwarf mass there is a marked dependence of the final hydrogen mass on the initial metallicity of the progenitor star: higher hydrogen masses are expected in metal-poor progenitors, see Iben & MacDonald (1985) and Iben & MacDonald (1986). For instance, for the $0.593\,M_{\odot}$ white dwarf model we find that the hydrogen mass is $\log M_{\rm H} \simeq -3.950$ for the solar metallicity progenitor, while this mass turns out to be $\log M_{\rm H} \simeq -3.777$, for the metal-poor progenitor, i.e. a 50% higher. This is an important issue since one of the factors affecting the white dwarf cooling rate is, precisely, the thickness of the hydrogen-rich envelope. By contrast, in the case of the residual helium content, no appreciable dependence on the metallicity exists. Also shown in Table 2.1 are the number of thermal pulses during the AGB and the total mass lost during the entire AGB phase, in solar units. We find that the number of thermal pulses during the AGB phase is, generally speaking, slightly larger for the set of metal-poor evolutionary sequences. For instance, for the $1.5\,M_{\odot}$ stellar sequence a total of 7 thermal pulses occur for the solar metallicity white dwarf progenitor, while for the metal-poor progenitor this number is 10, thus leading to a more extended mass-loss phase. However, the total mass lost during the entire AGB phase is smaller for the case of a metal-poor progenitor — $0.757\,M_{\odot}$ for the same model star — than for a solar-metallicity progenitor — $0.795\,M_{\odot}$.

Perhaps one of the most interesting results of our full evolutionary calculations is the initial-to-final mass relationship. In Fig. 2.2 we show our results for the case of solar composition ($Z = 0.01$). Specifically, in this figure we show using a solid line the mass of the white dwarf resulting from our theoretical calculations as a function of the initial mass at the ZAMS. For the sake of comparison we also show using a dot-dashed-dashed line the mass of the hydrogen-free core at the beginning of the first thermal pulse as a function of the initial mass of the progenitor star, and we compare this relationship with that of Salaris et al. (1997) — short dashed line — and Dominguez et al. (1999) for $Z = 0.006$ — long dashed line. These two initial-to-final mass relationships were obtained assuming that the mass of the resulting white dwarf corresponds to that of the hydrogen-free degenerate core at the first thermal pulse, and consequently that the core does not grow appreciably afterwards. In addition, we also show (using a dot-dot-dashed line) the recently obtained initial-to-final mass relationship of Weiss & Ferguson (2009) for $Z = 0.008$. In this calculation envelope overshooting was used during the TP-AGB, which, as mentioned in Sect. 2.2.1, considerably reduces the further growth of the hydrogen-free core. We also show the observational initial-to-final mass relationship of Catalán et al. (2008a) — dot-dashed line. This relationship is based on cluster observations of different metallicities, which are close to that adopted in our calculations ($Z = 0.01$). Also shown are the observational results of Kalirai et al. (2008) — with their corresponding error bars — which correspond to metallicities very close to the solar metallicity —

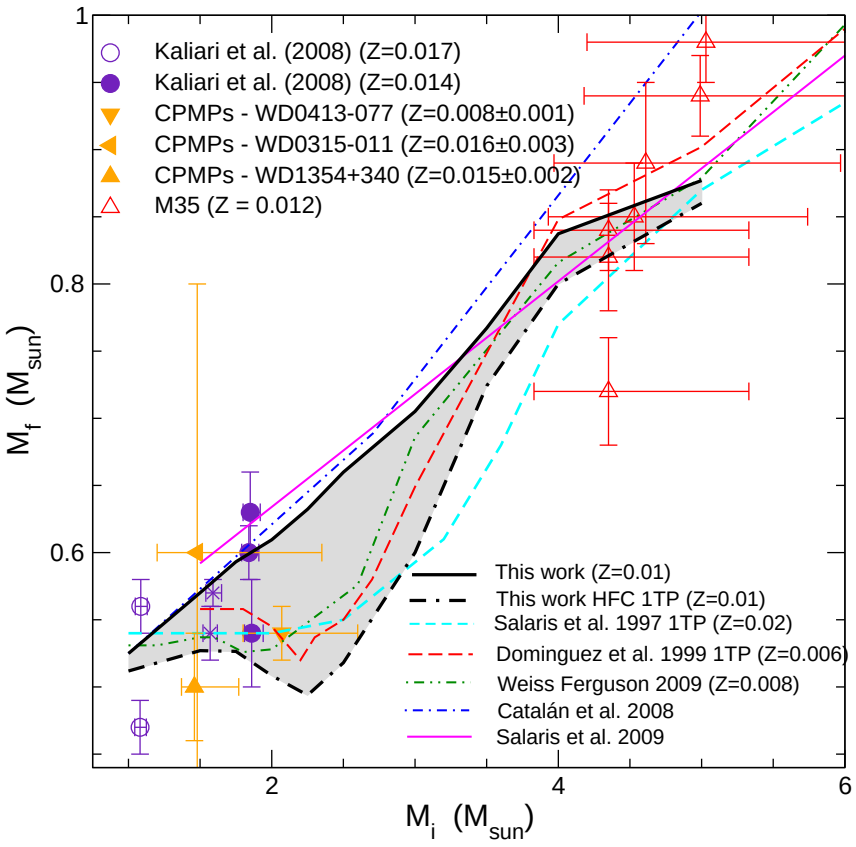

Figure 2.2: Theoretical initial-to-final mass relationship — thick solid line — and mass of the degenerate core at the beginning of the first thermal pulse — thick dot-dashed-dashed line — obtained in this work, both for the case in which the solar composition is adopted. The initial-to-final mass relationships of Salaris et al. (1997) — short dashed line — of Dominguez et al. (1999) — long dashed line — and of Weiss & Ferguson (2009) — dot-dot-dashed line — are also shown. The observational initial-to-final mass relationship of Catalán et al. (2008a) and Salaris et al. (2009) are the dot-dashed and solid lines, respectively. See the main text for additional details.

filled and open circles — and the results for individual white dwarfs in common proper motion pairs of Catalán et al. (2008b) — solid triangles. The main sequence stars of these common proper motion pairs also have solar metallicity. In addition, the results for M35 as quoted in Catalán et al. (2008a), for which the estimated metallicity is also close to solar (Barrado y Navascués et al., 2001) are also shown. Finally, the semi-empirical initial-to-final mass relationship of Salaris et al. (2009) based on open cluster observations is included in Fig. 2.2.

It is to be noted the excellent agreement between our theoretical calculations and the empirical initial-to-final mass relationships, particularly that of Salaris et al. (2009). Note as well that the mass of the hydrogen-free degenerate core at the first thermal pulse for all the theoretical sequences agrees with each other and presents a minimum around $\sim 2.0\,M_{\odot}$, but does not agree with the empirical initial-to-final mass relationship. This emphasizes the importance of carefully following the evolution of the star models from the main sequence all the way through the TP-AGB phase and, finally, to the beginning of the white dwarf cooling track, when the mass-loss rate becomes negligible. In particular, the growth of the core mass during the TP-AGB phase is emphasized as a gray area in Fig. 2.2. The implication of a proper computation of the intial-to-final mass relationship for the carbon-oxygen composition expected in a white dwarf will be discussed in chapter 3.3. Note as well, that our pre-white dwarf evolutionary calculations provide us with accurate and reliable starting configurations at the beginning of the white dwarf cooling phase, as they yield not only self-consistent inner chemical profiles, but also masses of the hydrogen-rich envelopes, helium buffers and core masses which agree with the observational results.

2.3.2 A global view of the white dwarf cooling phase

In Fig. 2.3 we show the different luminosity contributions during the white dwarf cooling phase, for an archetypical $0.609\,M_{\odot}$ carbon-oxygen white dwarf resulting from a progenitor star of $2.0\,M_{\odot}$ with solar composition. The very first phases of the cooling phase are dominated by residual hydrogen burning in the outer layers. This can be easily seen in Fig. 2.3, where the different nuclear luminosities, namely the proton-proton hydrogen-burning luminosity, the CNO bicycle luminosity and the helium-burning luminosity are shown as a function of the cooling age. As can be seen in this figure, at high luminosities the largest contribution comes from the CNO bicycle, being the proton-proton and the helium-burning luminosities orders of magnitude smaller. This a short-lived phase (a few thousand years) and, thus, given the long-lived cooling times of white dwarfs, it is totally negligible in terms of age. Nevertheless, this phase is important as it configures the final thickness of the hydrogen-rich envelope of the white dwarf. After this short-lived phase, the nuclear luminosities abruptly decline (at $\log t \simeq 3.6$) and the release of gravothermal energy becomes the dominant energy source and drives the evolution. In passing, we note

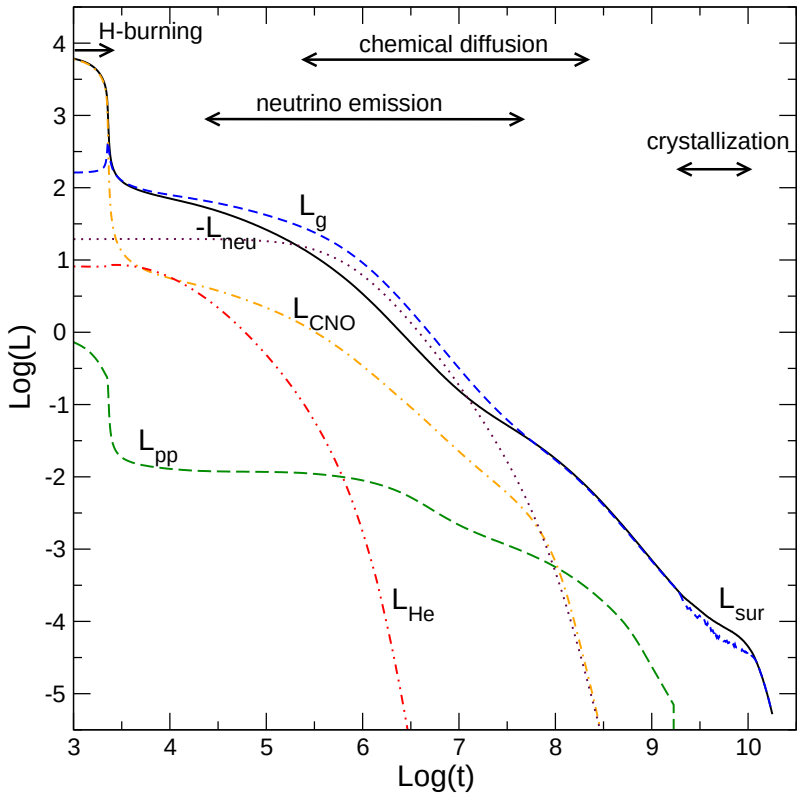

Figure 2.3: Time dependence of the different luminosity contributions for our $0.609\,M_{\odot}$ white dwarf sequence when carbon-oxygen phase separation is included. We show the photon luminosity, $L_{\rm sur}$ (solid line), the luminosities due to nuclear reactions — proton-proton chains, $L_{\rm pp}$ (long dashed line), CNO bicycle, $L_{\rm CNO}$ (dot-dashed line), helium burning, $L_{\rm He}$ (dot-dot-dashed line) — the neutrino losses, $L_{\rm neu}$ (dotted line) and the rate of gravothermal (compression plus thermal) energy release, $L_{\rm g}$ (dashed line). Time is expressed in years counted from the moment at which the remnant reaches $\log T_{\rm eff} = 4.87$ at high luminosity. The various physical processes occuring as the white dwarf cools down are indicated in the figure. The progenitor corresponds to a solar-metallicity $2.0\,M_{\odot}$ star.

that residual nuclear reactions are not totally extinguished until very late phases of the evolution, in agreement with the pioneering results of Iben & MacDonald (1985) and Iben & MacDonald (1986). In fact, there are still small contributions of both the CNO cycle and proton-proton chains until $\log t \simeq 8.3$ and $\log t \simeq 9.0$, respectively. Although almost negligible for the calculation of the cooling age in the case of white dwarfs resulting from solar metallicity progenitors, this residual nuclear burning becomes relevant at very late stages for white dwarfs resulting from low-metallicity progenitors as it lasts for one billion years, see next section. The phase in which the evolution is driven by gravitational contraction lasts for about one million years. During this phase the release of gravothermal energy occurs preferentially in the outer partially- or non-degenerate layers of the white dwarf. More or less at the same epoch — that is, at $\log t \simeq 5.6$ — neutrino losses become also important. In particular, at this epoch neutrinos are the dominant energy sink in the degenerate core of the white dwarf, and their associated luminosity becomes larger than the optical luminosity. In fact, during a relatively long period of time (from $\log t \sim 5.6$ to 7.1) the neutrino luminosity is comparable to the luminosity associated to the gravothermal energy release. It is also interesting to note that at approximately the same time, element diffusion is operating in the outer partially-degenerate envelope, shaping the chemical stratification of the very outer layers of the white dwarf. We will discuss below the resulting chemical stratification. This phase lasts for about 2.2×10^8 years. At $\log t \sim 7.8$ the temperatures in the degenerate core decrease below the threshold where neutrino emission ceases and, consequently, the neutrino luminosity abruptly drops. During this phase of the evolution most of the energy released by the white dwarf has gravothermal origin, and the white dwarf cools according to the classical Mestel's law (Mestel, 1952). Finally, at $\log t \simeq 9.2$ crystallization sets in at the center of the white dwarf and the cooling process slows down due to the release of latent heat and of gravitational energy due to carbon-oxygen phase separation. These physical processes are noticeable as a change in the slope of the cooling curve. Note as well that during the crystallization phase the surface energy is larger than the gravothermal luminosity, a consequence of these two additional energy sources. This phase lasts for $\sim 9.4 \times 10^9$ years. After this phase, the temperature of the crystallized core of the white dwarf drops below the Debye temperature and the heat capacity of the white dwarf drops. Consequently, the white dwarf enters the so-called Debye cooling phase, and the slope of the cooling curve increases again. This occurs at $\log t \sim 10$.

2.3.3 The thickness of the hydrogen envelope

Fig. 2.4 shows the temporal evolution of the masses of the hydrogen content for two representative white dwarf cooling tracks of the two metallicities explored here. Also shown are the ratio of the hydrogen-burning luminosities to the total luminosity. In particular, the thick lines represent the evolution of a $0.609\,M_\odot$ white dwarf

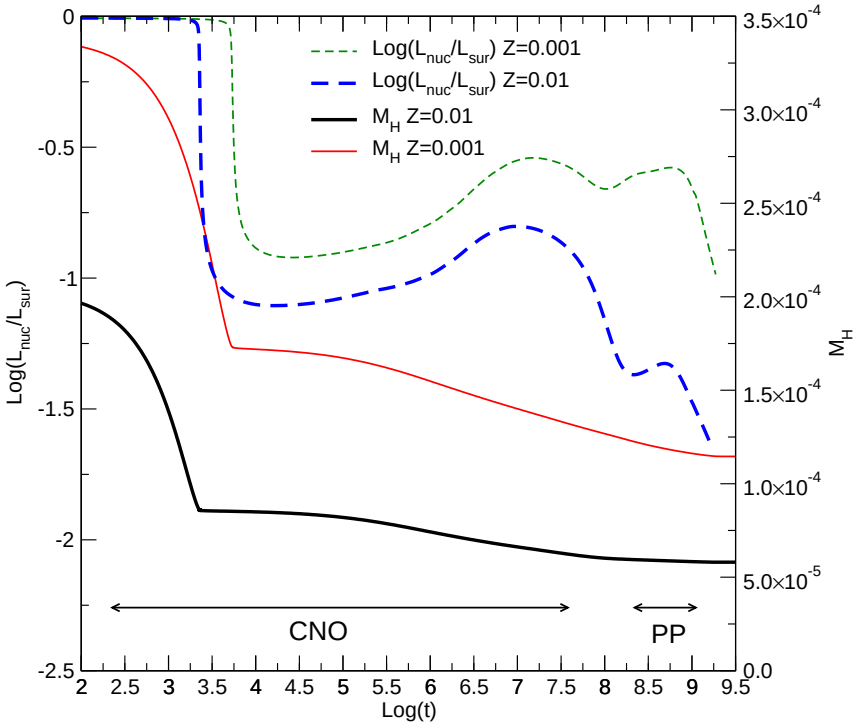

Figure 2.4: Temporal evolution of the hydrogen content $M_{\rm H}$ (in solar masses) and the ratio of hydrogen (proton-proton chains and CNO bicycle) nuclear burning to surface luminosity, solid and dashed lines, respectively. Thick (thin) lines correspond to progenitors with $Z = 0.01$ ($Z = 0.001$). Note that the hydrogen content left in the white dwarf, and therefore the nuclear energy output, are strongly dependent on the metal content of the progenitor stars. Although a large fraction of the hydrogen content is burnt before the remnant reaches the terminal cooling track at young ages, note that in the case of low metallicity, residual burning during the white dwarf stage reduces the hydrogen content considerably. The mass of the white dwarf corresponding to $Z = 0.01$ ($Z = 0.001$) is $0.609 M_{\odot}$ ($0.593 M_{\odot}$).

resulting from a solar progenitor, while the thin lines show that of a $0.593\,M_{\odot}$ white dwarf resulting from a metal-poor progenitor. The solid lines correspond to the evolution of the mass of the hydrogen content, while the dashed lines show the evolution of the nuclear luminosities. As can be seen, residual hydrogen burning is dominant during the first evolutionary phases of the white dwarf stage. As a consequence, the mass of these envelopes decreases for a period of time of $\sim 3 \times 10^3$ years, during which hydrogen burning supplies most of the surface luminosity of the white dwarf. However, as soon as the mass of the hydrogen content decreases below a certain threshold ($\sim 8 \times 10^{-5}\,M_{\odot}$ for the solar-metallicity star and $\sim 1.7 \times 10^{-4}\,M_{\odot}$ for the metal-poor star) the pressure at the bottom of the envelope is not large enough to support further nuclear reactions, and hence the main energy source of

the white dwarf is no longer nuclear reactions but gravothermal energy release, and the hydrogen content reaches a stationary value. This is true in the case of the white dwarf with a solar metallicity progenitor, but for the white dwarf remnant that results from the lower metallicity progenitor star, it is clear that residual hydrogen burning is by no means negligible. In this case, note that hydrogen burning represents an importante fraction of the surface luminosity after $\approx 10^7$ yr of evolution, and even at more advanced stages ($\approx 10^9$ yr), this contribution reaches up to 30%. At this time, the nuclear energy production is almost entirely from the proton-proton chain, and the hydrogen content has been reduced down to $\sim 1.1\times10^{-4}\,M_{\odot}$. The contribution of hydrogen burning to surface luminosity increases for white dwarfs with lower stellar masses. We would like to emphasize at this point the importance of computing self-consistently the very first stages of the white dwarf evolution, as they provide an homogeneous set of white dwarf envelope masses, which as the evolution proceeds influence the cooling of white dwarfs.

2.3.4 The chemical abundances of the envelope

Fig. 2.5 shows the chemical profiles of the $0.609\,M_{\odot}$ white dwarf resulting from a solar metallicity progenitor for selected evolutionary stages along the white dwarf cooling track. Each of the panels is labelled with the luminosity and effective temperature of the evolutionary stage. In these panels we show the abundance profiles of hydrogen, helium, carbon, nitrogen and oxygen in terms of the outer mass fraction. As can be seen in the upper-left panel, which depicts the chemical profiles at the beginning of the cooling track, the resulting white dwarf has a hydrogen-rich envelope, with substantial amounts of heavier elements, like helium, carbon, nitrogen and oxygen. The chemical composition of this layer is similar to that of typical AGB stars that have not experienced third dredge-up episodes, being oxygen more abundant than carbon, and nitrogen almost as abundant as carbon. Specifically, these abundances are essentially fixed by the first dredge-up episode during the red giant phase. The deeper layers in the helium buffer zone show CNO abundances that reflect the occurrence of hydrogen burning in prior stages, with nitrogen far more abundant than carbon and oxygen. As the white dwarf evolves across the knee in the Hertzsprung-Russell diagram, gravitational settling and diffusion become the relevant physical processes and the heavier chemical elements begin to sink appreciably. This is illustrated in the upper-right panel of Fig. 2.5. As can be seen in this panel, at this stage, the white dwarf has already developed a thin pure hydrogen envelope that thickens as evolution proceeds. Note that at this evolutionary stage some diffusion and gravitational settling has already occurred in deeper layers, and the chemical interfaces exhibit less sharp discontinuities. During these stages, the chemical composition has also changed as a result of nuclear burning via the CN cycle at the base of the hydrogen envelope. With further cooling — see the bottom-left panel of Fig. 2.5 — the action of element diffusion becomes more apparent.

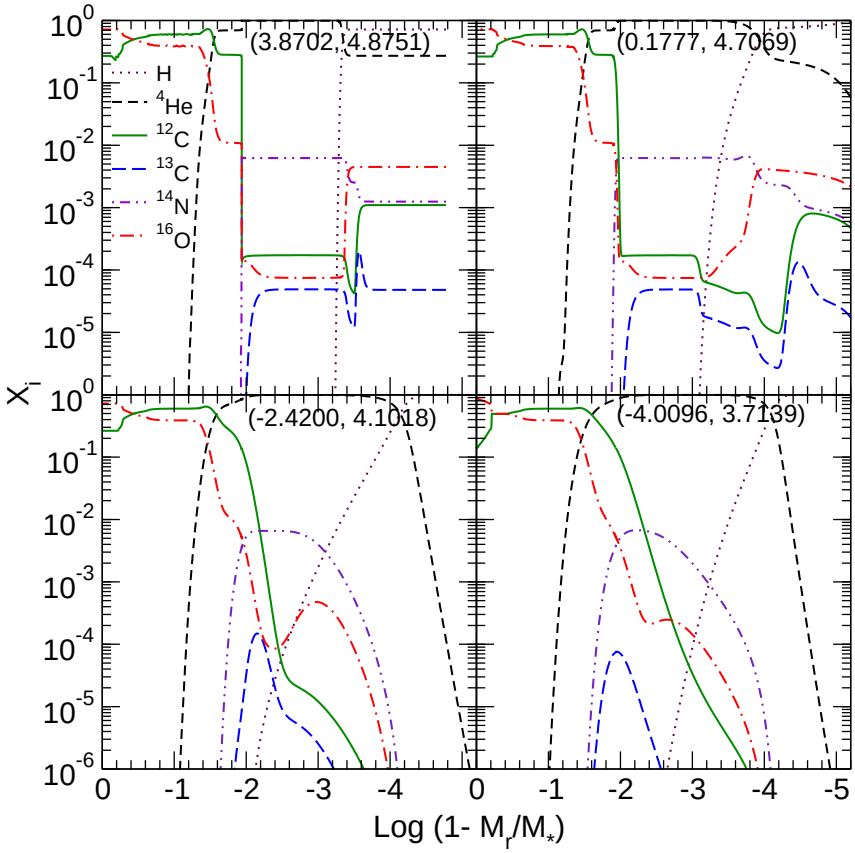

Figure 2.5: Abundance by mass of H, ^{4}He, ^{12}C, ^{13}C, ^{14}N, ^{16}O as a function of the outer mass fraction $\log(1 - M_r/M_*)$ for our 0.609 $M_\odot$ white dwarf sequence at various selected evolutionary stages. The upper-left panel corresponds to the start of the cooling branch ($\log T\mathrm{eff} = 4.87$ at high luminosity). The upper-right panel shows the chemical profiles after some diffusion has already taken place in the envelope. The bottom-left panel shows the situation at the domain of the pulsating DA white dwarfs. Finally, the bottom-right panel shows the chemical abundances after the onset of cyrstallization. Luminosity and effective temperatures ($\log L/L_\odot$, $\log T\mathrm{eff}$) are specified for each stage. The metallicity of the progenitor star is $Z = 0.01$.

In fact, the helium-rich buffer increases its size and both carbon and oxygen sink towards deeper and deeper regions of the white dwarf. Also, the thickness of the hydrogen rich layer increases appreciably, and at the same time, the tail of the hydrogen distribution continues to chemically diffusing inward. At this stage, which correponds to the domain of the pulsating DA white dwarfs, a rather thick hydrogen envelope has been formed, and below it, a helium-rich and several very thin layers, which are rich in even heavier elements — a consequence of the high gravity of the

white dwarf. Finally, the bottom-right panel depicts the situacion after the onset of crystallization. Note the change of carbon and oxygen composition of the core as a result of crystallization. This sequence of figures emphasizes the importance of a proper treatment of time-dependent diffusion processes during white dwarf evolution, and the extent to which the initial chemical stratification at the start of the cooling phase is altered by these processes.

2.3.5 Convective coupling and crystallization

As discussed in several works, the cooling curve is influenced strongly by crystallization. However, at this evolutionary stage the slope of the cooling curve is not only dictated by the release of latent heat and other energy sources associated to crystallization but also by the so-called convective coupling. When the envelope becomes fully convective the inner edge of the convective region reaches the boundary of the degenerate regions (Fontaine et al., 2001). This effect is illustrated in Fig. 2.6, where we show as a function of the surface luminosity (in solar units) the evolution of the cooling times and central temperatures (left scales), and the mass of the crystallized white dwarf core (right scale) for two white dwarfs, a low-mass white dwarf of $0.525\,M_{\odot}$ and a rather massive white dwarf with $M = 0.878\,M_{\odot}$, both resulting from solar metallicity progenitors. As can be seen there, as both white dwarfs cool, there is a gradual decrease of the central temperatures, while their corresponding cooling times also increase smoothly. At approximately $\log(L/L_{\odot}) \simeq -3.8$ crystallization sets in for the less massive white dwarf, whereas for the massive star this occurs at $\log(L/L_{\odot}) \simeq -3$. Convective coupling between the degenerate core and the partially degenerate convective envelope also occurs at low luminosities. Since the inner edge of the convective envelope reaches the boundary of the core, an increase of the rate of energy transfer across the outer opaque envelope occurs, which is much more efficient than radiative transfer alone. As a consequence, the relation between the central temperature and the surface luminosity experiences a sudden change of slope, which can be clearly seen in Fig. 2.6, where we show the region in which convective coupling occurs as a shaded area. Note that in the case of the more massive white dwarf, convective coupling takes place at luminosities markedly lower than that at which crystallization starts in the core. In fact, more than 90% of the white dwarf mass has crystallized by the time convective coupling occurs in the $0.878\,M_{\odot}$ white dwarf. In contrast, for the less massive white dwarf, both crystallization and convective coupling occur at approximately the same stellar luminosity, and thus the resulting impact of these effects on the rate of cooling is more noticeable in this case.

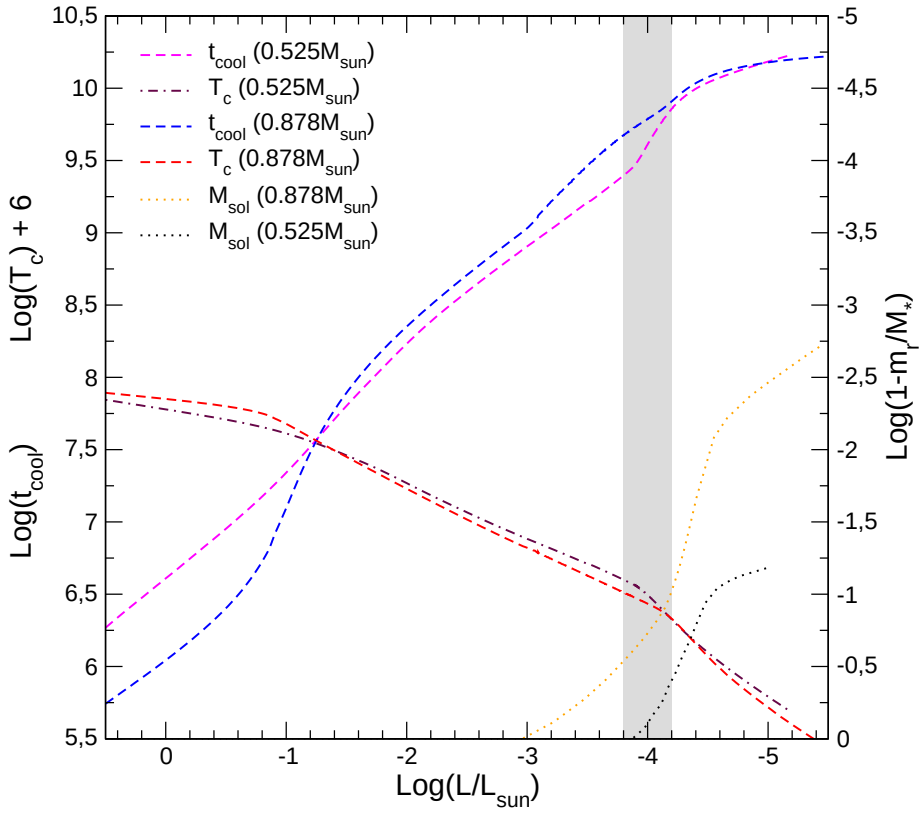

Figure 2.6: Some evolutionary properties corresponding to our 0.878 $M_{\odot}$ and 0.525 $M_{\odot}$ white dwarf sequences with carbon-oxygen phase separation resulting from $Z = 0.01$ progenitors. We show in terms of the surface luminosity the run of the cooling times (dashed lines), of the central temperature (dot-dashed lines), both read on the left-hand-side scale, and the evolution of the growth of the crystallized core (dotted lines) as given by the outer mass fraction on the right-hand-side scale. The gray area marks the occurrence of convective coupling. The energy released due to convective coupling and the energy resulting from the crystallization process markedly impact the cooling curves, see text for details.

2.3.6 Cooling times and chemical composition of the core

One of the most noticeable features of the white dwarf cooling tracks presented here is the inclusion in a self-consistent manner of the release of gravitational energy due to phase separation of carbon and oxygen upon crystallization. Previous studies of this kind Salaris et al. (2000) included the effects of phase separation, but a semian-alytical approach was used. To highlight the importance of phase separation upon crystallization we have computed two different sets of cooling sequences. In the first of these cooling sequences phase separation of carbon and oxygen was fully taken into account, whereas in the second it was disregarded. In Table 2.2 we list for various luminosities the cooling ages of all our white dwarf sequences resulting from solar metallicity progenitors, when carbon-oxygen phase separation is neglected (top section), and the corresponding delays introduced by carbon-oxygen phase separation. We also show the same quantities for the case of metal-poor progenitors in Table 2.3. Clearly, phase separation of carbon and oxygen introduces significant delays at low luminosities, between 1.0 and 1.8 Gyr. It is worth mentioning that at $\log(L/L_{\odot}) = -4.6$, a luminosity slightly smaller than that of the observed drop-off in the disk white dwarf luminosity function, $\log(L/L_{\odot}) \simeq -4.5$, phase separation of carbon and oxygen represents a correction of $\sim 15\%$ to the total age, that although not very large it is not negligible whatsoever if precise cosmochronology is to be performed. At $\log(L/L_{\odot}) = -4.0$, the delays constitute $20 - 25\%$ of the age for the more massive white dwarfs. Note that the magnitude of the delays increases with the mass of the white dwarf. For the case of white dwarfs resulting from metal poor progenitors (see Table 2.3), and for the same fiducial luminosity the delays intro-duced by carbon-oxygen phase separation are slightly larger for the same white dwarf mass. Our computed delays are larger than those obtained by Salaris et al. (2000). For instance, for our $0.609\,M_{\odot}$ white dwarf cooling sequence at $\log(L/L_{\odot}) = -4.6$ we obtain $\delta t \simeq 1.38$ Gyr, while Salaris et al. (2000) at the same luminosity obtain for their $0.61\,M_{\odot}$ white dwarf evolutionary sequence $\delta t \simeq 1.00$ Gyr. This difference stems in part from the larger carbon abundances of our white dwarf model, which leads to a larger energy release of the carbon-oxygen phase separation process, and consequently to larger time delays. Indeed, the chemical profiles used by Salaris et al. (2000) were those of Salaris et al. (1997). The central carbon abundance for the $0.61\,M_{\odot}$ white dwarf is $X_{\rm C} \simeq 0.25$, while for our $0.609\,M_{\odot}$ model we obtain $X_{\rm C} \simeq 0.29$. Hence, the delays introduced by carbon-oxygen phase separation are correspondingly larger in our model. A realistic core composition is crucial for a proper assessment of the energy release from phase separation and its impact on the cooling times.

Fig. 2.7 shows the evolutionary cooling sequences of several selected white dwarfs. Specifically we show the luminosity as a function of the cooling age for white dwarfs with solar metallicity progenitors and masses $0.525\,M_{\odot}$ (upper-left panel), $0.570\,M_{\odot}$ (upper-right panel), $0.609\,M_{\odot}$ (bottom-left panel), and $0.877\,M_{\odot}$

Table 2.2: Cooling ages when carbon-oxygen phase separation is neglected and the accumulated time delays introduced by chemical fractionation at crystallization for the evolutionary sequences with progenitors with $Z = 0.01$.

$-\log(L/L_\odot)$	t (Gyr)									
	$0.525\,M_\odot$	$0.570\,M_\odot$	$0.593\,M_\odot$	$0.609\,M_\odot$	$0.632\,M_\odot$	$0.659\,M_\odot$	$0.705\,M_\odot$	$0.767\,M_\odot$	$0.837\,M_\odot$	$0.878\,M_\odot$
2.0	0.17	0.17	0.17	0.17	0.17	0.17	0.18	0.20	0.21	0.22
3.0	0.80	0.80	0.80	0.80	0.82	0.85	0.89	0.95	1.03	1.07
4.0	3.97	4.17	4.26	4.25	4.26	4.34	4.57	4.75	4.89	4.92
4.2	6.57	6.79	6.85	6.85	6.86	6.95	7.10	7.02	6.80	6.62
4.4	8.88	9.25	9.32	9.34	9.38	9.52	9.73	9.66	9.42	9.17
4.6	10.69	11.03	11.13	11.19	11.25	11.40	11.65	11.59	11.36	11.08
4.8	12.40	12.71	12.77	12.81	12.84	12.96	13.18	13.04	12.71	12.39
5.0	14.13	14.33	14.32	14.34	14.30	14.37	14.50	14.22	13.74	13.32
	δt (Gyr)									
3.0	0.00	0.00	0.00	0.00	0.00	0.00	0.00	0.00	0.00	0.01
4.0	0.10	0.15	0.16	0.23	0.27	0.37	0.67	0.97	1.14	1.20
4.2	0.64	0.87	0.88	0.97	1.00	1.12	1.39	1.47	1.48	1.49
4.4	1.03	1.26	1.28	1.30	1.33	1.45	1.66	1.72	1.68	1.67
4.6	1.15	1.33	1.37	1.38	1.40	1.51	1.72	1.76	1.72	1.72

Table 2.3: Same as Table 2.2 but for $Z = 0.001$.

$-\log(L/L_\odot)$	t (Gyr)						
	$0.505\,M_\odot$	$0.553\,M_\odot$	$0.593\,M_\odot$	$0.627\,M_\odot$	$0.660\,M_\odot$	$0.693\,M_\odot$	$0.864\,M_\odot$
2.0	0.24	0.22	0.19	0.17	0.18	0.19	0.22
3.0	1.01	1.03	0.91	0.83	0.86	0.89	1.06
4.0	4.15	4.49	4.50	4.40	4.48	4.59	4.98
4.2	6.74	7.15	7.11	7.01	7.13	7.21	6.84
4.4	9.01	9.57	9.61	9.54	9.73	9.84	9.42
4.6	10.81	11.39	11.43	11.43	11.63	11.74	11.37
4.8	12.56	13.10	13.08	13.04	13.22	13.30	12.67
5.0	14.33	14.78	14.64	14.53	14.66	14.64	13.66
	δt (Gyr)						
3.0	0.00	0.00	0.00	0.00	0.00	0.00	0.00
4.0	0.08	0.17	0.16	0.25	0.39	0.49	1.14
4.2	0.49	0.80	0.94	1.14	1.24	1.27	1.44
4.4	0.90	1.18	1.34	1.49	1.55	1.57	1.63
4.6	1.04	1.28	1.42	1.58	1.61	1.64	1.70

(bottom-right panel), respectively. The figure emphasizes the evolutionary stages where the processes of convective coupling, cyrstallization and Debye cooling take place. As mentioned, in low-mass white dwarfs, cyrstallization and convective coupling occur approximately at the same luminosity, $\log(L/L_\odot) \approx -4$, thus resulting in a pronounced impact on the cooling rate. As can be observed, the cooling tracks presented here have been computed down to very low luminosities, typically of the order of $10^{-5}\,L_\odot$, or even smaller. At these very low luminosities the central regions of the white dwarf have low enough temperatures to enter the so-called Debye cooling phase. In this phase the specific heat drops abruptly as T^3, and as a consequence the cooling rate is enhanced. Thus, the cooling curve rapidly drops. The transition to this phase of cooling depends on the Debye temperature, $\theta_{\rm D}$, which in turn depends on the density ($\theta_{\rm D} \propto \rho^{1/2}$). Consequently, more massive white dwarfs enter this phase at larger temperatures (luminosities). In our most massive sequence, rapid Debye cooling is expected to occur at the lowest luminosities we computed, as it is clear from Fig. 2.7, while for lower stellar masses, this phase is delayed to much lower luminosities.

Phase separation in the deep interiors of white dwarfs also has obvious imprints in the chemical profiles of carbon and oxygen. To illustrate this, in Fig. 2.8 we display for four selected white dwarf evolutionary sequences the oxygen mass abundance as a function of the interior mass at three selected evolutionary stages. Specifically, we show the abundance profiles shortly after the progenitor star departs from the AGB (dashed lines), the same profiles after Rayleigh-Taylor rehomogeneization (Salaris et al., 1997) has occurred (solid lines), and finally, when the entire white dwarf core has crystallized (dot-dot-dashed lines). For the sake of comparison in the bottom-left panel of this figure we also show as a dashed-dotted line the profile obtained by

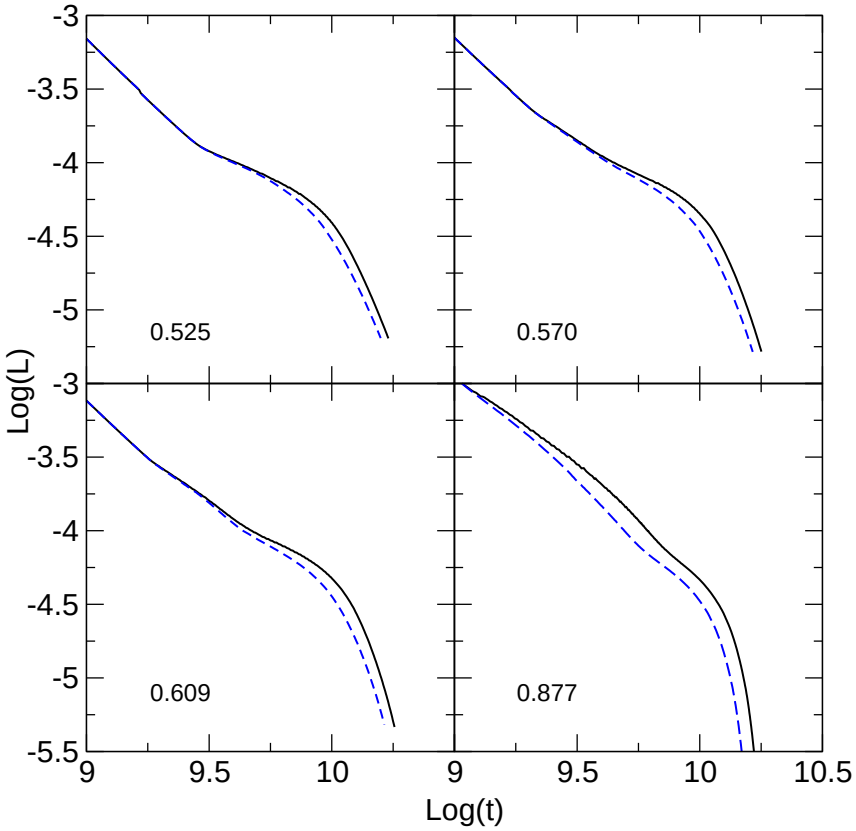

Figure 2.7: Cooling curves at advanced stages in the white dwarf evolution for our sequences of masses $0.525\,M_{\odot}$ (upper-left panel), $0.570\,M_{\odot}$ (upper-right panel), $0.609 M_{\odot}$ (bottom-left panel), and $0.877 M_{\odot}$ (bottom-right panel). Solid lines correspond to the case in which both latent heat and carbon-oxygen phase separation are considered, while dashed lines correspond to the situation when carbon-oxygen phase separation is neglected. The metallicity of progenitor stars is $Z = 0.01$.

Salaris et al. (1997) for a white dwarf of $0.61\,M_{\odot}$, a mass value very close to that of this panel. Note that the central oxygen abundance in the $0.61\,M_{\odot}$ white dwarf of Salaris et al. (1997) is somewhat higher than that of our $0.609\,M_{\odot}$ white dwarf. This is mostly because we use the value of the NACRE compilation for the $^{12}\mathrm{C}(\alpha,\gamma)^{16}\mathrm{O}$ reaction rate (Angulo et al., 1999) which is smaller than the rate of Caughlan et al. (1985) adopted by Salaris et al. (1997). However, another point that has to be considered in this comparison is the fact that the white dwarf mass in Salaris et al. (1997) is assessed at the first thermal pulse. Thus, for a given white dwarf mass, our progenitor stars are less massive than those of Salaris et al. (1997), see our Fig. 2.2. Because of this effect alone, our white dwarf model should be characterized

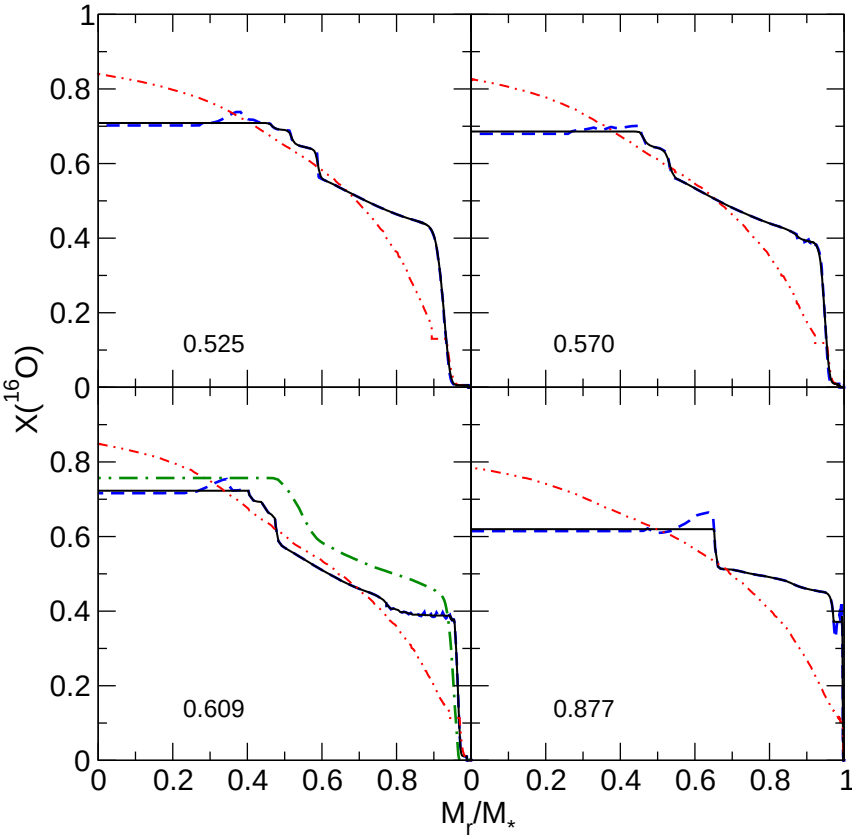

Figure 2.8: Oxygen abundance (by mass) profiles for four selected white dwarfs sequences with stellar masses (in solar masses) as labeled in each panel. Dashed lines show the abundance distribution shortly after the AGB stage. Solid lines show the chemical profile after Rayleigh-Taylor rehomogenization has occurred in the core and dot-dot-dashed lines show the profiles after carbon-oxygen phase separation upon crystallization has finished. In the interests of comparison, in the bottom-left panel we also show with a dash-dotted line the oxygen profile of Salaris et al. (1997) after the rehomogenization phase of a white dwarf with mass $0.609\,M_{\odot}$. Note that in all cases, the initial chemical distribution in the core has been markedly altered by the crystallization process. The metallicity of the progenitor stars is $Z = 0.01$.

by a higher central oxygen abundance than it would have resulted from a more massive progenitor — see Althaus et al. (2010a). Thus, on the one hand we expect a *lower* oxygen abundance in our model because of our adopted cross section for the $^{12}C(\alpha,\gamma)^{16}O$ reaction rate, but on the other hand, we expect a *higher* oxygen abundance because of the lower initial mass of our progenitor star. The net effect is that the central oxygen abundance in our model results somewhat lower than that in the Salaris et al. (1997) model. Finally, the treatment of extra mixing episodes during core helium burning, which are well known to influence the final carbon oxygen stratification, leads to some differences in the expected composition. In our simulation, extra-mixing episodes is treated as a diffusion processes (Herwig et al., 1997), while in Salaris et al. (1997) extra-mixing is considered as a semiconvective process. However, as shown by Straniero et al. (2003) both treatments give rise to a quite similar core chemical stratification, and thus no appreciable difference in the central oxygen abundance should be expected from these treatments.

2.3.7 Colors and the blue hook

The molecular hydrogen formation at low effective temperatures also affects the evolution of our models in the color-magnitude diagram, as shown in Fig. 2.9, which displays the run of the absolute visual magnitude M_V in terms of four standard colours: $V-I$, $U-V$, $B-V$, and $V-R$. For the evolutionary stages computed in this work the turn to the blue at $M_V \approx 17$ is noticeable for the $V-I$ and $V-R$ colors. This effect is due to the H_2-H_2 collision-induced absorption over the infrared spectral regions, which forces stellar flux to emerge at shorter wavelenghts. Note that in this diagram, all our sequences are expected to become markedly blue at $V-I$ and $V-R$. In the $V-I$ color index, the turn-off point occurs between $M_V = 16.5$ and 17.2, depending on the stellar mass value. This range corresponds to luminosities between $\log(L/L_\odot) = -4.6$ and -5.0, and cooling ages between 11.9 and 15 Gyr for our sequences with carbon oxygen phase separation. On the other hand, $U-V$ and $B-V$ colors are sensitive to the Lyα broadening by H-H_2 collisions, which reduces the emergent flux at ultraviolet and blue regions increasing the reddening of these colors in the models cooler than about $T_{\rm eff} = 5\,000$ K (U - $V > 1.0$ and B - $V > 0.8$).

2.4 Summary and conclusions

We have computed a set of cooling sequences for hydrogen-rich white dwarfs, which are appropriate for precision white dwarf cosmochronology. Our evolutionary sequences have been self-consistently evolved from the zero age main sequence, through the core hydrogen and helium burning evolutionary phases to the thermally pulsing asymptotic giant branch and, ultimately, to the white dwarf stage. This has been done for white dwarf progenitors with two different metallicities. For the first set of evolutionary sequences we have adopted solar metallicity. This allows us to obtain

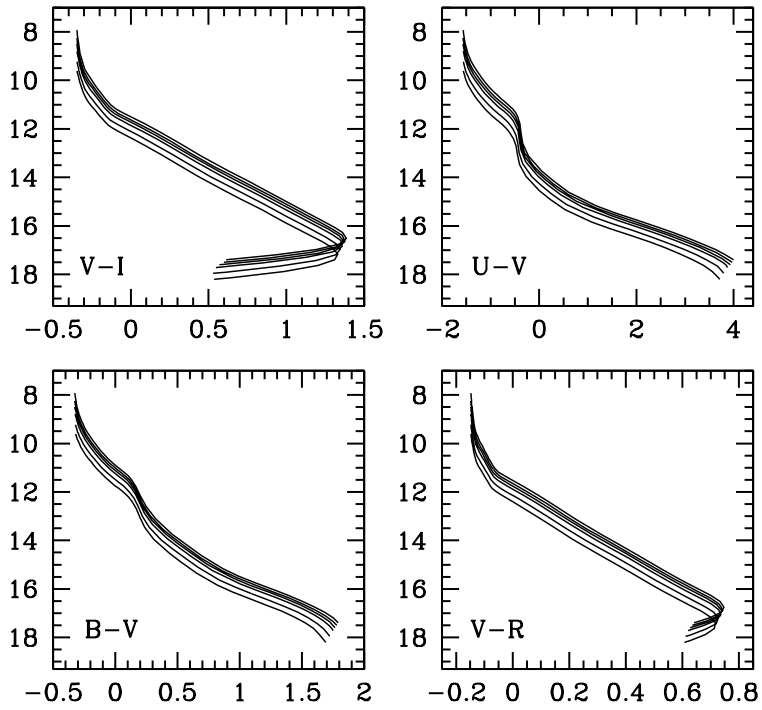

Figure 2.9: Absolute visual magnitude M_V in terms of the color index $V - I$ (upper-left panel), $U - V$ (upper-right panel), $B - V$ (bottom-left panel), and $V - R$ (bottom-right panel), for the complete evolutionary tracks of our sequences with $Z = 0.01$, from top to bottom: $0.525\,M_\odot$, $0.570\,M_\odot$, $0.609\,M_\odot$, $0.659\,M_\odot$, $0.767\,M_\odot$, and $0.878\,M_\odot$.

accurate ages for white dwarfs in the local Galactic disk. The second set of cooling sequences corresponds to a metallicity typical of most Galactic globular clusters, $Z = 0.001$, thus allowing to obtain accurate ages for metal-poor stellar systems. To the best of our knowledge, this is the first set of self-consistent evolutionary sequences covering different initial masses and metallicities.

Our main findings can be summarized as follows. First, our evolutionary sequences correctly reproduce the observed initial-to-final mass relationship of white dwarfs. Specifically, our evolutionary calculations are in excellent agreement with the recent results of Salaris et al. (2009) for white dwarfs with solar metallicity progenitors. Second, we corroborate the importance of convective coupling at low luminosity in the cooling of white dwarfs, as originally suggested by Fontaine et al.

(2001). Third, we demonstrate the importance of residual hydrogen burning in white dwarfs resulting from low-metallicity progenitors. Fourth, we confirm as well the importance of carbon-oxygen phase separation upon crystallization, in good qualitative agreement with the results of Garcia-Berro et al. (1988a,b), Segretain et al. (1994) and Salaris et al. (1997, 2000). Although the computed delays are smaller than those previously estimated by Segretain et al. (1994), they are larger than those computed by Salaris et al. (2000), and are by no means negligible if precision white dwarf cosmochronology is to be done. However, we would like to mention that these delays depend crucially on the previous evolutionary history of white dwarf progenitors and, particularly, on the rate of the $^{12}C(\alpha,\gamma)^{16}O$ nuclear reaction, as well as on the adopted treatment for convective mixing. Additionally, since our evolutionary sequences rely on state-of-the-art non-gray model atmospheres, they reproduce the well-known blue hook of very old hydrogen-rich white dwarfs caused by H_2-H_2 collision-induced absorption (Hansen, 1999). Finally, we show the impact of Lyα quasi-molecular opacity on the evolution of cool white dwarfs in the color-magnitude diagram.

We would like to emphasize that our full treatment of the entire evolutionary history of white dwarfs has allowed us to obtain consistent white dwarf initial configurations. In particular, the mass of the hydrogen-rich envelope and of the helium buffer were obtained from evolutionary calculations, instead of using typical values and artificial initial white dwarf models. This has implications for the cooling rates of old white dwarfs, as the thicknesses of these outer layers control the cooling speed of such white dwarfs. Another important issue which we would like to mention is that our calculations also yield self-consistent interior chemical profiles. This also has relevance for the cooling of white dwarfs, as the release of latent heat and gravitational energy due to carbon-oxygen phase separation upon crystallization crucially depend on the previous evolutionary history of white dwarfs. Also, the chemical stratification of white dwarf progenitors is important for correctly computing the specific heat of white dwarf interiors. We would like to stress as well that the evolutionary tracks of cooling white dwarfs presented here has been computed with the most accurate physical inputs and with a high degree of detail and realism. In particular, our calculations include nuclear burning at the very early phases of white dwarf evolution — which is important to determine the final thickness of the hydrogen-rich envelope — diffusion and gravitational settling — which are important to shape the profiles of the outer layers — accurate neutrino emission rates — which control the cooling at high luminosities — crystallization and phase separation of carbon and oxygen — which dominate the cooling times at low luminosities — a very detailed equation of state — which is important in all the evolutionary phases — and improved non-gray model atmospheres — which allow for a precise determination of white dwarf colors and outer boundary conditions for the evolving models. Finally, we would like to remark that these evolutionary sequences are important as well for the calculation of self-consistent models of pulsating DA

white dwarfs. Detailed tabulations of our evolutionary sequences are available at the website `http://www.fcaglp.unlp.edu.ar/evolgroup`.

Chapter 3

Chemical profiles for the asteroseismology of ZZ Ceti stars

In this chapter we present new white dwarf chemical profiles appropriate for pulsational studies of ZZ Ceti stars on the basis of full evolutionary calculations for both white dwarfs and progenitor stars. We perform adiabatic pulsation calculations, and find that the whole $g-$mode period spectrum and the mode-trapping properties of ZZ Ceti stars as derived from our new chemical profiles are substantially different from those based on chemical profiles widely used in existing asteroseismological studies. Thus, we expect the asteroseismological models derived from our chemical profiles to be significantly different from those found thus far.

3.1 Introduction

Pulsating DA white dwarfs, or ZZ Ceti stars, are found within a very narrow strip of effective temperatures between 10 500 K and 12 500 K. They are characterized by multiperiodic brightness variations of up to 0.30 mag caused by non-radial $g-$modes of low degree ($\ell \leq 2$) with periods between 100 and 1200 s. The comparison of the observed pulsation periods and the periods computed for appropriate theoretical models (white dwarf asteroseismology) allows to infer details of their origin, internal structure and evolution (Winget & Kepler, 2008; Fontaine & Brassard, 2008), as well as to study axions, crystallization, and the presence of planets around white dwarfs.

Castanheira & Kepler (2008) and Castanheira & Kepler (2009) have performed asteroseismological fits to DAVs by employing white dwarf models that assume the core chemical composition to be 50% O and 50 % C. They found that the thickness of the H envelopes is in the range $10^{-4} \gtrsim M_{\rm H}/M_* \gtrsim 10^{-10}$, with a mean value of $M_{\rm H}/M_* = 5 \times 10^{-7}$. This suggests that an important fraction of DAs characterized

by envelopes substantially thinner than predicted by the standard evolution theory could exist. Bischoff-Kim et al. (2008) performed an asteroseismological study on G117−B15A and R 548 by employing DA white dwarf models similar to those employed by Castanheira & Kepler (2008) and Castanheira & Kepler (2009), but incorporating realistic core chemical profiles according to Salaris et al. (1997). The mass and effective temperatures found by Bischoff-Kim et al. (2008) for G117−B15A are rather high (especially the mass, $0.66\,M_{\odot}$).

Here we present consistent chemical profiles for both the core and the envelope of white dwarfs with various stellar masses appropriate for detailed asteroseismological fits of ZZ Ceti stars. These chemical profiles are extracted from the full and complete evolution of progenitor stars from the zero age main sequence, to the thermally-pulsing and mass-loss phases on the Asymptotic Giant Branch (AGB), and from time-dependent element diffusion predictions during the white dwarf stage, by using an updated version of the `LPCODE` stellar evolutionary code (Althaus et al., 2010c). Core overshooting is treated as a diffusion process. Overshooting during the thermally-pulsing AGB phase is not considered. These profiles will be valuable in conducting future asteroseismological studies of ZZ Ceti stars that intend to include realistic chemical profiles throughout the interior of white dwarfs. To assess the impact of these new profiles on the theoretical pulsational inferences, we perfom adiabatic pulsation computations and compare the resulting periods with the pulsational inferences based on the most widely used chemical profiles in existing asteroseismological fits. Using these profiles we perfom adiabatic pulsation computations and compare the resulting periods with the pulsational inferences based on the most widely used chemical profiles in existing asteroseismological fits.

In particular, we compute the complete evolution of ten evolutionary sequences with initial stellar mass ranging from 1 to $5\,M_{\odot}$. The stellar mass of the resulting white dwarfs is in the range $0.5249 - 0.8779\,M_{\odot}$. We recall that the final carbon-oxygen stratification of the emerging white dwarf depends on both the efficiency of the $^{12}\mathrm{C}(\alpha,\gamma)^{16}\mathrm{O}$ reaction rate and the occurrence of extra-mixing episodes toward the late stage of core helium burning. In particular, the systematically lower oxygen abundances of our models as compared with those of Salaris et al. (1997) are due mostly to our use of the cross section for the $^{12}\mathrm{C}(\alpha,\gamma)^{16}\mathrm{O}$ reaction rate given by Angulo et al. (1999), which is smaller than the rate of Caughlan et al. (1985) adopted by Salaris et al. (1997).

The chapter is organized as follows. In Sect. 3.2, we provide a description of the input physics assumed in the evolutionary calculations of relevance for the chemical composition. In Sect. 3.3 we discuss the importance of the initial-final mass relationship for the expected white dwarf carbon-oxygen composition. The resulting chemical profiles are described at some length in Sect. 3.4. The implications of our new chemical profiles for the pulsational properties of ZZ Ceti stars are discussed in Sect. 3.5. We conclude in Sect. 3.6 by summarizing our findings.

Table 3.1: Initial and final stellar mass (in solar units), and the central oxygen abundance (mass fraction) left after core helium burning, and after Rayleigh-Taylor rehomogenization. The progenitor metallicity is $Z = 0.01$.

$M_{\rm ZAMS}$	$M_{\rm WD}$	$X_{\rm O}$(CHB)	$X_{\rm O}$(RT)
1.00	0.5249	0.702	0.788
1.50	0.5701	0.680	0.686
1.75	0.5932	0.699	0.704
2.00	0.6096	0.716	0.723
2.25	0.6323	0.747	0.755
2.50	0.6598	0.722	0.730
3.00	0.7051	0.658	0.661
3.50	0.7670	0.649	0.655
4.00	0.8373	0.635	0.641
5.00	0.8779	0.615	0.620

3.2 Input physics

The chemical profiles presented in this chapter have been extracted from full and complete evolutionary calculations for both the white dwarfs and their progenitor stars, by using an updated version of the LPCODE stellar evolutionary code — see A.1, as well as Althaus et al. (2005c), and references therein. This code has recently been employed to study different aspects of the evolution of low-mass stars, such as the formation and evolution of DA white dwarfs — see chapter 2, as well as Renedo et al. (2010) — H-deficient white dwarfs, PG 1159 and extreme horizontal branch stars (Althaus et al., 2005c; Miller Bertolami & Althaus, 2006; Miller Bertolami et al., 2008; Althaus et al., 2009a), as well as the evolution of He-core white dwarfs with high metallicity progenitors (Althaus et al., 2009b). It has also been used to study the initial-final-mass relation by Salaris et al. (2009), where a test and comparison of LPCODE with other evolutionary codes has also been made. Details of LPCODE can be found in these works. In what follows, we comment on the main input physics that are relevant for this chapter. We assume the metallicity of progenitor stars to be $Z = 0.01$.

Except for the evolutionary stages corresponding to the thermally-pulsing AGB phase, we have considered the occurrence of extra-mixing episodes beyond each convective boundary following the prescription of Herwig et al. (1997) — see more details in A.1.1). The occurrence of extra-mixing episodes during core helium burning largely determines the final chemical composition of the white dwarf core. In this sense, our treatment of time-dependent extra-mixing episodes predicts a core chemical stratification similar to that predicted by the phenomenon of "semicon-

vection" during central helium burning, which naturally yields the growth of the convective core (Straniero et al., 2003). Finally, the breathing pulse instability occurring towards the end of core helium burning was suppressed — see Straniero et al. (2003) for a discussion of this point. In our simulations, breathing pulses have been suppressed by gradually decreasing the parameter f from the moment the helium convective core starts to receed (which occurs once the helium abundance in the core decreases below $\approx 0.05-0.1$). At this stage, the gradual suppression of extra-mixing toward the end of core helium burning bears no consequences for the final chemical stratification.

Other physical ingredients considered in LPCODE are the radiative opacities from the OPAL project (Iglesias & Rogers, 1996), including carbon- and oxygen-rich composition, supplemented at low temperatures with the molecular opacities of Alexander & Ferguson (1994). During the white dwarf regime, the metal mass fraction Z in the envelope is not assumed to be fixed. Instead, it is specified consistently according to the prediction of element diffusion. To account for this, we have considered radiative opacities tables from OPAL for arbitrary metallicities. For effective temperatures less than 10 000 K we have included the effects of molecular opacitiy by assuming pure hydrogen composition from the computations of Marigo & Aringer (2009). This assumption is justified because element diffusion leads to pure hydrogen envelopes in cool white dwarfs. The conductive opacities are those of Cassisi et al. (2007), and the neutrino emission rates are taken from Itoh et al. (1996) and Haft et al. (1994). For the high density regime characteristics of white dwarfs, we have used the equation of state of Segretain et al. (1994), which accounts for all the important contributions for both the liquid and solid phases — see Althaus et al. (2007) and references therein.

In this study, we have considered the distinct physical processes that are responsible for changes in the chemical abundance distribution during white dwarf evolution. In particular, element diffusion strongly modifies the chemical composition profile throughout their outer layers. As a result of diffusion processes, our sequences developed pure hydrogen envelopes, the thickness of which gradually increases as evolution proceeds. We have considered gravitational settling as well as thermal and chemical diffusion — but not radiative levitation, which is relevant only for the hottest and brightest post-AGB and early white-dwarf cooling stages for determining the surface composition — of ^{1}H, ^{3}He, ^{4}He, ^{12}C, ^{13}C, ^{14}N and ^{16}O, see Althaus et al. (2003) for details. Our treatment of time-dependent diffusion is based on the multicomponent gas treatment presented in Burgers (1969). In LPCODE, diffusion becomes operative once the wind limit is reached at high effective temperatures (Unglaub & Bues, 2000). In addition, abundance changes resulting from residual nuclear burning — mostly during the hot stages of white dwarf evolution — have been taken into account in our simulations. Finally, we considered the chemical rehomogenization of the inner carbon- oxygen profile induced by Rayleigh-Taylor (RT) instabilities following Salaris et al. (1997). These instabilities arise because of the

positive molecular weight gradients that remain above the flat chemical profile left by convection during core helium burning.

3.3 The importance of the initial-final mass relationship

As mentioned, chemical profiles appropriate for DA white dwarfs have been derived from the full evolutionary calculations of progenitor stars for solar metallicity. To this end, the complete evolution of ten evolutionary sequences with initial stellar mass ranging from 1 to 5 $M_{\odot}$ were computed from the ZAMS through the thermally-pulsing and mass-loss phases on the AGB and finally to the domain of planetary nebulae. In Table 3.1 we list the stellar masses of the resulting white dwarfs, together with the inital masses of the progenitor stars on the ZAMS. Also listed in Table 3.1 is the central oxygen abundance both at the end of core He burning and after chemical rehomogenization by Rayleigh-Taylor instabilities.

We mention that extra-mixing episodes were disregarded during the thermally-pulsing AGB phase. In particular, a strong reduction (a value of f much smaller than 0.016) of extra-mixing episodes at the base of the pulse-driven convection zone is supported by simulations of the $s-$process abundance patterns (Lugaro et al., 2003) and, more recently, by observational inferences of the initial-final mass relation (Salaris et al., 2009). As a result, it is expected that the mass of the hydrogen-free core of our sequences gradually grows as evolution proceeds through the thermally-pulsing AGB. This is because a strong reduction or suppression of extra-mixing at the base of the pulse-driven convection zone strongly inhibits the occurrence of third dredge-up, thus favoring the growth of the hydrogen-free core. We considered mass-loss episodes during the core helium burning stage and on the red giant branch following Schröder & Cuntz (2005). During the AGB and thermally-pulsing AGB phases, we adopted the maximum mass loss rate between the prescription of Schröder & Cuntz (2005) and that of Vassiliadis & Wood (1993). In the case of a strong reduction of third dredge-up, as occurred in our sequences, mass loss plays a major role in determining the final mass of the hydrogen-free core at the end of the TP-AGB evolution, and thus the initial-final mass relation (Weiss & Ferguson, 2009).

We begin by examining Fig. 3.1 which displays the central oxygen abundance by mass fraction left after core helium burning. The upper panel shows the predicted central oxygen abundance in terms of the hydrogen-free core mass right before the first thermal pulse, while the lower panel shows this quantity in terms of the initial stellar mass on the ZAMS. The predictions of our calculations — solid lines — are compared with those of Salaris et al. (1997) — dashed lines. Note the qualitatively good agreement between both sets of calculations. We recall that the final carbon-oxygen stratification of the emerging white dwarf depends on both the efficiency of the $^{12}C(\alpha,\gamma)^{16}O$ reaction rate and the occurrence of extra-mixing episodes toward the late stage of core helium burning. In particular, the systematically lower oxygen

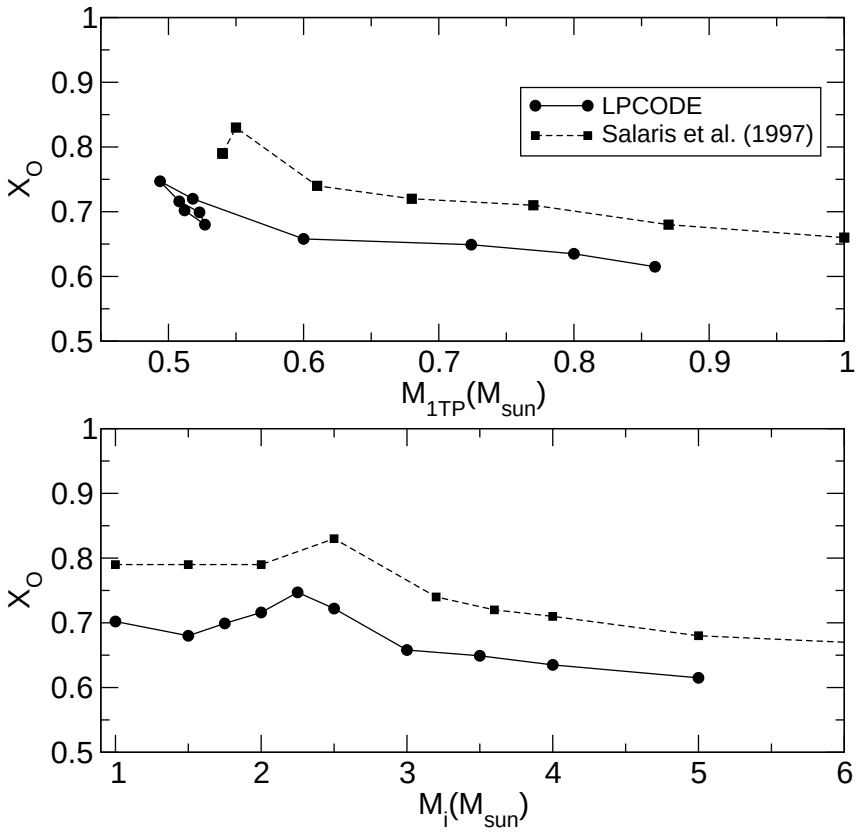

Figure 3.1: Central oxygen abundance (mass fraction) left after core helium burning in terms of both the hydrogen-free core mass right before the first thermal pulse (upper panel) and the initial stellar mass on the ZAMS (lower panel). The solid lines show our results while the dashed lines show those of Salaris et al. (1997)

abundances of our models are due mostly to our use of the cross section for the $^{12}C(\alpha,\gamma)^{16}O$ reaction rate given by Angulo et al. (1999), which is smaller than the rate of Caughlan et al. (1985) adopted by Salaris et al. (1997). Note that both sets of calculations predict a maximum in the central oxygen abundance at an initial mass of $M \approx 2.5 M_{\odot}$.

A careful computation of the evolutionary stages during the thermally-pulsing AGB and the resulting initial-final mass relationship is an important aspect concerning the final carbon-oxygen composition of the white dwarf core. This can be seen by inspecting Fig. 3.2, where various theoretical initial-final mass relationships, giving the mass of the hydrogen-free core in terms of the ZAMS mass of the progenitor, are plotted. The results shown in this figure include the predictions of our full evolutionary calculations at the end of the thermally-pulsing AGB phase and at the beginning of the first thermal pulse (circles and squares, respectively).

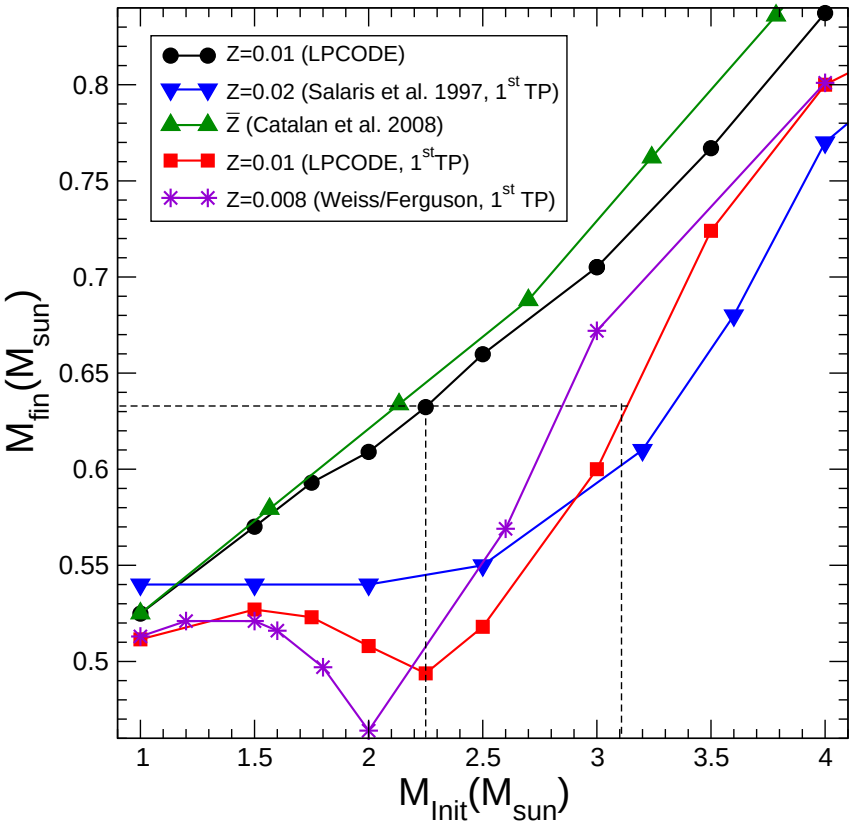

Figure 3.2: Initial-final mass relationships: The final mass given by the hydrogen-free core mass is depicted in terms of the initial mass of the progenitor star. In addition to the observational data from open clusters (Catalán et al., 2008a), upwards triangles, we show the theoretical predictions given by our calculations at the end of the TP-AGB phase and before the first thermal pulse (circles and squares, respectively). Also shown are the predictions of Weiss & Ferguson (2009) and Salaris et al. (1997) before the first thermal pulse (stars and downwards triangles, respectively).

Our relationships are compared with those of Salaris et al. (1997) and Weiss & Ferguson (2009), both at the beginning of the first thermal pulse. We also show the semi-empirical initial-final mass relationship of Catalán et al. (2008a), based on white dwarfs in open clusters and in common proper motions pairs with metallicities close to $Z = 0.01$, the metallicity we assume for the progenitor stars of our sequences. In view of the discussion of the preceeding paragraph, note the increase in the mass of the hydrogen-free core during the thermally-pulsing AGB stage. As a result, the initial-final mass relationship by the end of the thermally-pulsing AGB becomes markedly different from that determined by the mass of the hydrogen-free core before the first thermal pulse. For the carbon-oxygen composition expected in

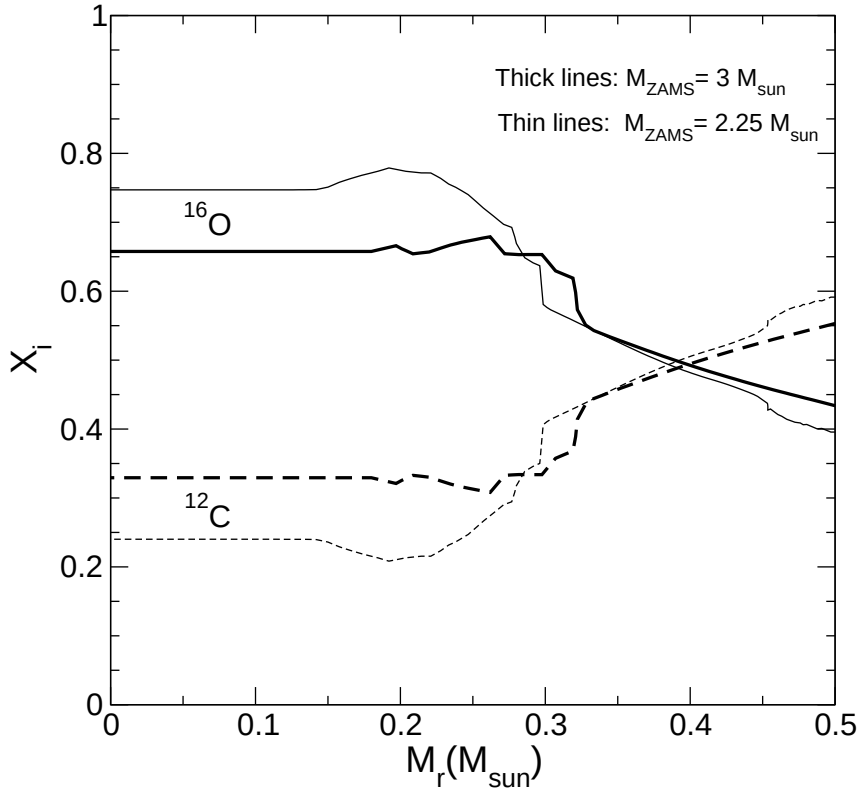

Figure 3.3: Inner carbon and oxygen abundance by mass for the $0.63\,M_{\odot}$ white dwarf resulting from two different progenitors that lead to the same white dwarf mass. The chemical profiles correspond to progenitor stars with initial stellar mass of 3 and $2.25\,M_{\odot}$ (thick and thin lines, respectively), and at stages before chemical rehomogenization by Rayleigh-Taylor instability.

a white dwarf, this is an important issue. Indeed, if the mass of the hydrogen-free core is assumed to be essentially the mass of the resulting white dwarf, it is clear that a white dwarf with a given mass may correspond to different progenitor stellar masses depending on the assumed initial-final mass relationship. For instance, from our theoretical initial-to-final mass relationships, a white dwarf with $0.63\,M_{\odot}$ would correspond to a progenitor star with a stellar mass of $2.25\,M_{\odot}$ if the initial-final mass relationship is assessed at an advanced stage in the thermally-pulsing AGB phase, or $3\,M_{\odot}$ if the white dwarf mass is assumed to be the hydrogen-deficient core mass right before the first thermal pulse. In particular, we note that Salaris et al. (1997) adopt the mass of the hydrogen-free core at the start of the first thermal pulse as the mass of the resulting white dwarf.

The implication of this dichotomy in the mass of the progenitor star for the white dwarf carbon-oxygen composition is illustrated in Fig. 3.3. We show the inner car-

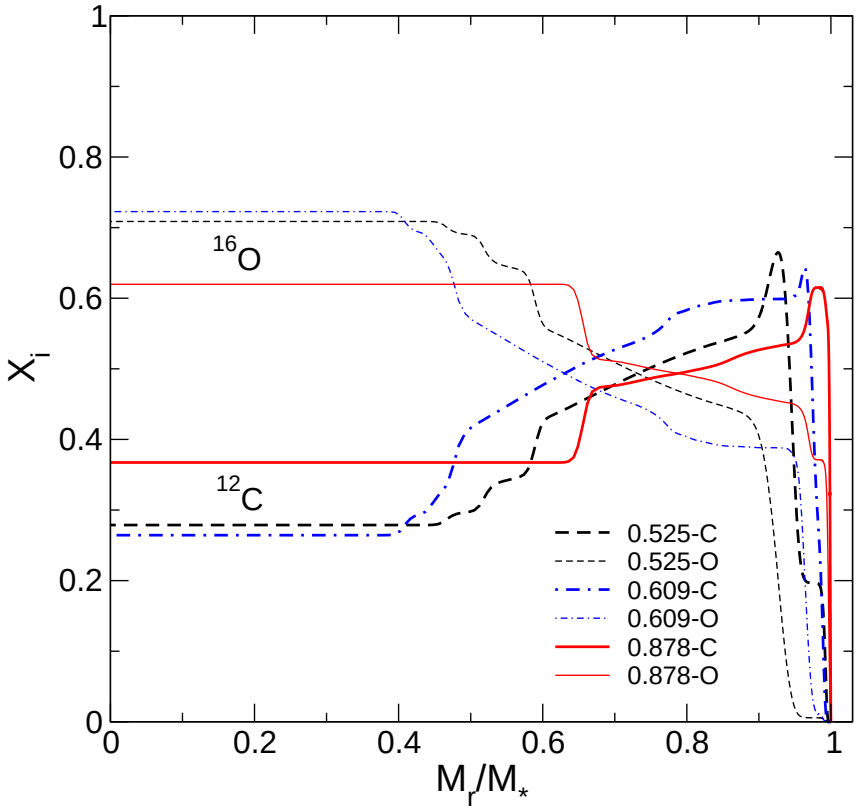

Figure 3.4: Inner carbon and oxygen abundance by mass for the 0.525, 0.609, and 0.878 $M_\odot$ white dwarf models at $T_{\rm eff} \approx 12\,000$ K, and after chemical rehomogenization by Rayleigh-Taylor instabilities.

bon and oxygen abundance distribution for the 0.63 $M_\odot$ white dwarf resulting from the two different progenitors discussed previously. For illustrative purposes, chemical rehomogenization by Rayleigh-Taylor instabilities has not been considered in this particular example. The thick lines display the chemical profile for the progenitor star with 3 $M_\odot$ characterized before the first thermal pulse by a hydrogen-free core of 0.63 $M_\odot$. The thin lines show the chemical profile for the 2.25 $M_\odot$ progenitor which leads to the same white dwarf mass but after evolution has proceeded through the thermally-pulsing AGB phase (see Fig.3.2). Note the different chemical profiles expected in both cases. In particular, the central oxygen abundance may be underestimated by about 15% should the white dwarf mass is assumed to be the hydrogen-free core mass right before the first thermal pulse. Note that, however, this variation is an upper limit, and it would be less for other white-dwarf masses. Clearly, the initial-final mass relationship is an aspect that has to be considered in the problem of the carbon-oxygen composition expected in a white dwarf, as well

as in attempts at constraining, from pulsational inferences of variable white dwarfs, the mixing processes and the efficiency of the $^{12}C(\alpha,\gamma)^{16}O$ reaction rate in the core of helium burning stars. Also, it is important to realize that a larger oxygen abundance increases the cooling rate of the white dwarf because of the lower heat capacity and because an initial larger oxygen abundance reduces the energy release by phase separation on cyrstallization (Isern et al., 2000).

3.4 The internal chemical profiles

The carbon-oxygen stratification for some selected models is shown in Figs. 3.3 and 3.4. The shape of the chemical profiles before rehomogenization is given in Fig. 3.3. Easily recognizable are the flat chemical profiles in the inner part of the core left by convection during the core helium burning, the bumps resulting from the inclusion of extra-mixing episodes beyond the fully convective core, and the signatures of the outward-moving helium-burning shell after the end of core helium burning. Because of the larger temperatures in the helium burning shell, the oxygen abundance decreases in the outer regions of the carbon-oxygen core.

The expected chemical profiles of some of our white dwarf models when evolution has proceeded to the domain of the ZZ Ceti stars are displayed in Fig. 3.4. At this stage, chemical rehomogenization by Rayleigh-Taylor instabilities has already smeared out the bumps in the inner profiles, leading to quite extended flat chemical profiles. Note the dependence of both the core chemical abundances and the location of the chemical transitions on the stellar mass. Pulsation periods in white dwarf models are very sensitive to the shapes and locations of the chemical transions zones (see section 3.5). This emphasizes the need for a detailed knowledge of the progenitor history for a realistic treatment of white dwarf evolution and pulsations. The chemical profiles in the outermost regions, resulting from prior mixing and burning events during the thermally-pulsing AGB phase, are markedly modified by the diffusion processes acting during white dwarf evolution, particularly in the case of more massive models, where chemical diffusion and gravitational settling are notably more efficient. This can be better appreciated in Fig. 3.5, where the chemical abundance distribution for white dwarf models of different stellar masses is depicted in terms of the outer mass fraction. These plots put special emphasis in the outer regions of the model. In this figure and for each stellar mass, thin lines show the chemical abundance distribution at early stages of white dwarf evolution when diffusion has not had time to act. The signature of the evolution through the thermally-pulsing AGB stage on the chemical profile, particularly the formation of the helium-rich buffer and the underlying intershell region rich in helium and carbon — built up during the mixing episode at the last AGB thermal pulse — are easily visible. The presence of carbon in the intershell region stems from the short-lived convective mixing that has driven the carbon-rich zone upward during the peak of the last helium pulse on

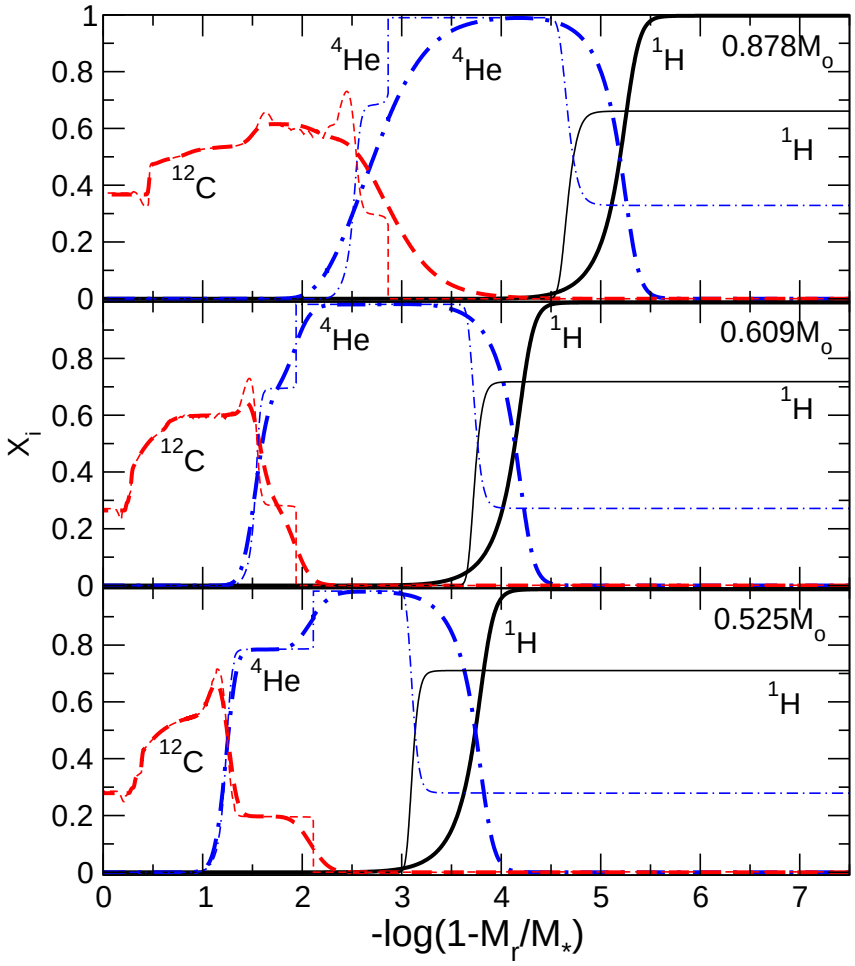

Figure 3.5: Abundance distribution of hydrogen, helium and carbon in terms of the outer mass fraction for the 0.878, 0.609 and 0.525 $M_{\odot}$ white dwarf models at two selected stages just after the maximum effective temperature point and near the beginning of the ZZ Ceti regime (thin and thick lines, respectively).

the AGB. Thick lines depict the situation at advanced stages, near the ZZ Ceti instability strip, when element diffusion has strongly modified the chemical abundance distribution and resulted in the formation of a thick pure hydrogen envelope plus an extended inner tail. In the more massive models, chemical diffusion leads to a significant amount of carbon in the helium buffer zone. Also near-discontinuities in the initial abundance distribution are smoothed out considerably by diffusion.

An important fact to note in Fig. 3.5 is the dependence on the stellar mass of the outer layer chemical stratification expected in ZZ Ceti stars. Indeed, for the more massive models, diffusion has strongly modified the chemical abundance distribution,

eroding the intershell region by the time evolution has reached the domain of the ZZ Ceti instability strip. This is in contrast with the situation encountered in our less massive models, where the intershell region is not removed by diffusion. This is because element diffusion is less efficient in less massive models and also because the intershell is thicker, with the subsequent longer diffusion timescales. Regarding white dwarf asteroseismology, these are not minor issues, since the presence of a double-layered structure in the helium-rich layers is expected to affect the theoretical $g-$mode period spectrum of ZZ Ceti stars, as it does for pulsating DB (He-rich) white dwarf stars (Metcalfe et al., 2003). However, we mention that the thickness of the intershell region also depends somewhat on the number of thermal pulses during the AGB experienced by the progenitor star.

Finally, we have explored whether the shape of the He/H chemical interface has a dependence on the thickness of the H envelope. This is an important issue, because predictions of the exact value of the H envelope mass are tied to the precise mass loss history along the previous AGB and post-AGB phase, and particularly to the occurrence of late thermal pulses. We have generated additional, artificial sequences with H envelopes much thinner than those of our models. These sequences were created at high luminosities from a hot model with $M_* = 0.609 M_\odot$. This artificial procedure took place at luminosities high enough as to ensure that the models become physically sound at stages far before the domain of the ZZ Ceti stars. We found that diffusion rapidly leads to pure hydrogen envelopes, but the shape of the He/H chemical interfaces by the time evolution has proceeded to the ZZ Ceti stage, is almost the same independently of the thickness of the H envelope.

3.5 Pulsation properties: comparison with previous calculations

White dwarf asteroseismology is sensitive to the precise shape of the internal chemical profiles. The entire $g-$mode period spectrum and mode-trapping properties of pulsating white dwarfs are very sensitive to the fine details of the chemical profiles of both the core and the envelope of the star. This extreme sensitivity has been exploited with some success in several pulsation studies to infer the core chemical structure — e.g., Metcalfe (2003) for the case of pulsating DB white dwarfs — and the thickness of the He and H envelopes — e.g., (Bradley, 1998, 2001) for DAV stars.

In this section we perform a comparison between the pulsation properties derived from our new chemical profiles and those based on the most widely used chemical profiles in existing asteroseismological studies. To assess the adiabatic pulsation properties of our white dwarf models we employ the numerical code described in Córsico & Althaus (2006). We refer the reader to that paper for details. With the aim of simplifying our analysis, we elect a template DA white dwarf model with $M_* = 0.6096\, M_\odot$, $T_{\rm eff} \sim 12\,000$ K, and a thick hydrogen envelope ($M_{\rm H} \sim 10^{-4} M_*$). This is

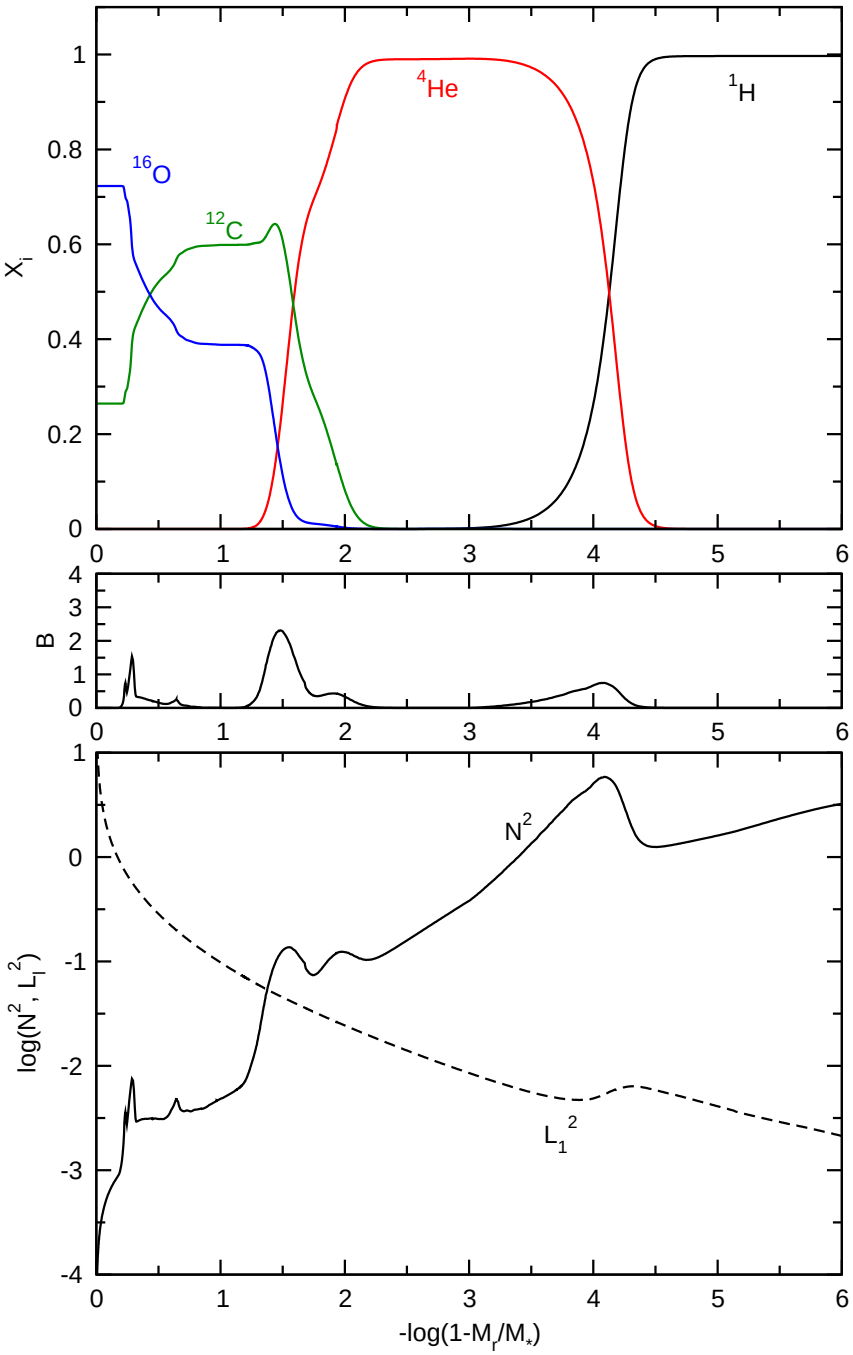

Figure 3.6: The internal chemical profile (upper panel), the Ledoux term B (middle panel), and the logarithm of the squaredBrunt-Väisälä (N) and Lamb (L_ℓ) frequencies (lower panel) in terms of the outer mass fraction ($-\log q$, where $q \equiv 1 - M_r/M_*$) for dipole modes ($\ell = 1$) corresponding to a DA white dwarf model with $M_* = 0.6096\,M_\odot$ and $T_{\rm eff} \sim 12\,000$ K.

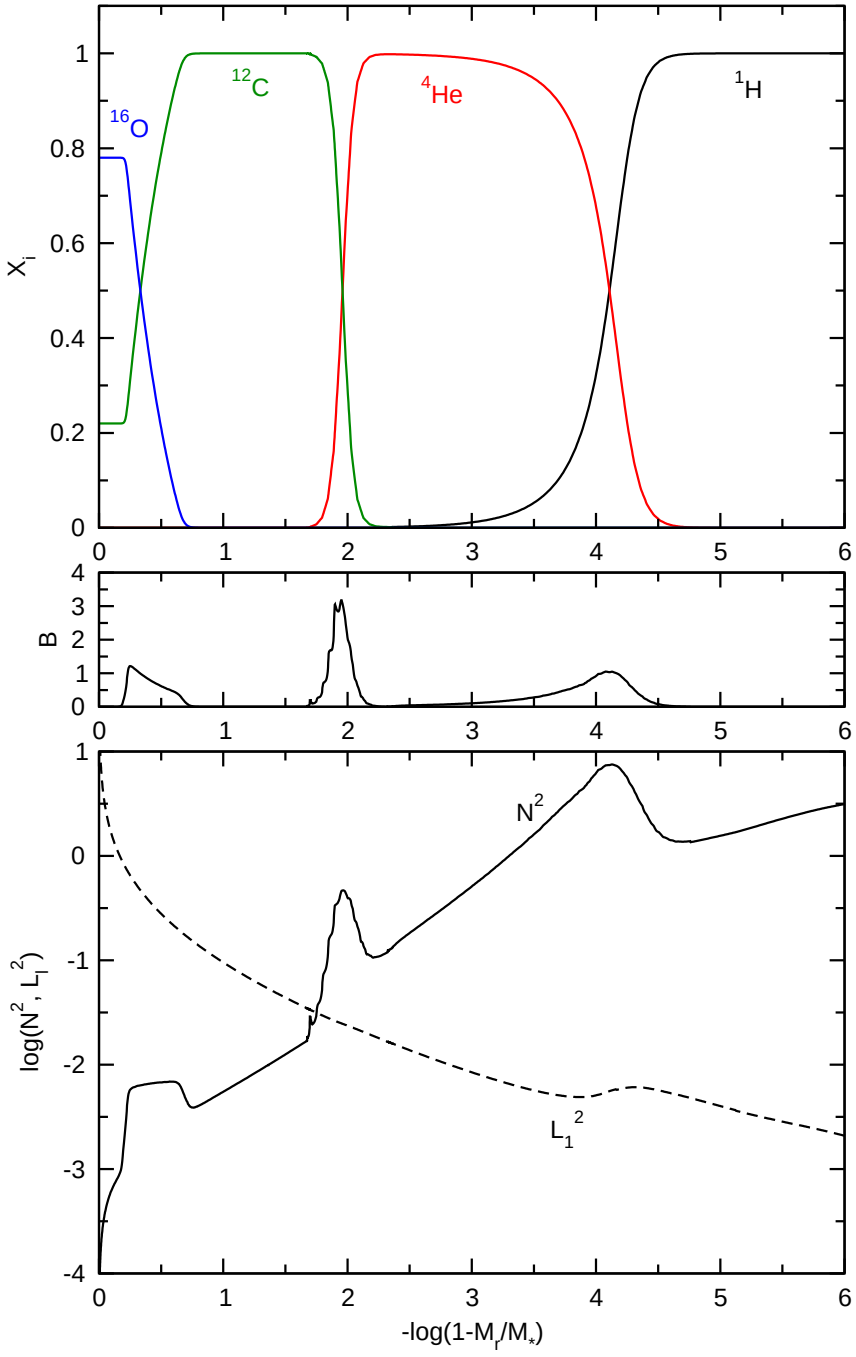

Figure 3.7: Same as in Fig. 3.6, but for the case of ramp-like core chemical profiles.

a canonical model of a DAV star with an average mass located in the middle of the observed ZZ Ceti instability strip. In Fig. 3.6 we depict the internal chemical profile (upper panel), the Ledoux term (middle panel), and the logarithm of the squared Brunt-Väisälä and Lamb frequencies (lower panel) for dipole modes corresponding to our template model. The Ledoux term and the Brunt-Väisälä frequency are computed as in Córsico & Althaus (2006). Our model is characterized by three chemical transition regions: a double chemical interface of oxygen and carbon located at the core region ($0.2 \lesssim -\log q \lesssim 0.8$), a triple chemical interface of oxygen, carbon, and helium located at $1.2 \lesssim -\log q \lesssim 2.3$, and finally, a double chemical interface of He/H located at $3.0 \lesssim -\log q \lesssim 4.5$. The core chemical profile is typical of situations in which extra mixing episodes beyond the fully convective core (like overshooting) during the core He burning phase are allowed to operate. The smoothness of the He/H chemical interface, on the other hand, is the result of the time-dependent element diffusion processes. The existence of these three chemical interfaces induces the "bumps" in the profile of the Brunt-Väisälä frequency. The number of these bumps, as well as their heights and widths, strongly affect the whole structure of the pulsation spectrum of the star.

In Fig. 3.7 we show the situation in which our template model is characterized by a ramp-like core chemical structure of the kind used by (Bradley, 1996, 1998, 2001) and more recently by Bischoff-Kim (2009). In this case the core chemical profile is not the result of stellar evolution calculations, but parameterized. This kind of chemical profiles has been widely employed in asteroseismology of white dwarfs because it allows a full exploration of the parameter space regarding the shape of the chemical abundance profiles in the core. The parameters are the central oxygen abundance ($X_{\rm O}$), the coordinate at which $X_{\rm O}$ starts to drop, and the coordinate at which $X_{\rm O}$ drops to zero — see, e.g., Bischoff-Kim et al. (2008). The overall shape of the core chemical profiles displayed in Fig. 3.7 is substantially simpler than that of the chemical profiles characterizing the model depicted in Fig. 3.6. Note the presence of a chemical transition region of C and He. This is at variance with the chemical profiles produced by `LPCODE`, which are characterized by a triple transition region of oxygen, carbon, and helium (see Fig. 3.6). The shape of the C/He chemical interface in this model is set by diffusion parameters, which were chosen to match the pulsation periods of G 117−B15A Bischoff-Kim et al. (2008). It is worth noting that this transition region produces the most prominent bump in the Brunt-Väisälä frequency (see the Ledoux term B in the central panel of Fig. 3.7). We mention that the presence of a thick pure carbon buffer like that assumed in these models is not expected from stellar evolution calculations. Finally, the He/H chemical transition region has been obtained by assuming equilibrium diffusion (Arcoragi & Fontaine, 1980), but without the trace element approximation — see Bischoff-Kim et al. (2008) for details. The shape of this interface is very similar to one based on time-dependent diffusion. It is worth noting, however, that the slight differences in the thickness and steepness of this chemical interface between

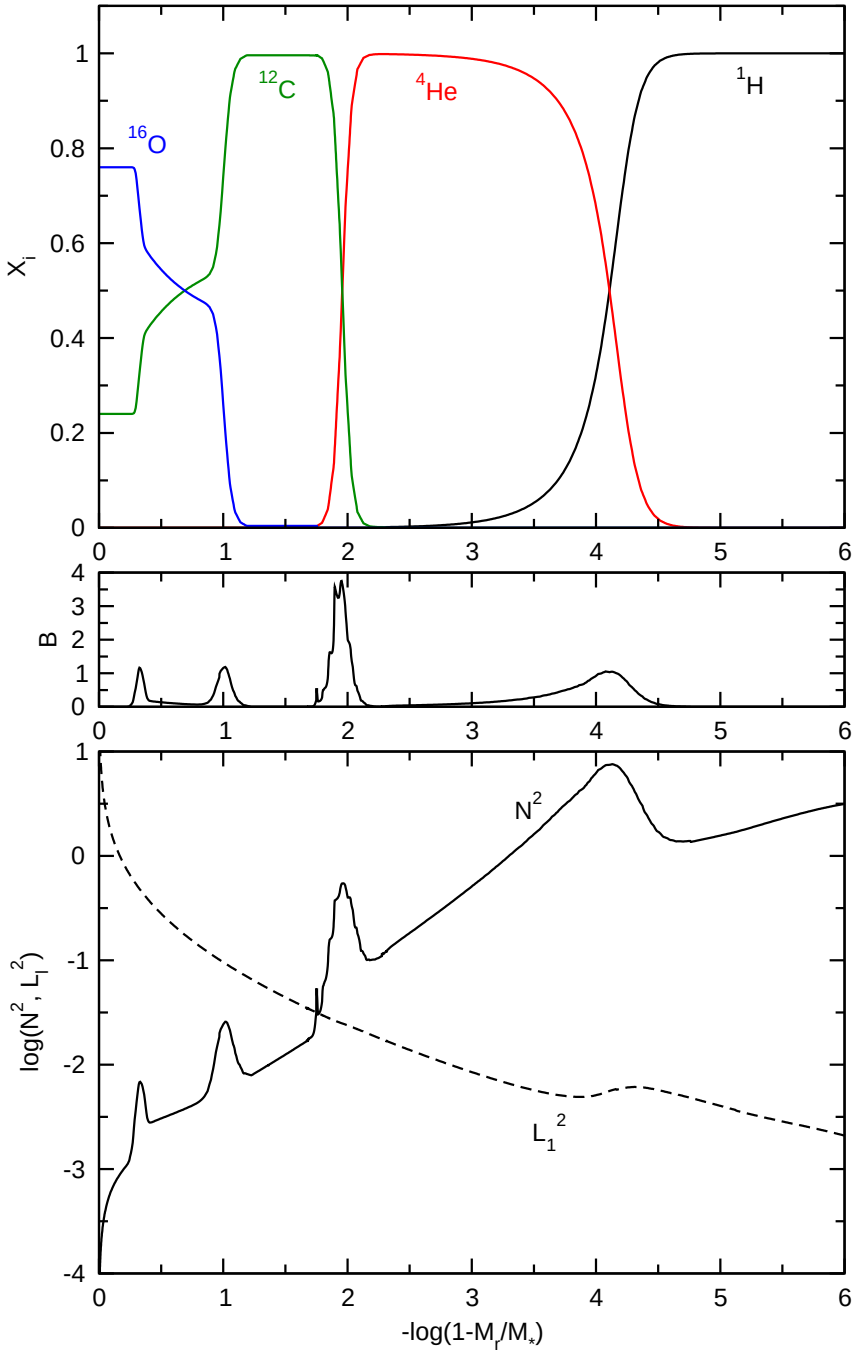

Figure 3.8: Same as in Fig. 3.6, but for the case of Salaris-like core chemical profiles.

the LPCODE model and the ramp-like model lead to a non-negligible contribution to the differences found in the period spacing (and the period themselves) of the models (see later in this section).

In Fig. 3.8 we display the case of a template model characterized by a Salaris-like core chemical structure. This kind of core chemical profiles was employed first by Córsico et al. (2001a), Córsico et al. (2002b) and Benvenuto et al. (2002b,a), and more recently in Bischoff-Kim et al. (2008). Actually, the core chemical profiles displayed in Fig. 3.8 and those used in Bischoff-Kim et al. (2008) are a close adaptation of the original chemical profiles of Salaris et al. (1997). Except for the core region, the rest of the chemical profiles in this model are the same as in the model depicted in Fig. 3.7. At variance with the template models described before, in this case there are two core chemical interfaces of oxygen and carbon instead of just one. This leads to four bumps in the Brunt-Väisälä frequency, as can be seen in the lower panel in Fig. 3.8.

Figures 3.6, 3.7, and 3.8 clearly reveal the profound differences existing between the chemical profiles and the run of the Brunt-Väisälä frequency of the model generated with LPCODE, i.e., by considering the full evolution of progenitor stars, and the two template models that incorporate the most widely used chemical profiles in past and current asteroseismological studies of ZZ Ceti stars. The differences are particularly noteworthy in the core chemical structure.

In what follows, we compare the pulsation properties of our template model with the models having core ramp-like and Salaris-like chemical profiles. The $\ell = 1$ asymptotic period spacing is largest for the LPCODE model (45.38 s), followed by the Salaris-like core chemical profile model (44.17 s) and by the ramp-like model (43.32 s). Since these models have the same stellar mass and effective temperature, the period and asymptotic period spacing differences are exclusively due to the differences in the chemical profiles at the core *and* the envelope of the three models. In particular, the subtle differences existing in the shape of the He/H interface resulting from time-dependent diffusion and that obtained from equilibrium diffusion give rise to a non-negligible contribution to the difference in the asymptotic period spacing.

If we now turn the argument around and imagine doing asteroseismological fits where we fix the chemical profiles to those found using LPCODE and allow the mass and effective temperature of the models to vary to give us a pulsation spectrum that matches that of an observed pulsating white dwarf, the asymptotic period spacing of the models will influence the mass and effective temperature of the best fits models. As it is well known, the hotter and more massive models have smaller asymptotic period spacings (for modes that are not strongly trapped). Since the asymptotic period spacing is larger for the LPCODE models, the best fit models would have to have larger mass and effective temperature to match a given observed asymptotic period spacing. As a result, we would expect to find asteroseismological fits that are more massive and hotter than current fits. This effect should mainly be observed for rich white dwarf pulsators, where we have a wealth of higher k (asymptotically

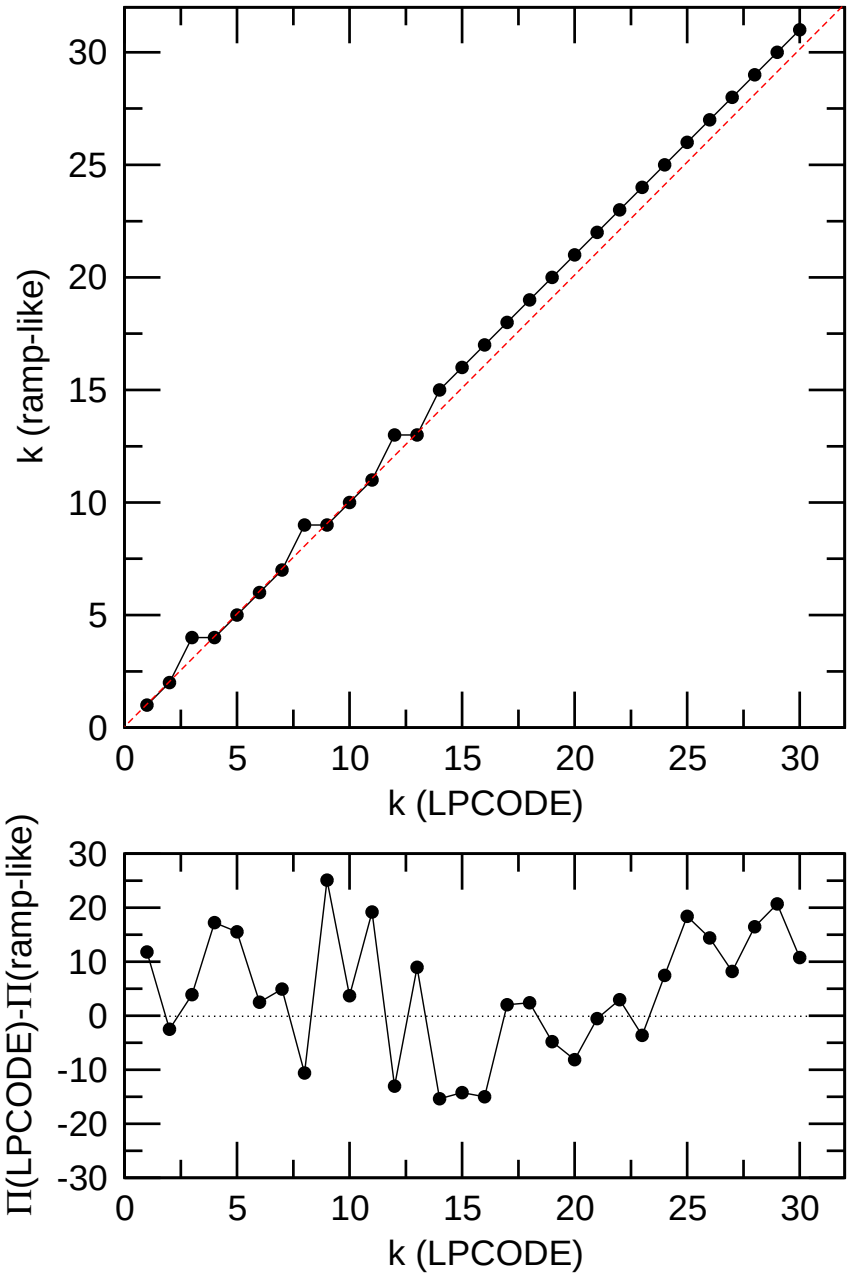

Figure 3.9: Comparison between the template model generated with `LPCODE` (Fig. 3.6) and the template model with ramp-like core chemical profiles (Fig. 3.7). The upper panel shows the differences in the k identification, and the lower panel depicts the differences between the matched periods.

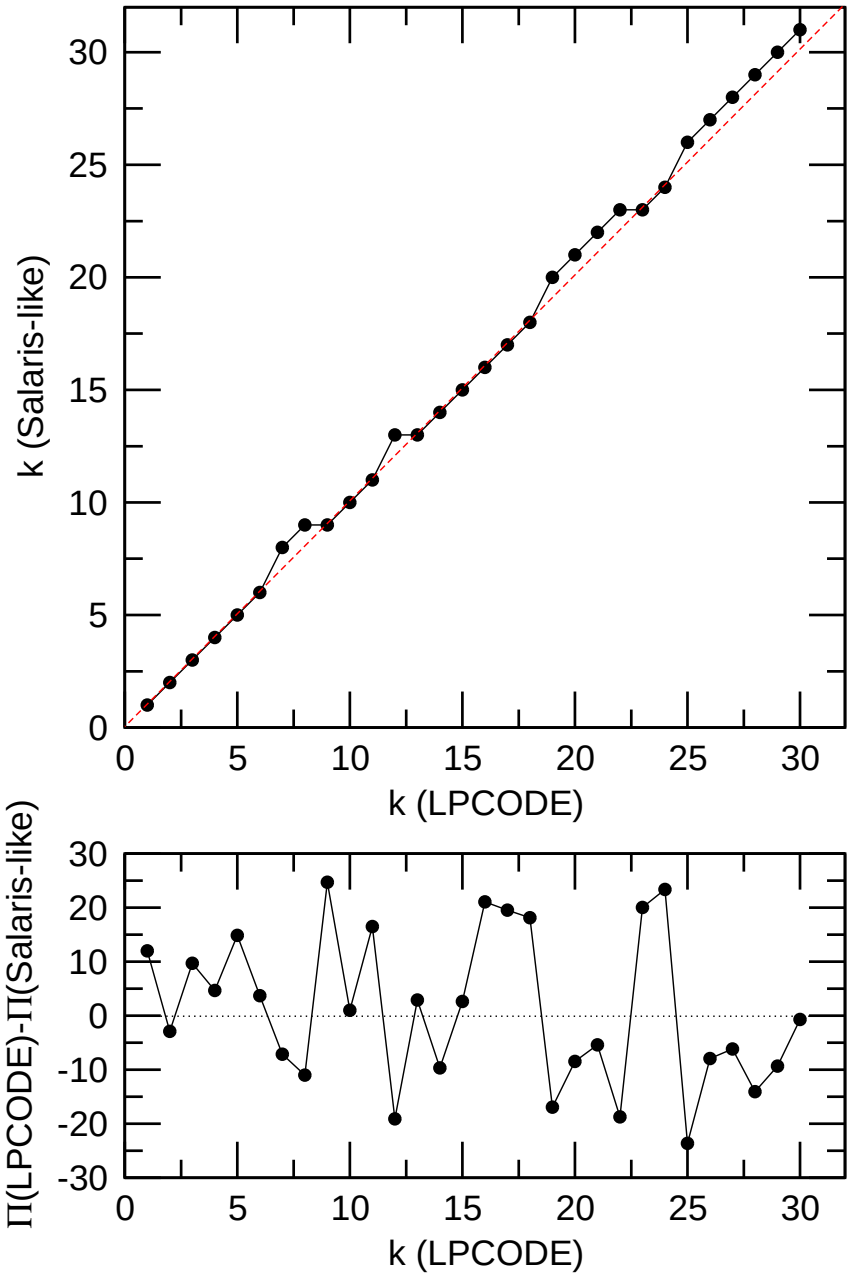

Figure 3.10: Same as in Fig. 3.9, but for the comparison between the template model generated with `LPCODE` (Fig. 3.6) and the template model with Salaris-like core chemical profiles (Fig. 3.8).

spaced) modes to fit. For G117−B15A, for instance, we cannot draw any conclusions from the asymptotic period spacings alone, as the only 3 modes observed have low radial overtone and are strongly trapped (Bischoff-Kim et al., 2008).

The higher period spacing for the LPCODE model leads to a drift to longer and longer periods as we work down the list of periods toward higher k modes. For instance, the cumulated effect of the 2.06 s difference between the LPCODE and the ramp-like models results in higher k periods to differ by as much as 65 seconds (for $k \sim 30$ if $\ell = 1$ and $k \sim 55$ if $\ell = 2$). The practical result in asteroseismological studies of such a drift to higher periods would be to lead to different k identifications of modes. In Figs. 3.9 and 3.10 we show how asteroseismological fits may be affected. In the upper panels, we show the differences in k identifications and in the bottom panels, how the period of the matched modes differ. Even allowing the k identifications to change to find the best match between the periods of the two models compared, we still find that some individual periods differ by as much as ~ 25 seconds.

We conclude our analysis by examining the forward period spacing ($\Delta\Pi_k \equiv \Pi_{k+1} - \Pi_k$) and the kinetic energy ($E_{\rm kin}$) of the three template models (Figure 3.11). The kinetic energy is computed according to Córsico & Althaus (2006). The horizontal lines in red correspond to the asymptotic period spacing. As it is well known, the presence of density gradients in the chemical transition regions in the interior of a white dwarf causes mode trapping (Winget et al., 1981; Brassard et al., 1992a; Córsico et al., 2002a). The signature of mode trapping on the period-spacing distribution is the presence of strong minima in a $\Delta\Pi_k - \Pi_k$ diagram, in contrast to the situation in which the star is chemically homogeneous — see, for instance, Córsico & Benvenuto (2002). Due to the presence of several chemical interfaces in the template models, we expect to find clear signatures of mode trapping.

For the model generated with LPCODE, the $\Delta\Pi_k$ distribution exhibits two primary minima and several secondary minima, as can be seen in the upper left panel of Figure 3.11. In the case of the model with ramp-like core chemical profiles (upper central panel) there are also primary and secondary minima, but the contrast amongst them is much less pronounced than in the case of the LPCODE model. Finally, in the case of the model with Salaris-like core chemical profiles (upper right panel) there is no clear distinction between primary and secondary minima of $\Delta\Pi_k$. That is, all the minima are very similar.

In spite of the complexity of the mode-trapping pattern exhibited by the template models, it is possible to make some rough inferences by examining the values of the kinetic energy of the modes (lower panels of Fig. 3.11). A close inspection of the plots reveals that each minimum of $\Delta\Pi_k$ is associated with a maximum in $E_{\rm kin}$ of a mode with the same radial order k or differing in $\Delta k = \pm 1$. Modes corresponding to local maxima in $E_{\rm kin}$ are modes partially confined to the core regions below the O/C and/or the C/He chemical interfaces (the O/C/He transition in the case of the LPCODE model), that is, modes with amplitudes relatively large even in very deep

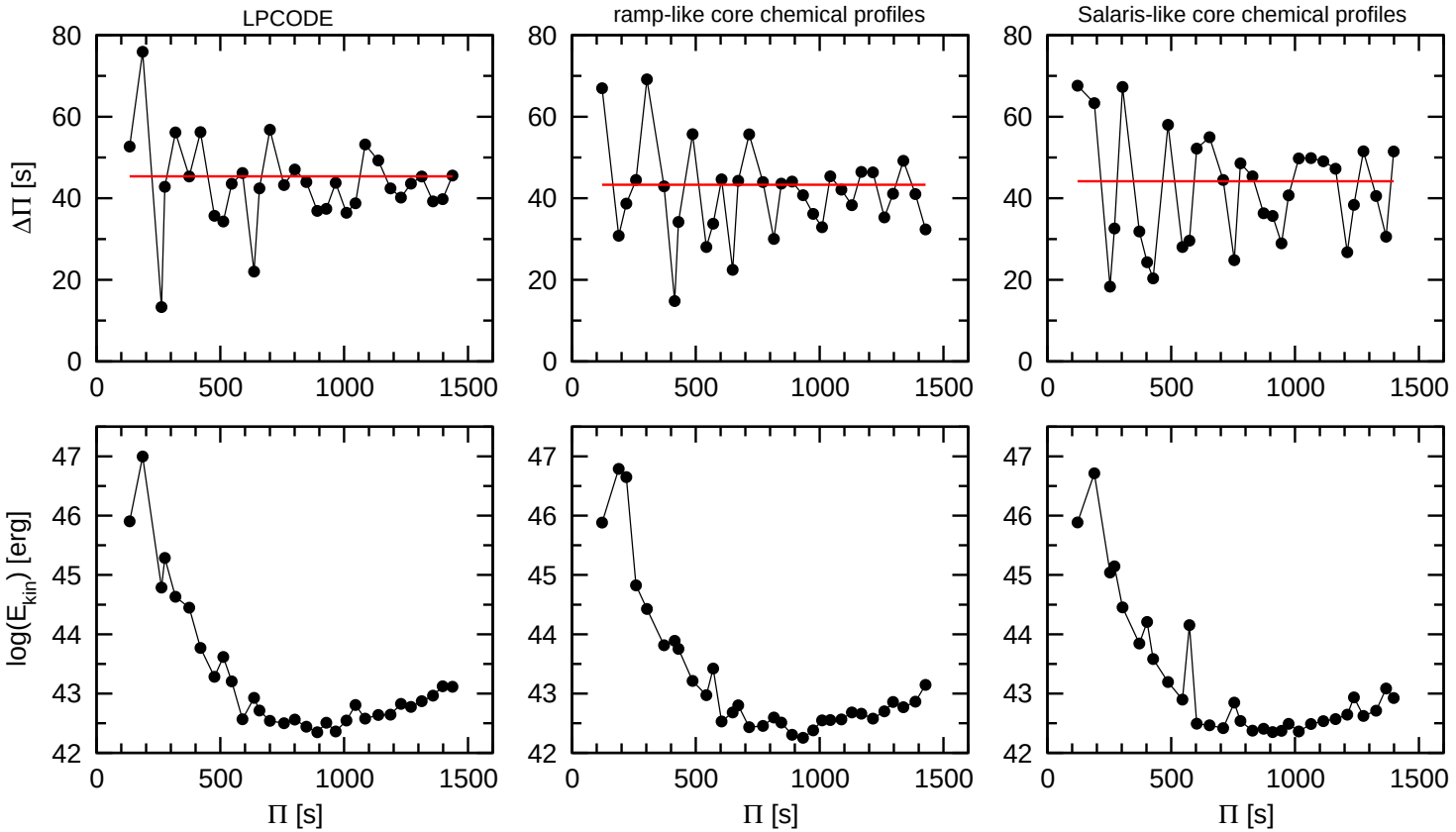

Figure 3.11: The upper panels show the forward period spacing and the lower panels depict the logarithm of the oscillation kinetic energy of $\ell = 1$ modes in terms of the pulsation periods. The horizontal lines in the upper panels display the asymptotic period spacing.

layers of the model. These modes are potentially useful from an asteroseismological point of view. The remaining modes (which have neither maxima nor minima kinetic energy values) are much less sensitive to the presence of the chemical transition regions, and so, they are of minor relevance for asteroseismolgy.

We conclude that the pulsation properties of DA white dwarf models that incorporate our new chemical profiles for the core and envelope substantially differ from those of models having the most commonly used chemical profiles. The important issue to be addressed now is to assess the impact of our new chemical profiles on asteroseismological period-to-period fits of real DAV stars. This step is beyond the scope of the present work, and we defer it to future studies.

3.6 Summary and conclusions

In this chapter we computed new chemical profiles for the core and envelope of white dwarfs appropriate for pulsational studies of ZZ Ceti stars. These profiles were derived from the full and complete evolution of progenitor stars from the zero age main sequence, through the thermally-pulsing and mass-loss phases on the asymptotic giant branch (AGB). These new profiles are intented for asteroseismological studies of ZZ Ceti stars that require realistic chemical profiles throughout the white dwarf interiors. In deriving the new chemical profiles, we employed the `LPCODE` evolutionary code, based on detailed and updated constitutive physics. Extra-mixing episodes during central hydrogen and helium burning, time-dependent element diffusion during the white dwarf stage and chemical rehomogenization of the inner carbon-oxygen composition by Rayleigh-Taylor instabilities were considered. The metallicity of progenitor stars is $Z = 0.01$.

We discussed at some length the importance of the initial-final mass relationship for the white dwarf carbon-oxygen composition. A reduction of the efficiency of extra-mixing episodes during the thermally-pulsing AGB phase, supported by different pieces of theoretical and observational evidence, yields a gradual increase of the hydrogen-free core mass as evolution proceeds during this phase. As a result, the initial-final mass relationship by the end of the thermally-pulsing AGB is markedly different from that resulting from considering the mass of the hydrogen free core right before the first thermal pulse. We found that this issue has implications for the carbon-oxygen composition expected in a white dwarf. In particular, the central oxygen abundance may be underestimated by about 15% if we assume the white dwarf mass to be the hydrogen-free core mass before the first thermal pulse. We also discuss the importance of the computation of the thermally-pulsing AGB and element diffusion for the chemical profiles expected in the outermost layers of ZZ Ceti stars. In this sense, we found a strong dependence of the outer layer chemical stratification on the stellar mass. In less massive models, the intershell region rich in helium and carbon — which is built during the mixing episode at the last AGB

thermal pulse — is not removed by diffusion by the time the ZZ Ceti stage is reached.

Finally, we performed adiabatic pulsation computations and discussed the implications of our new chemical profiles for the pulsational properties of ZZ Ceti stars. We found that the whole $g-$mode period spectrum and the mode-trapping properties of these pulsating white dwarfs as derived from our new chemical profiles are substantially different from those based on the most widely used chemical profiles in existing asteroseismological studies.

We expect the best fit parameters of asteroseismological studies using the `LPCODE` chemical profiles to differ significantly from those found in studies made so far. Further studies will show in what way, if we will solve the high mass problem with G117−B15A and Salaris-like core profiles (Bischoff-Kim et al., 2008) or find thicker hydrogen layers in asteroseismological fits, more in line with stellar evolution calculations Castanheira & Kepler (2008).

Chapter 4

^{22}Ne diffusion in white dwarfs with metal-rich progenitors

In this chapter we present new white dwarf evolutionary sequences appropriate for computing accurate ages for metal-rich clusters. We take into account not only the delays introduced by carbon-oxygen phase separation upon crystallization, but also the delay introduced by ^{22}Ne diffusion in the liquid at moderately high effective temperatures and luminosities. As it will be shown in the second part of this work, this is crucial for solving the discrepancies between the ages derived from fitting the main sequence turn-off and those obtained by fitting the termination of the white dwarf cooling sequence of some open, metal-rich, well populated, nearby clusters.

4.1 Introduction

The evolution of white dwarf stars is a relatively well-understood process that can be basically described as a simple cooling problem (Mestel, 1952) in which the decrease in the thermal heat content of the ions constitutes the main source of luminosity. Because of this, white dwarfs can be used as independent reliable cosmics clocks to date a wide variety of stellar populations. This fact has attracted the attention of numerous researchers over the years, who have devoted large efforts to study in detail the evolutionary properties of these stars. In particular, it is important to realize that an accurate determination of the rate at which white dwarfs cool down constitutes a fundamental issue. Detailed evolutionary models for these stars, based on increasing degrees of sophistication of their constitutive physics and energy sources, have proved to be valuable at determining interesting properties of many Galactic populations, including the disk (Winget et al., 1987; Garcia-Berro et al., 1988b; Hernanz et al., 1994; García-Berro et al., 1999), the halo (Isern et al., 1998; Torres et al., 2002) and globular and open clusters (Richer et al., 1997; von Hippel & Gilmore, 2000; Hansen et al., 2002; von Hippel et al., 2006; Hansen et al., 2007;

Winget et al., 2009). This important application of white dwarf stars has also been possible thanks to a parallel effort devoted to empirically determine the white dwarf cooling sequences of stellar clusters, as well to obtain the luminosity function of field white dwarfs, which also provides a measure of the white dwarf cooling rate.

Detailed models of white dwarfs require a complete treatment of the energy sources resulting from the core cyrstallization. In particular, the release of both latent heat (van Horn, 1968; Lamb & van Horn, 1975) and gravitational energy due to the change in chemical composition induced by crystallization (Stevenson, 1980; Garcia-Berro et al., 1988a; Segretain et al., 1994; Isern et al., 1997, 2000) affect considerably the cooling of white dwarfs. In particular, compositional separation at crystallization markedly slows down the cooling. This, in turn, influences, for instance, the position of the cut-off of the disk white dwarf luminosity function (Hernanz et al., 1994), which is essential in obtaining an independent determination of the age of the Galactic disk.

However, a new observational determination of the white dwarf luminosity function of the cluser NGC 6791 by Bedin et al. (2008a) casts serious doubts on the reliability of existing white dwarf evolutionary models and their use as accurate clocks. NGC 6791 is a very old (8 Gyr) and very metal-rich ([Fe/H] $\sim +0.4$) open cluster, for which Bedin et al. (2008a) have uncovered the faint end of the white dwarf cooling track, and have convincingly demonstrated the existence of a peak and a subsequent cut-off in the white dwarf luminosity function at $m_{\rm F606W} \approx 28.15$. Additionally, Bedin et al. (2008a) have found that the age of the cluster derived from the main sequence turn-off technique (8 Gyr) is in serious conflict with the age derived from the termination of the cooling sequence (6 Gyr). This discrepancy has strong implications for the theory of white dwarf evolution, and points out at a missing piece of physics in the conventional modeling of white dwarfs. In particular, Bedin et al. (2008a) have concluded that the white dwarfs in NGC 6791 have to cool markedly more slowly than believed in order to reproduce the faint peak and measured cut-off in the observed white dwarf luminosity function at the age of the cluster derived from the well-established main-sequence turn-off technique.

In view of the high metallicity characterizing NGC 6791 ($Z \approx 0.04$), a viable physical process that can decrease the cooling rate of white dwarfs appreciably is the slow gravitational settling of ^{22}Ne in the liquid phase. ^{22}Ne is the most abundant impurity expected in the carbon-oxygen interiors of typical white dwarfs. Its abundance by mass reaches $X_{\rm Ne} \approx Z_{\rm CNO}$, and it is the result of helium burning on ^{14}N — built up during the CNO cycle of hydrogen burning. As first noted by Bravo et al. (1992), the two extra neutrons present in the ^{22}Ne nucleus (relative to $A_i = 2Z_i$ nuclei, being A_i the atomic mass number and Z_i the charge) results in a net downward gravitational force of magnitude $2m_p g$, where g is the local gravitational acceleration and m_p is the proton mass. This leads to a slow, diffusive settling of ^{22}Ne in the liquid regions towards the center of the white dwarf. The role of ^{22}Ne sedimentation in the energetics of crystallizing white dwarfs was first addressed by

Isern et al. (1991) and more recently quantitatively explored by Deloye & Bildsten (2002) and García-Berro et al. (2008), who concluded that ^{22}Ne sedimentation releases sufficient energy to affect appreciably the cooling of massive white dwarfs, making them appear bright for very long periods of time, of the order of 10^9 yr. Deloye & Bildsten (2002) predicted that the possible impact of ^{22}Ne sedimentation on white dwarf cooling could be better seen in metal-rich clusters, such as NGC 6791, where the neon abundance expected in the cores of white dwarfs could be as high as $\sim 4\%$ by mass.

The effect of ^{22}Ne sedimentation is not included in any of the existing grids of white dwarf evolutionary calculations, and its effect on the evolution of white dwarfs resulting from supersolar metallicity progenitors has not been addressed. The only study of the effects of ^{22}Ne sedimentation in the cooling of white dwarfs using a complete stellar evolutionary code is that of García-Berro et al. (2008) for the case of solar metallicity. In this chapter, we present the first grid of full white dwarf evolutionary models resulting from metal-rich progenitors with masses ranging from 1 to 5 $M_{\odot}$ that includes both ^{22}Ne sedimentation and carbon-oxygen phase separation. This grid incorporates a much more elaborated and improved treatment of the physical processes relevant for the white dwarf evolution than that we considered in García-Berro et al. (2008). These improvements include, in addition to an update in the microphysics content, the derivation of starting white dwarf configurations obtained from a full calculation of the progenitor evolution, as well as a precise and self-consistent treatment of the energy released by the redistribution of carbon and oxygen due to phase separation during cystallization, which was lacking in our previous study. We find that the energy released by ^{22}Ne sedimentation markedly impacts the evolution of white dwarfs populating metal-rich clusters, and that this source of energy must be taken into account in deriving stellar ages from the white dwarf cooling sequence of such clusters. In particular, at the evolutionary stages where the faint peak and cut-off of the white dwarf luminosity function of NGC 6791 are observed, we find that the release of energy from both phase separation and ^{22}Ne sedimentation substantially slows down the cooling of white dwarfs. The occurrence of these physical separation processes in the core of cool white dwarfs and the associated slow down of the cooling rate has recently been demonstrated by García-Berro et al. (2010) to be a fundamental aspect to reconcile the age discrepancy in NGC 6791.

In this chapter there are three distinctive characteristics that allow us to obtain absolute ages for white dwarfs in metal-rich clusters. First, as already mentioned, the inclusion of the energy released from both ^{22}Ne sedimentation and carbon-oxygen phase separation is done self-consistently and locally coupled to the full set of equations of stellar evolution. In addition, realistic carbon-oxygen profiles expected in the cores of white dwarfs, of relevance for an accurate evaluation of the energy released by phase separation, are derived form the full computation of the evolution of progenitor stars. Finally, detailed non-gray model atmospheres are used to derive

the outer boundary conditions of our evolving sequences. All these facts allow us to obtain accurate ages. The chapter is organized as follows. In Sect. 4.2 we give a full account of the input physics of our evolutionary code, particularly the treatment of the energy sources. In Sect. 4.3 we present our results, and finally in Sect. 4.4 we summarize our findings and we draw our conclusions.

4.2 Details of computations

4.2.1 Input physics

Evolutionary calculations for both the white dwarfs and the progenitor stars were done with an updated version of the LPCODE stellar evolutionary code — see A, Althaus et al. (2005a) and references therein. This code has recently been employed to study different aspects of the evolution of low-mass stars, such as the formation and evolution of H-deficient white dwarfs, PG 1159 and extreme horizontal branch stars (Althaus et al., 2005a; Miller Bertolami & Althaus, 2006; Miller Bertolami et al., 2008; Althaus et al., 2009a), as well as the evolution of He-core white dwarfs with high metallicity progenitors (Althaus et al., 2009b). It has also been used to study the initial-final-mass relation (Salaris et al., 2009), where a test and comparison of LPCODE with other evolutionary codes has also been made. Details of LPCODE can be found in these works. In what follows, we comment on the main input physics that are relevant for the evolutionary calculations presented in this work.

The radiative opacities considered in LPCODE are from the OPAL project (Iglesias & Rogers, 1996), including C- and O-rich composition, supplemented at low temperatures with the molecular opacities of Alexander & Ferguson (1994). During the white dwarf regime, the metal mass fraction Z in the envelope is not assumed to be fixed. Instead, it is specified consistently according to the prediction of element diffusion. To account for this, we have considered radiative opacities tables from OPAL for arbitrary metallicities. For effective temperatures less than 10 000 K we have included the effects of molecular opacitiy by assuming pure hydrogen composition from the computations of Marigo & Aringer (2009). This assumption is justified because element diffusion leads to pure hydrogen envelopes in cool white dwarfs. It is worth noting that these opacity calculations do not cover the high-density regime characteristic of the envelopes of cool white dwarfs. Nevertheless, because the derivation of the outer boundary conditions for our evolving models involves the integration of detailed non-gray model atmospheres down to very large optical depths ($\tau = 25$) these opacities are only required at large τ and low effective temperatures. However, at the high densities reached at the end of the atmospheric integration, energy transfer is mainly by convection, which at such depths is essentially adiabatic. Indeed, we find that at $\tau = 25$, the radiative flux amounts to 4% at most. Consequently, the temperature stratification characterizing these deep layers becomes strongly tied to the equation of state, so a detailed knowledge of the radiative opacity becomes

almost irrelevant. The conductive opacities are those of Cassisi et al. (2007), and the neutrino emission rates are taken from Itoh et al. (1996) and Haft et al. (1994). For the high-density regime characteristic of white dwarfs, we have used the equation of state of Segretain et al. (1994), which accounts for all the important contributions for both the liquid and solid phases — see Althaus et al. (2007) and references therein. We have also considered the abundance changes resulting from element diffusion in the outer layers of white dwarfs. As a result, our sequences develop pure hydrogen envelopes, the thickness of which gradually increases as evolution proceeds. We have considered gravitational settling and thermal and chemical diffusion, see Althaus et al. (2003) for details. In `LPCODE`, diffusion becomes operative once the wind limit is reached at high effective temperatures (Unglaub & Bues, 2000). Chemical rehomogenization of the inner carbon-oxygen profile induced by Rayleigh-Taylor instabilities has been considered following Salaris et al. (1997). These instabilities arise because the positive molecular weight gradients that remain above the flat chemical profile left by convection during helium core burning.

Finally, we employ outer boundary conditions for our evolving white dwarf models as provided by detailed non-gray model atmospheres that include non-ideal effects in the gas equation of state and chemical equilibrium based on the occupation probability formalism. The level occupation probabilities are self-consistently incorporated in the calculation of the line and continuum opacities. Model atmospheres also consider collision-induced absorption due to H_2-H_2, H_2-He, and H-He pairs, and the Lyα quasi-molecular opacity that result from perturbations of hydrogen atoms by interactions with other particles, mainly H and H_2. These model atmospheres have been developed by Rohrmann et al. (2002) and Rohrmann et al. (2011), and we refer the reader to those works and to Chap. 2, as well as to Renedo et al. (2010)) for a full description of them. In the interest of reducing computing time, we have computed from these models a grid of pressure, temperature, radial thickness and outer mass fraction values at an optical depth $\tau = 25$ from which we derive the outer boundary conditions. At advanced stages of white dwarf evolution, the central temperature becomes strongly tied to the temperature stratification of the very outer layers, thus the employment of non-gray model atmospheres is highly desired for an accurate assessment of cooling times of cool white dwarfs (Prada Moroni & Straniero, 2007). Our model atmoshperes also provide detailed colors and magnitudes for effective temperatures lower than 60 000 K for a pure hydrogen composition and for the HST ACS filters (Vega-mag system) and $UBVRI$ photometry.

The energy contribution resulting from the gravitational settling of ^{22}Ne is treated in a similar way as it was done in García-Berro et al. (2008), except that now we have assumed that the liquid behaves as a single backgroung one-component plasma consisting of the average by number of carbon and oxygen — the inner chemical composition expected in a real white dwarf — plus traces of ^{22}Ne. This allows us to treat the problem of ^{22}Ne diffusion in a simple and realistic way. The slow change in the ^{22}Ne chemical profile and the associated local contribution to the luminosity

equation is provided by an accurate treatment of time-dependent ^{22}Ne diffusion — see García-Berro et al. (2008) for details. In particular, the diffusion coefficient $D_{\rm s}$ in the liquid interior is given by (Deloye & Bildsten, 2002):

$$D_{\rm s} = 7.3 \times 10^{-7} \frac{T}{\rho^{1/2} \overline{Z}\ \Gamma^{1/3}}\ {\rm cm}^2/{\rm s}, \tag{4.1}$$

where we have considered a mean charge $\overline{Z}$ of the background plasma. For those regions of the white dwarf that have crystallized, diffusion is expected to be no longer efficient due to the abrupt increase in viscosity expected in the solid phase. Thus, we set $D = 0$ in the crystallized regions.

In a subsequent phase we have also considered the energy sources resulting from the crystallization of the white dwarf core, i.e., the release of latent heat and the release of gravitational energy associated with carbon-oxygen phase separation induced by crystallization. In `LPCODE`, these energy sources are included self-consistently and are locally coupled to the full set of equations of stellar evolution. In particular, the standard luminosity equation

$$\frac{\partial L_r}{\partial M_r} = \varepsilon_{\rm nuc} - \epsilon_\nu - C_P \frac{dT}{dt} + \frac{\delta}{\rho} \frac{dP}{dt}, \tag{4.2}$$

had to be modified. In Eq. (4.2), $\varepsilon_{\rm nuc}$ and ϵ_ν denote, respectively, the energy per unit mass per second due to nuclear burning and neutrino losses, and the third and fourth terms are the well-known contributions of the heat capacity and pressure changes to the local luminosity of the star (Kippenhahn & Weigert, 1990). We have simplified the treatment of phase separation, by ignoring the presence of ^{22}Ne. As shown by Segretain (1996), ^{22}Ne influences the phase diagram at the late stages of crystallization, and the impact on the cooling time is moderate and much smaller than that resulting from carbon-oxygen phase separation. Thus, to compute the energy resulting from phase separation, we assume that the white dwarf interior is made only of carbon and oxygen with abundance by mass $X_{\rm C}$ and $X_{\rm O}$ respectively ($X_{\rm C} + X_{\rm O} = 1$). Then, it can be shown (García-Berro et al., 2008) that

$$\begin{aligned} \frac{\partial L_r}{\partial M_r} = \varepsilon_{\rm nuc} - \epsilon_\nu - C_P \frac{dT}{dt} + \frac{\delta}{\rho} \frac{dP}{dt} + & \quad l_{\rm s} \frac{dM_{\rm s}}{dt} \delta(m - M_{\rm s}) \\ & - A \frac{dX_{\rm O}}{dt} \end{aligned} \tag{4.3}$$

where A is given by

$$A = \left(\frac{\partial u}{\partial X_{\rm O}} \right)_{\rho,T} + \frac{\delta}{\rho} \left(\frac{\partial P}{\partial X_{\rm O}} \right)_{\rho,T} \approx \left(\frac{\partial u}{\partial X_{\rm O}} \right)_{\rho,T}, \tag{4.4}$$

being u the internal energy per gram.

The fifth term in Eq. (4.3) is the local contribution of latent heat: $l_{\rm s}$ is the latent heat of crystallization and $dM_{\rm s}/dt$ is the rate at which the solid core grows. The delta function indicates that the latent heat is released at the solidification front. The last term in Eq. (4.3) represents the energy released by chemical abundance changes. Although this term is usually small in normal stars, since it is much smaller than the energy released by nuclear reactions, it plays a major role in crystallizing white dwarfs, with important energetic consequences due to carbon-oxygen phase separation. In the case of carbon-oxygen mixtures, $(\partial u/\partial X_{\rm O})_{\rho,T}$ is dominated by the ionic contributions, and is negative. Hence, the last term in Eq. (4.3) will be a source (sink) of energy in those regions where the oxygen abundance increases (decreases). During the crystallization of a carbon-oxygen white dwarf, the oxygen abundance in the crystallizing region increases, and the overlying liquid mantle becomes carbon-enriched as a result of a mixing process induced by a Rayleigh-Taylor instability at the region above the crystallized core. Thus, according to Eq. (4.3), phase separation will lead to a source of energy in those layers that are crystallizing, and to a sink of energy in the overlying layers. We computed the resulting chemical rehomogenization following the prescription by Salaris et al. (1997), see also Montgomery et al. (1999).

To implement the energy release by phase separation in our code in a suitable formalism, and to avoid numerical difficulties when integrating the full set of equations of stellar structure and evolution, we have considered the *net* energy released by the process of carbon-oxygen phase separation over a time interval dt, by integrating the last term in Eq. (4.3) over the whole star. Because cooling is a slow process, it can be shown that (Isern et al., 1997):

$$\int_0^M \left(\frac{\partial u}{\partial X_{\rm O}}\right) \quad \frac{dX_{\rm O}}{dt}\, dM_r = (X_{\rm O}^{\rm sol} - X_{\rm O}^{\rm liq}) \times \left[\left(\frac{\partial u}{\partial X_{\rm O}}\right)_{M_{\rm s}} - \left\langle \frac{\partial u}{\partial X_{\rm O}} \right\rangle\right] \frac{dM_{\rm s}}{dt} \tag{4.5}$$

where $(\partial u/\partial X_{\rm O})_{M_{\rm s}}$ is evaluated at the boundary of the solid core and

$$\left\langle \frac{\partial u}{\partial X_{\rm O}} \right\rangle = \frac{1}{\Delta M} \int_{\Delta M} \left(\frac{\partial u}{\partial X_{\rm O}}\right) dM_r. \tag{4.6}$$

The first term in the square bracket in Eq. (4.5) represents the energy released in the crystallizing layer, and the second term, given by Eq. (4.6), is the energy absorbed on average in the convective region (ΔM) driven by the Rayleigh-Taylor instability above the cyrstallization front. Since $(\partial u/\partial X_{\rm O})$ is negative and essentially depends on the density (which decreases outwards), the square bracket is negative, and thus the process of phase separation results in a net release of energy during the time interval dt. It is clear that the energy released by this process will depend

on the intial oxygen profile at the beginning of the white dwarf phase, resulting in a smaller contribution in the case of initially higher oxygen abundances. Note that the shape of the initial chemical profile may also affect the degree of mixing in the liquid layers and thus the energy absorbed there, hence altering the net energy released by the process.

For computational purposes, we proceed as follows. At each evolutionary time step, we compute the change of chemical composition resulting from carbon-oxygen phase separation using the spindle-type phase diagram for a carbon-oxygen mixture of Segretain & Chabrier (1993). Then, we evaluate the net energy released by this process during the time step from Eq. (4.5). This energy is added to the, usually smaller, latent heat contribution, of the order of $0.77 k_{\rm B} T$ per ion. The resulting energy is distributed over a small mass range around the crystallization front, and the resulting local contribution is added to the luminosity equation, Eq. 4.2. Finally, we also add to this equation the contribution from ^{22}Ne sedimentation in the same way as in García-Berro et al. (2008). The `LPCODE` stellar evolutionary code solves iteratively the full set of equations for the white dwarf evolution with the luminosity equation modified as previously explained. We mention that the magnitude of these energy sources is calculated at each iteration during the convergence of the model. In our calculations, crystallization sets in when the ion coupling constant reaches $\Gamma = 180$, where $\Gamma \equiv \langle Z^{5/3} \rangle e^2 / a_{\rm e} k_{\rm B} T$ and $a_{\rm e}$ is the interelectronic distance.

Finally, we want to mention that our treatment is not entirely consistent in the sense that the energy resulting from ^{22}Ne sedimentation is evaluated separately and independently of the ^{22}Ne abundances changes induced by crystallization. However, as shown by Segretain (1996), the neon concentration is expected to change appreciably only when $\sim 70\%$ of the white dwarf has crystallized. Because the luminosity contribution from ^{22}Ne sedimentation strongly declines by the time a large fraction of the mass of the white dwarf has crystallized, we expect that this inconsistency in our treatment is not relevant. In any case, it should be noted that this picture could change appreciably for the case of larger initial neon abundances than that considered in Segretain (1996).

4.2.2 Evolutionary sequences

As mentioned, initial models for our white dwarf sequences have been derived from full evolutionary calculations of progenitor stars for solar metallicity see Chap 2 and Renedo et al. (2010). All the sequences have been computed from the ZAMS through the thermally-pulsing and mass-loss phases on the AGB and, finally, to the domain of planetary nebulae. Extra-mixing episodes beyond the pulse-driven convection zone have been disregarded during the thermally-pulsing AGB phase, as suggested by different and recent studies — see Salaris et al. (2009), and Weiss & Ferguson (2009), and references therein. As a result, the efficiency of the third dredge-up episode is strongly reduced for the low-mass sequences (but not for the massive ones), and thus

the mass of the hydrogen-free core of our less massive sequences gradually grows as evolution proceeds through this stage. A strong reduction of extra-mixing during the AGB phase and the resulting reduction in the efficiency of third dredge-up episodes in low-mass stars is in agreement with observational inferences of AGB carbon stars, the luminosities of which, in turn, are in good agreement with those predicted by stellar models using the Schwarzschild's criterion for convection (Guandalini et al., 2006). The breathing pulse instability occurring towards the end of core helium burning was suppressed — see Straniero et al. (2003) for a thorough discussion on this issue. We considered mass-loss episodes during the stages of core helium burning and red giant branch following Schröder & Cuntz (2005), whereas during the AGB and thermally-pulsing AGB phases we used the mass-loss prescription of Vassiliadis & Wood (1993). In the case of a strong reduction of the third dredge-up efficiency, as occurs in our less massive sequences, mass loss plays a major role in determining the final mass of the hydrogen-free core at the end of the TP-AGB evolution, and thus the initial-final mass relation (Weiss & Ferguson, 2009). However, we stress that the initial-final mass relation obtained from our sequences (Renedo et al., 2010) is in very good agreement with the semi-empirical determination of this relation of Salaris et al. (2009) and with that of Catalán et al. (2008a). Finally, we mention that the hydrogen envelope massses of our sequences should be considered as upper limits to the maximum mass of hydrogen left in a white dwarf resulting from the evolution of single star progenitors. This stems from the fact that the occurrence of a late thermal pulse after departure from the TP-AGB may reduce the hydrogen mass considerably, see Althaus et al. (2005b). Hence, this could alter the quantitative effect of ^{22}Ne sedimentation on the white dwarf cooling.

The computation of the progenitor evolution provides realistic initial models and, more importantly, detailed carbon-oxygen chemical profiles, which are relevant for a proper computation of the energy released by carbon-oxygen phase separation. In Fig. 4.1 we show the mass abundances of ^{1}H, ^{4}He, ^{12}C and ^{16}O throughout the deep interior of a selected $0.7051\,M_{\odot}$ white dwarf model at an evolutionary stage where element diffusion has already strongly modified the initial outer layer chemical stratification, leading to the formation of a thick pure hydrogen envelope plus an extended inner tail. Below the hydrogen envelope there is the helium buffer and an intershell rich in helium, carbon and oxygen. Finally, the innermost region is composed mainly of carbon and oxygen, plus traces of heavier element of which ^{22}Ne is the most abundant one. As previously mentioned, ^{22}Ne is the result of helium burning on ^{14}N via the reactions $^{14}\mathrm{N}(\alpha,\gamma)^{18}\mathrm{F}(\beta^{+})^{18}\mathrm{O}(\alpha,\gamma)^{22}\mathrm{Ne}$. The core chemical profile of our model is typical of situations in which extra mixing episodes beyond the fully convective core during the core He burning are allowed — see Straniero et al. (2003) and also Prada Moroni & Straniero (2007) for the consequences on white dwarf evolution. The flat chemical profile towards the center is the result of the chemical rehomogenization induced by Rayleigh-Taylor instabilities.

Here, we have considered two initial ^{22}Ne abundances of $X_{\rm Ne} \approx Z_{\rm CNO} \approx 0.03$ and

Table 4.1: Initial and final stellar mass (in solar units), and the central oxygen abundance (mass fraction) of our starting white dwarf sequences. The progenitor metallicity is $Z = 0.01$.

$M_{\rm WD}$	$M_{\rm ZAMS}$	$X_{\rm O}$
0.5249	1.00	0.70
0.5701	1.50	0.68
0.5932	1.75	0.70
0.6096	2.00	0.72
0.6323	2.25	0.75
0.6598	2.50	0.72
0.7051	3.00	0.66
0.7670	3.50	0.65
0.8779	5.00	0.61

0.06. These elections are not entirely consistent with the almost solar metallicity we assumed for the progenitor stars, $Z = 0.01$. This introduces a slight inconsistency however, since only a minor difference is expected in the oxygen composition and in the white dwarf evolution when progenitors with different metallicities are considered (Prada Moroni & Straniero, 2002; Salaris et al., 2010). Thus, to a good approximation, our starting models are representative of white dwarf stars with progenitors having supersolar metallicity. However, we mention that a significant change in the metallicity progenitor could affect the AGB evolution and mass-loss history, as well as the initial-final mass relation. In this work, we computed white dwarf sequences with hydrogen-rich envelopes for ^{22}Ne abundances of 0.03 and 0.06, taking into account the energy contributions from ^{22}Ne sedimentation and carbon-oxygen phase separation. We compute also additional sequences to assess the impact of these energy sources. This includes the computation of the evolution of a $1.0\,M_{\odot}$ white dwarf sequence that was started, in contrast to the other sequences, from an artificially-generated initial model, and with a carbon-oxygen composition similar to that of the $0.8779\,M_{\odot}$ sequence. In this way, our sequences cover the entire white dwarf mass interval for which a carbon-oxygen core is expected to be formed. In Table 4.1 we list the stellar masses of the white dwarfs for which we compute their progenitor evolution, together with the inital masses of the progenitor stars at the ZAMS. Also listed in Table 4.1 is the central oxygen abundance at the beginning of the white dwarf evolutionary track. These sequences were computed from the pre-white dwarf stage down to $\log(L/L_{\odot}) \approx -5.3$. To explore the relevance for the cooling times of uncertainties in the actual value of the diffusion coefficient of ^{22}Ne (Deloye & Bildsten, 2002), we compute additional cooling sequences altering the diffusion coefficient by a factor of 2. Finally, we find worthwhile to assess the lowest metallicity for which

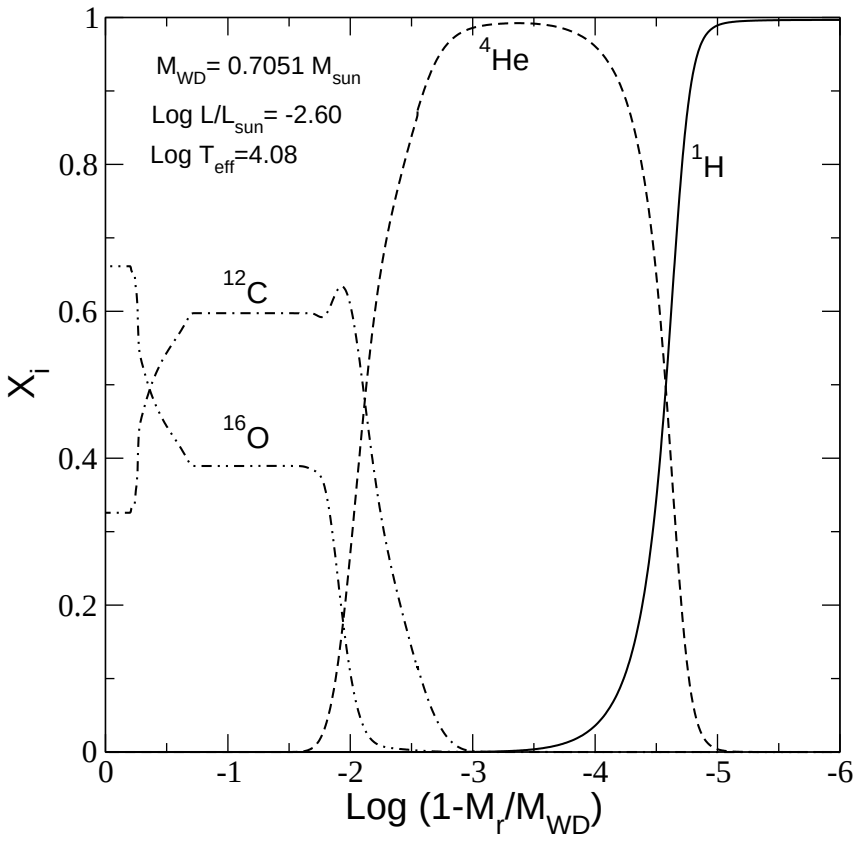

Figure 4.1: The chemical abundance distribution (carbon, oxygen, hydrogen and helium) for a selected 0.7051 $M_{\odot}$ white dwarf model after element diffusion has led to the formation of a pure hydrogen envelope.

^{22}Ne sedimentation starts to affect significantly the cooling times of white dwarfs. To this end, we compute additional cooling sequences for initial ^{22}Ne abundances of 0.01 and 0.005.

4.3 Results

The results presented in this work are based on a complete and consistent treatment of the different energy sources that influence the evolution of white dwarfs along the distinct evolutionary stages. The ultimate aim is to provide cooling ages as accurate as possible, according to our best knowledge of the physical processes that drive the evolution of these stars. In particular, we compute here the first grid of white dwarf evolutionary sequences that incorporates the sedimentation of ^{22}Ne. The grid is intended for applications to white dwarfs with high ^{22}Ne abundances in their cores,

namely, those resulting from metal-rich progenitors, for which ^{22}Ne sedimentation is expected to impact their evolution — see Chap 4 and Chap 5, as well as García-Berro et al. (2010) and García-Berro et al. (2011).

As shown by Deloye & Bildsten (2002) and García-Berro et al. (2008), ^{22}Ne sedimentation is a slow process that impacts the evolution of white dwarfs only after long enough times have elapsed. During the evolutionary stages where most of the white dwarf remains in a liquid state, this process causes a strong depletion of ^{22}Ne in the outer region of the core, and an enhancement of its abundance in the central regions of the star. This behavior becomes susbtantially more noticeable as the gravity is increased. Indeed, a more rapid sedimentation and a faster depletion of ^{22}Ne in the outer layers is expected in massive white dwarfs. However, because massive white dwarfs crystallize earlier than less massive ones, ^{22}Ne sedimentation will stop at higher effective temperatures as compared with less massive white dwarfs, thus limiting the extent to which ^{22}Ne diffusion constitutes an energy source for the star. This is a critical issue regarding the cooling behavior of massive white dwarfs.

As expected, the contribution of ^{22}Ne sedimentation to the luminosity budget of white dwarfs becomes larger as the metal content of the parent star is increased. This is exemplified in Fig. 4.2, which shows the resulting luminosity contribution (expressed in solar units) in terms of the effective temperature of the white dwarf for the 0.7051 and the 0.5249 $M_{\odot}$ sequences (upper and bottom panel, respectively) and for the two metallicities adopted in this work, $Z = 0.03$ and 0.06. This figure gives us a deep insight of the importance of ^{22}Ne sedimentation into the global energetics during the entire white dwarf evolution. Note that the contribution from this process to the star luminosity is notably enhanced in the case of more massive white dwarfs. Moreover, after the onset of core crystallization ^{22}Ne sedimentation is still a relevant process. As the core becomes increasingly crystallized, the luminosity due to ^{22}Ne sedimentation declines steeply (at higher effective temperatures in more massive white dwarfs). For low-mass white dwarfs, the impact of ^{22}Ne sedimentation is markedly less noticeable, albeit not negligible in the case of high Z. In Fig. 4.2, we also display with thin solid lines the luminosity contribution that results from carbon-oxygen phase separation. It can been seen that, depending on the stellar mass and metal content, the contribution of ^{22}Ne sedimentation to the energetics is comparable or larger than that resulting from carbon-oxygen phase separation.

It is clear that ^{22}Ne sedimentation plays a major role in the energetics of cool white dwarfs characterized by a high metal content in their interiors. The impact of this process as well as of latent heat and carbon-oxygen phase separation in the white dwarf cooling ages can be seen in Figs. 4.3 and 4.4 for the case of $Z = 0.03$ and 0.06, respectively. Here, the white dwarf surface luminosity is shown as a function of the age. In each figure, the upper and bottom panles correspond to the 0.5249 and 0.7051 $M_{\odot}$ sequences, respectively. The solid line corresponds to the standard case in which latent heat is considered, and carbon-oxygen phase separation and ^{22}Ne sedimentation are neglected. The inclusion of ^{22}Ne sedimentation strongly modifies

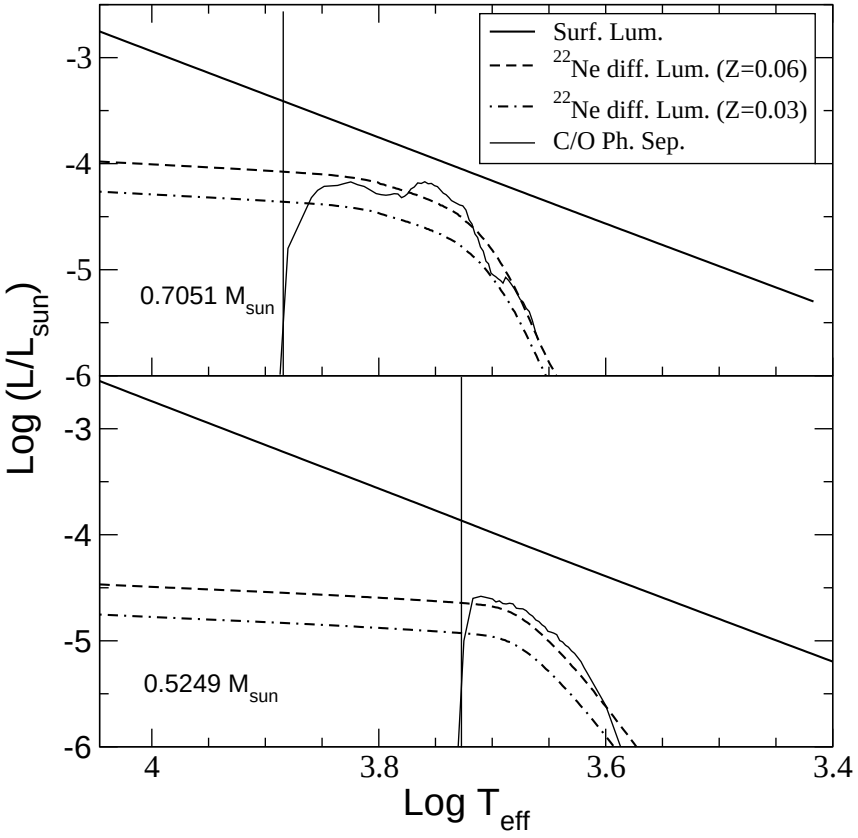

Figure 4.2: Luminosity contribution in solar units due to ^{22}Ne sedimentation versus effective temperature for the 0.7051 and 0.5249 $M_{\odot}$ white dwarf sequences (upper and bottom panel, respectively), and for $Z = 0.06$ and 0.03 (dashed and dot-dashed lines) respectively. The solid line displays the surface luminosity, and the thin solid line the luminosity contribution from carbon-oxygen phase separation. The vertical line marks the effective temperature for the onset of core crystallization.

the cooling curves — dashed lines. Finally, the addition of the energy resulting from carbon-oxygen phase separation upon cyrstallization (and ^{22}Ne sedimentation) gives rise to the cooling curve shown in dot-dashed line. Clearly, the energy released by ^{22}Ne sedimentation markedly influences the cooling times, particularly those of the more massive white dwarfs. Note that in this case, the magnitude of the delays in the cooling rates resulting from ^{22}Ne sedimentation are comparable (or even much larger in the case of $Z = 0.06$) to the delays induced by carbon-oxygen phase separation.

According to what we have discussed, the signatures of ^{22}Ne sedimentation in the cooling rate will certainly be different depending on the mass of the white dwarf. In particular, because of their larger gravities, they start to manifest themselves earlier

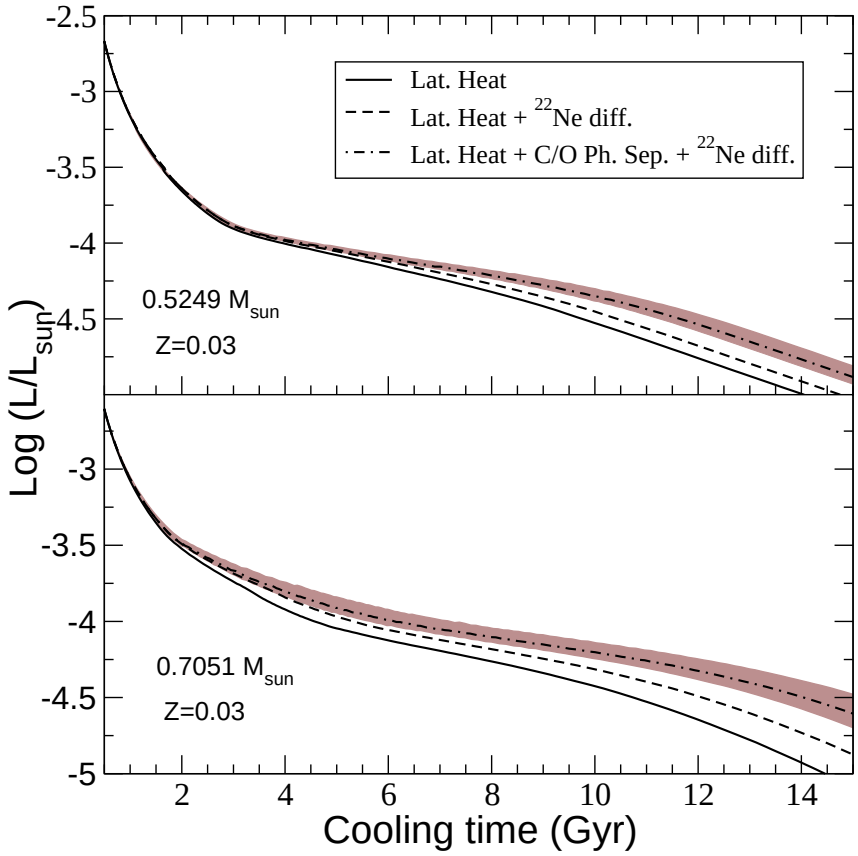

Figure 4.3: Surface luminosity versus age for the 0.5249 and 0.7051 $M_{\odot}$ sequences (upper and bottom panel, respectively). The solid line displays the cooling times for the case in which only the release of latent heat is considered and carbon-oxygen phase separation and ^{22}Ne sedimentation are neglected. The dashed line displays the results for the case where both latent heat and ^{22}Ne sedimentation are included, but not carbon-oxygen phase separation. The dot-dashed line corresponds to the case where latent heat, carbon-oxygen phase separation and ^{22}Ne sedimentation are considered. For this case, the gray region shows the extent to which the cooling times change when the diffusion coefficient of ^{22}Ne is changed by a factor of 2. The metal content in all cases is $Z = 0.03$.

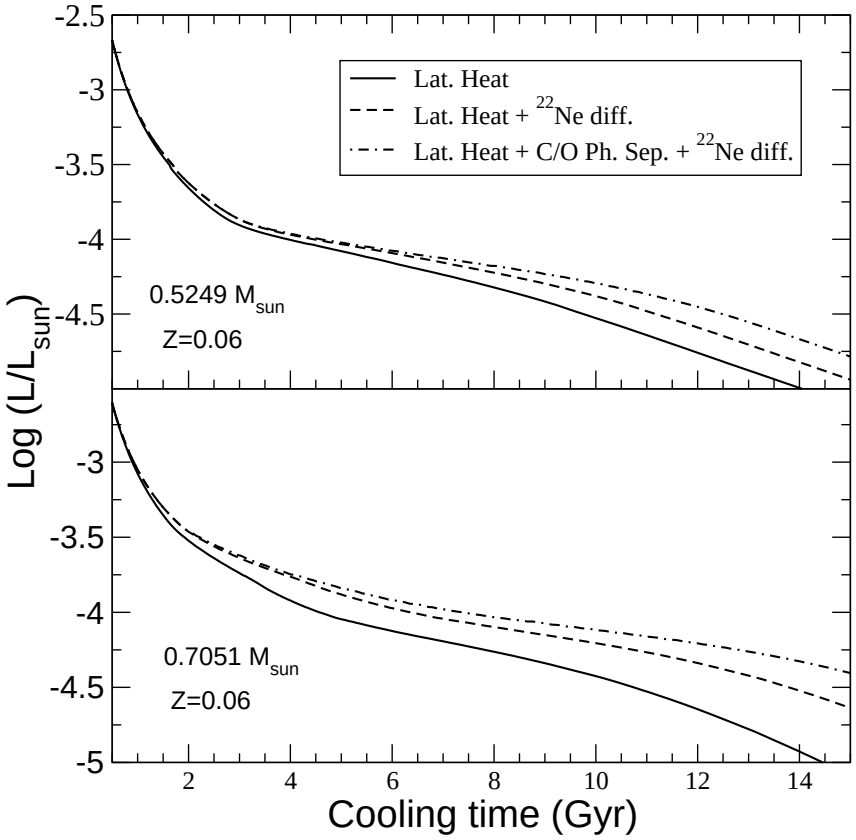

Figure 4.4: Similar to Fig. 4.3 but for white dwarf models with a metal content of $Z = 0.06$ in their cores.

in more massive white dwarfs. This can be better appreciated in Fig. 4.5, where we show the cooling curves for the 0.5249, 0.7051, and 0.8779 $M_{\odot}$ sequences for the case $Z = 0.03$. In both panels, we display with thick lines the cooling curves that result from considering the energy released by crystallization (latent heat), carbon-oxygen phase separation and ^{22}Ne sedimentation. The thin lines show the corresponding cooling curves when ^{22}Ne sedimentation is neglected, but latent heat (upper panel), and latent heat and carbon-oxygen phase separation (bottom panel) are taken into account. Note the marked lengthening of the cooling times that results from the ocurrence of ^{22}Ne sedimentation at luminosities as high as $\log(L/L_{\odot}) \approx -3.5$ (see bottom panel) for the massive sequence of 0.8779 $M_{\odot}$. This delay persists until low luminosities. For the lowest stellar masses considered in this work (0.5249 $M_{\odot}$), appreciable delays in the cooling rates due to ^{22}Ne sedimentation take place, but only at luminosities lower than $\log(L/L_{\odot}) \approx -4.2$. Carbon-oxygen phase separation also leads to appreciable delays in the cooling rates. The extent of this delay and

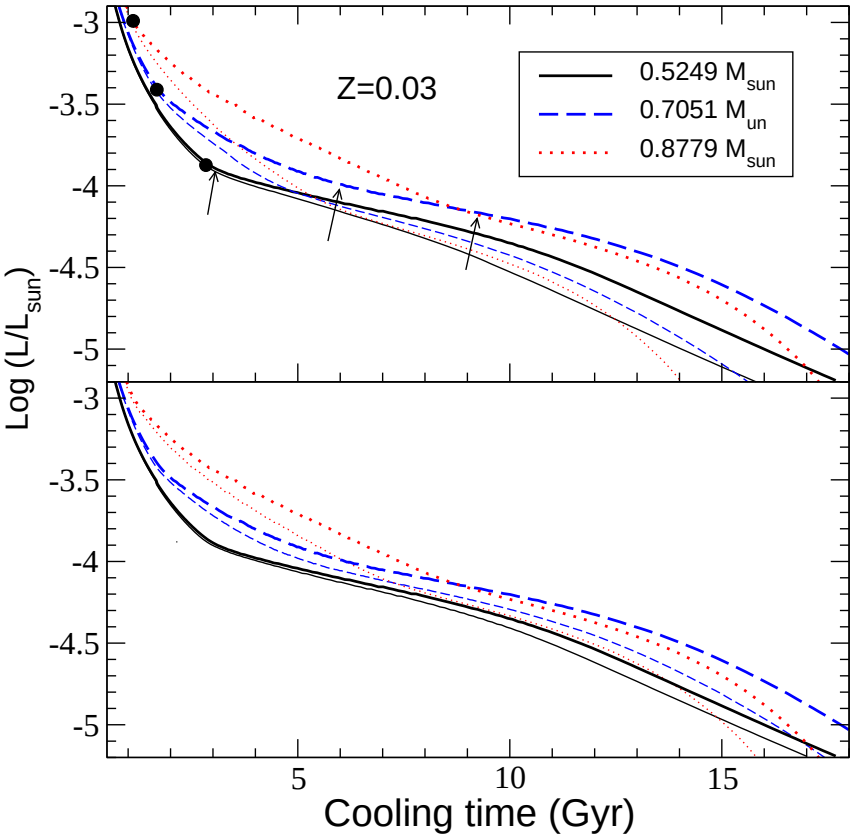

Figure 4.5: Surface luminosity versus cooling time for the 0.5249, 0.7051, and 0.8779 $M_{\odot}$ sequences. In both panels, the thick lines correspond to sequences where the release of latent heat, carbon-oxygen phase separation and ^{22}Ne sedimentation are considered. Sequences with thin lines consider either only latent heat (upper panel) or latent heat plus carbon-oxygen separation (botton panel), but not ^{22}Ne sedimentation. Filled circles and arrows at selected sequences denote, respectively, the onset of crystallization and the time at which convective coupling occurs. The metallicity is $Z = 0.03$.

the luminosities at which this occurs depend on the stellar mass. In the case of more massive white dwarfs, most of the carbon-oxygen phase separation and ^{22}Ne sedimentation occur during evolutionary stages prior to the convective coupling — the onset of which is indicated by arrows on the sequences with thick lines in the upper panel. Convective coupling takes places when the envelope convective region penetrates into the degenerate core, with the consequent release of excess thermal energy, and the resulting slow-down of the cooling process, as reflected by the change of slope in the cooling curve — see Fontaine et al. (2001). By contrast, in the less massive models, the delay in the cooling rate due to convective coupling takes place

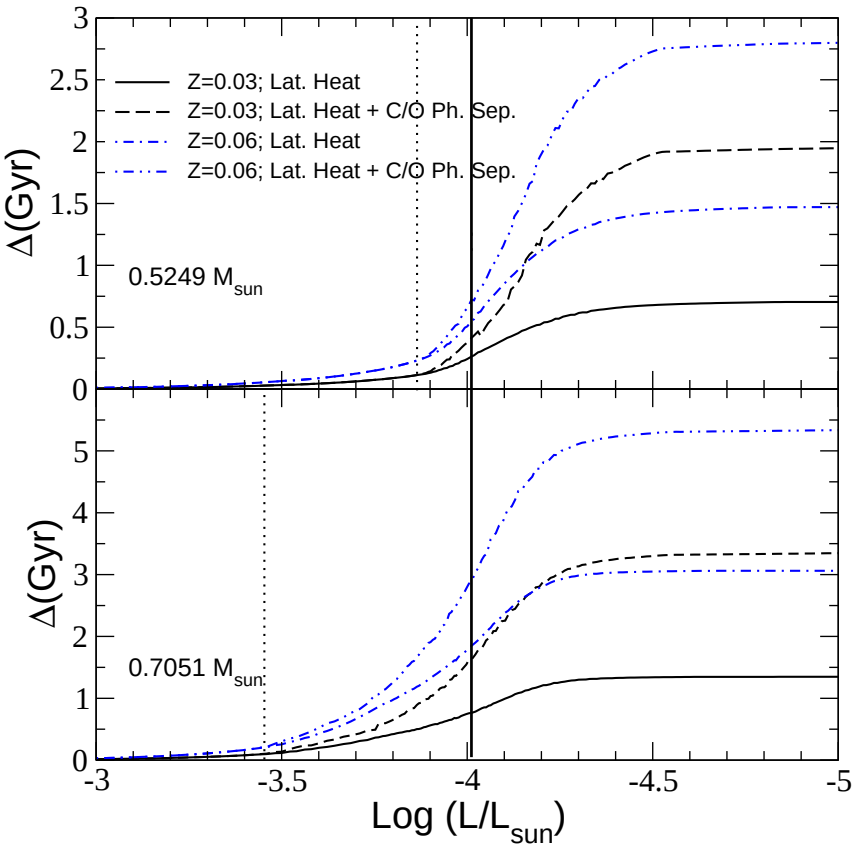

Figure 4.6: Difference in evolutionary times (Gyr) between various sequences that include ^{22}Ne diffusion and the sequence which considers only latent heat, for white dwarfs with masses 0.5249 and 0.7051 $M_{\odot}$. The vertical dotted lines mark the surface luminosity at the onset of core crystallization, and the vertical solid line the location of the faint peak in the NGC 6791 luminosity function.

before the release of appreciable energy from carbon-oxygen phase separation and ^{22}Ne sedimentation. This in part helps to understand the distinct behavior of the cooling curves with stellar mass.

From the preceeding paragraphs, we conclude that, in the case of white dwarfs that result from progenitor stars with super-solar metallicity, the occurrence of ^{22}Ne sedimentation releases enough energy to produce appreciable delays in the rate of cooling at relevant stellar luminosities. We can obtain a more quantitative idea of this assertion examining Fig. 4.6 — see also Table 4.2 — which shows the age difference between sequences that incorporte the energy released from ^{22}Ne sedimentation and the sequence that considers only latent heat, for two masses and the two metallicities adopted in this study. It is clear that both carbon-oxygen phase separation and

Table 4.2: Differences in the evolutionary times (Gyr) between sequences which include the release of latent heat, carbon-oxygen phase separation and ^{22}Ne sedimentation with the sequence which considers only the release of latent heat. The results are shown at selected stellar lumonisities and masses (in solar units), for both $Z = 0.03$ and $Z = 0.06$.

	$Z = 0.03$							$Z = 0.06$						
$\log(L/L_\odot)$	0.5249	0.5932	0.6598	0.7051	0.7670	0.8779	1.0000	0.5249	0.5932	0.6598	0.7051	0.7670	0.8779	1.0000
-3.0	< 0.01	0.01	0.01	0.02	0.03	0.07	0.35	0.01	0.02	0.03	0.03	0.05	0.14	0.67
-3.5	0.03	0.05	0.10	0.14	0.33	1.02	1.45	0.07	0.09	0.20	0.30	0.64	1.80	2.61
-4.0	0.38	0.64	1.03	1.63	2.04	2.51	2.30	0.66	1.18	1.89	2.88	3.58	4.26	3.79
-4.5	1.90	2.44	2.84	3.31	3.33	3.20	2.60	2.73	3.69	4.43	5.29	5.33	5.05	4.10

^{22}Ne sedimentation lead to substantial delays in the cooling times. Note that, at very low surface luminosities and for metallicity $Z = 0.03$, the inclusion of both carbon-oxygen phase separation and ^{22}Ne sedimentation produces age differences between $\sim$ 2.0 and 3.3 Gry, depending on the value of the stellar mass. These differences range from 2.7 to 5.3 Gyr for the case of progenitor stars with $Z = 0.06$. Note also that the magnitude of the delay resulting from the ^{22}Ne sedimentation is comparable or even larger than that induced by carbon-oxygen phase separation. In particular, by $\log(L/L_{\odot}) \approx -4.0$, the luminosity at which the faint peak of the white dwarf luminosity function in NGC 6791 is located, the release of energy from ^{22}Ne sedimentation markedly slows down the cooling rate of the more massive white dwarfs, which, because of their short pre-white dwarf times, populate the faint end of the white dwarf luminosity function of the cluster. For our more massive sequences and at the metallicity of the cluster ($Z \simeq 0.04$), we find that the delays from ^{22}Ne sedimentation alone range from 1.10 to 1.50 Gyr and $\approx$ 1.80 Gyr at $\log(L/L_{\odot}) \approx -4.0$ and -4.2, respectively. These delays together with the delays resulting from carbon-oxygen phase separation, are of the order of what is required to solve the age discrepancy in NGC 6791 (García-Berro et al., 2010). The delay in the cooling rate of white dwarfs resulting from ^{22}Ne sedimentation is important and points out the necessity of incorporating this energy source in the calculation of detailed white dwarf cooling sequences, particularly in the case of white dwarfs populating metal-rich clusters.

Because of the relevance of the ^{22}Ne sedimentation for the cooling of white dwarfs, we find instructive to estimate the lowest metallicity for which ^{22}Ne sedimentation starts to affect significantly the cooling times of white dwarfs. To this end, we compute additional cooling sequences for initial ^{22}Ne abundances of 0.01 and 0.005. For the case of an initial ^{22}Ne abundance of 0.01, ^{22}Ne sedimentation increases the cooling time of our 0.5249 $M_{\odot}$ sequence that considers latent heat and carbon-oxygen phase separation by at most 1–2%. The magnitude of the delays are larger for more massive white dwarfs, reaching 3–6% and 4–8% for the 0.7051 and 1.0 $M_{\odot}$ sequences, respectively. For these two stellar masses, the resulting delays are 1.5–3% and 2–4% for a ^{22}Ne abundances of 0.005. We conclude that, for initial ^{22}Ne abundances smaller than $\approx$ 0.01, ^{22}Ne sedimentation has a minor impact on white dwarf cooling times, except for rather massive white dwarfs for which non-negligible delays (but smaller than 8%) are found even for ^{22}Ne abundances of 0.005.

Finally, to account for possible uncertainties in the actual value of the diffusion coefficient of ^{22}Ne (Deloye & Bildsten, 2002), we compute additional cooling sequences for which we multiply and divide the diffusion coefficient by a factor of 2. The resulting impacts on the cooling time for the case in which $Z = 0.03$ can be seen in Fig. 4.3 for the 0.7051 and the 0.5249 $M_{\odot}$ sequences that consider latent heat, carbon-oxygen phase separation and ^{22}Ne sedimentation. The gray region shows the extent to which the cooling curves vary when the diffusion coefficient is changed within this range of values. For the more massive sequence and at $\log(L/L_{\odot}) = -4.5$

and −4, the cooling times change by less than 8% and −5%, and by 17% and −8%, respectively. For the less massive sequence, the changes remain below 7%. In the case of the $1.0\,M_{\odot}$ sequence, an increase in $D_{\rm s}$ by a factor of 2 causes a maximum age difference of $\approx 20\%$ in the luminosity range from $\log(L/L_{\odot}) \approx -3$ to −3.5. It is clear that uncertainties in the diffusion coefficient larger than a factor of 2 will affect the cooling time considerably, particularly for our most massive white dwarf sequences.

4.4 Summary and conclusions

The use of white dwarfs as reliable cosmic clocks to date Galactic stellar populations has been recently thrown into doubt by a new observational determination of the white dwarf luminosity function in the old, metal-rich open cluster NGC 6791 (Bedin et al., 2008a), the age of which as derived from the main sequence turn-off technique (8 Gyr) markedly disagrees with the age derived from the termination of the white dwarf cooling sequence (6 Gyr). This discrepancy points out at a missing physical process in the standard treatment of white dwarf evolution. In view of the high metallicity characterizing NGC 6791 ($Z \approx 0.04$), the gravitational settling of ^{22}Ne constitutes the most viable process that can decrease the cooling rate of cool white dwarfs. Indeed, as first shown by Isern et al. (1991) and later by Deloye & Bildsten (2002) and García-Berro et al. (2008), the slow gravitational settling of ^{22}Ne in the liquid phase releases enough energy as to appreciably slow down the cooling rate of white dwarfs in metal-rich clusters like NGC 6791.

Motivated by these considerations, we have presented a grid of white dwarf evolutionary sequences that incorporates for the first time the energy contributions arising from both ^{22}Ne sedimentation and carbon-oxygen phase separation. The grid covers the entire mass range expected for carbon-oxygen white dwarfs, from 0.52 to $1.0\,M_{\odot}$, and it is based on a detailed and self-consistent treatment of these energy sources. Except for the $1.0\,M_{\odot}$ sequence, the history of progenitor stars has been taken into account by evolving initial stellar configurations in the mass range 1 to $5\,M_{\odot}$ from the ZAMS all the way through the thermally pulsing AGB and mass loss phases. Because of the full calculation of the evolution of progenitor stars, the white dwarf sequences incorporates realistic and consistent carbon-oxygen profiles — of relevance for an accurate computation of the energy released by carbon-oxygen phase separation. In addition, detailed non-gray model atmospheres are used to derive the outer boundary condition for the evolving sequences. At the low luminosities where the process of ^{22}Ne sedimentation becomes relevant, the outer boundary conditions influence the cooling times.

We find that ^{22}Ne sedimentation has notable consequences for the cooling times of cool white dwarfs characterized by a high metal content in their interiors. The related energy release strongly delays their cooling. The precise value of the delays

depends on the mass of the white dwarf, its luminosity and on the metal content. For instance, because of their larger gravities, the impact of ^{22}Ne sedimentation starts earlier in more massive white dwarfs. In particular, appreciable delays in the cooling rates start to manifest themselves at luminosities of $\log(L/L_{\odot}) \approx -3.5$ to -4.2. In general, the magnitude of the delays in the cooling rates resulting from ^{22}Ne sedimentation is comparable (or even larger in the case of $Z = 0.06$) to the delays induced by carbon-oxygen phase separation. At the approximate location of the faint peak in the white dwarf luminosity function of NGC 6791, delays between 1 and 1.5 Gyr are expected as a result of ^{22}Ne sedimentation only. As recently shown in García-Berro et al. (2010), the occurrence of this process in the interior of cool white dwarfs is a key factor in solving the longstanding age discrepancy of NGC 6791.

In summary, we find that the evolution of cool white dwarfs stemming from progenitor stars with super-solar metallicity, is strongly modified by the energy released from ^{22}Ne sedimentation. The resulting delays in cooling times of such white dwarfs are important and have to be taken into account in age determinations of metal-rich clusters from the cooling sequence of their white dwarfs. The grid of evolutionary sequences we have presented here is the first one intented for such a purpose, and incorporates the effects carbon-oxygen phase separation and ^{22}Ne sedimentation in the evolution of these stars.

Chapter 5

Solving the age discrepancy for NGC 6791

In this chapter we compute the age of NGC 6791 using the latest generation models of cooling white dwarfs (see chapter 4 for more details). NGC 6791 is a well studied open cluster (Bedin et al., 2005) that it is so close to us that can be imaged down to very faint luminosities (Bedin et al., 2008a). The main sequence turn-off age ($\sim$ 8 Gyr) and the age derived from the termination of the white dwarf cooling sequence ($\sim$ 6 Gyr) are significantly different. One possible explanation is that as white dwarfs cool, one of the ashes of helium burning, ^{22}Ne, sinks in the deep interior of these stars (Bravo et al., 1992; Bildsten & Hall, 2001; Deloye & Bildsten, 2002). At lower temperatures, white dwarfs are expected to crystallize and phase separation of the main constituents of the core of a typical white dwarf, ^{12}C and ^{16}O, is expected to occur (Garcia-Berro et al., 1988b,a). This sequence of events is expected to introduce significant delays in the cooling times (Segretain et al., 1994; García-Berro et al., 2008), but has not hitherto been proven. Here we show that, as theoretically anticipated (Deloye & Bildsten, 2002; Garcia-Berro et al., 1988b), physical separation processes occur in the cores of white dwarfs, solving the age discrepancy for NGC 6791.

5.1 Introduction

The use of white dwarfs as cosmochronometers relies on the accuracy of the theoretical cooling sequences. The standard theory of dense plasmas indicates that as white dwarfs cool, one of the ashes of helium burning, ^{22}Ne, sinks in the deep interior of these stars, due to its large neutron excess and to the strong gravity that characterize white dwarfs (Bravo et al., 1992; Bildsten & Hall, 2001). At even lower temperatures white dwarfs are expected to crystallize and phase separation of the main constituents of the core of a typical white dwarf, ^{12}C and ^{16}O, is expected to

occur (Garcia-Berro et al., 1988b; Segretain et al., 1994). However, up to now there was no observational evidence of this sequence of events.

NGC 6791 is a metal-rich ([Fe/H]$\sim$ +0.4), well populated ($\sim$ 3000 stars) and very old Galactic open cluster (Bedin et al., 2005). Additionally, it is so close to us that has been imaged down to luminosities below those of the faintest white dwarfs (Bedin et al., 2005, 2008a). These characteristics make of this cluster a primary target to detect the cooling sequence of white dwarfs and, hence, it has been the subject of different observational studies, since it provides an unique test-bed to prove the accuracy of the evolutionary sequences of both non-evolved stars and white dwarfs (Bedin et al., 2008b). The main result that emerges from these studies is that there is a serious discrepancy between the age of the cluster derived from the main sequence turn-off technique and the age derived from the termination of the white dwarf cooling sequence, thus casting doubts on the use of white dwarfs as reliable chronometers. Several explanations for solving this discrepancy have been proposed. Of these, the most viable and promising explanation is, precisely, the delays introduced by physical separation processes (García-Berro et al., 2008). However, up to now no white dwarf cooling sequences incorporating these effects have been available, thus hampering a confirmation of this. Here we solve this age discrepancy by using a set of new cooling sequences which incorporate the effects of both ^{22}Ne diffusion and carbon-oxygen phase separation.

The chapter is organized as follows. Sect. 5.2 summarizes the main ingredients of our Monte Carlo code used to simulate the white dwarf luminosity function. Moreover, in this chapter information is given on our cooling sequences which, as mentioned, include the release of gravitational energy resulting from ^{22}Ne diffusion in the liquid phase and from phase separation of carbon and oxygen upon crystallization. Sect. 5.3 presents the main results of our simulations aimed to solving the age discrepancy for NGC 6791. Finally, Sect. 5.4 closes the chapter with a summary and our conclusions.

5.2 Modeling NGC 6791

5.2.1 The Monte-Carlo simulator

The white dwarf luminosity function of NGC 6791 was simulated using a Monte-Carlo technique. Our Monte Carlo simulator has been previously employed to model the Galactic disk and halo field white dwarf populations (García-Berro et al., 1999; Torres et al., 2002; García-Berro et al., 2004), with excellent results. We briefly describe here the most important ingredients of our simulator. Synthetic main sequence stars were randomly drawn according to a Salpeter-like initial mass function, and a burst of star formation starting 8 Gyr ago, which lasted for 1 Gyr. We accounted for unresolved detached binary white dwarfs adopting a fraction of 54% of binary systems in the main sequence, which leads to a fraction of white dwarfs in binaries

of 36%. We also employed main sequence lifetimes appropriate for the metallicity of NGC 6791 (Weiss & Ferguson, 2009) and we used an up-to-date initial-to-final mass of white dwarfs (Catalán et al., 2008a). Given the age of the cluster, the time at which each synthetic star was born and its associated main sequence lifetime, we determined which stars were able to evolve to white dwarfs and we interpolated their colors and luminosities using the theoretical cooling sequences described in Sect. 5.2.2. For unresolved binary systems we did the same calculation for the secondary and we added the fluxes. The photometric errors were drawn according to Gaussian distributions. The standard photometric error was assumed to increase linearly with the magnitude (Bedin et al., 2005, 2008a). Finally, we added the distance modulus of NGC 6791, $(m-M)_{\rm F606W} = 13.44$, and its color excess, $E({\rm F606W}-{\rm F814W}) = 0.14$ to obtain a synthetic white dwarf color-magnitude diagram. Fig. 5.1 shows all these steps. The upper left panel shows the cooling isochrone of single white dwarfs for the age of the cluster. When the age dispersion is added (upper right panel) some spread at very low luminosities is clearly visible. The bottom left panel show the effect of introducing the photometric errors. Finally, the bottom right panel displays the result of including unresolved binary systems. It is striking the high degree of similarity of the Monte Carlo realization of the color-magnitude diagram with the observational data, which is shown in the right panel of Fig. 5.2, respectively. Two clumps of stars are clearly visible in these diagrams. The bright one corresponds to unresolved binary stars, while the faint one corresponds to the pile-up of single white dwarfs owing to the combined effects of ^{22}Ne sedimentation and carbon-oxygen phase separation.

5.2.2 The cooling sequences

The cooling sequences adopted in this chapter were extensively discussed in Chap. 4 — see also Althaus et al. (2010c). In summary, these sequences were obtained from star models with stellar masses at the ZAMS ranging from 1 to 3 $M_{\odot}$ and were followed through the thermally pulsing and mass-loss phases on the AGB to the white dwarf stage. The resulting white dwarf masses were 0.5249, 0.5701, 0.593, 0.6096, 0.6323, 0.6598 and 0.7051$M_{\odot}$. These calculations have been done with `LPCODE`, a state-of-the-art stellar evolutionary code (Althaus et al., 2009c) — see also App. A.1. We have fully included the release of gravitational energy resulting from ^{22}Ne diffusion in the liquid phase and from phase separation of carbon and oxygen upon crystallization (Isern et al., 1997, 2000). We stress here that this was made in a self-consistent way, because the energy release is locally coupled to the equations of stellar evolution. Specifically, we have computed the structure and evolution of white dwarfs using a luminosity equation appropriately modified to account for the local contribution of energy released by the changes in the chemical profiles arising from physical separation processes. The energy contribution of ^{22}Ne sedimentation was computed assuming that the liquid behaves as a single background one-component

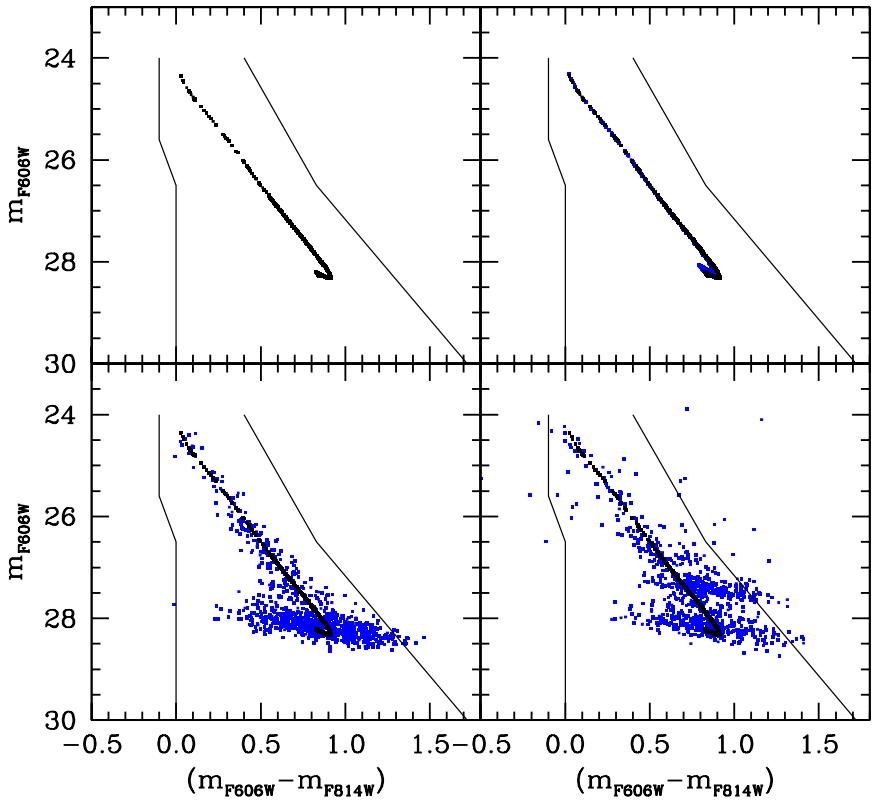

Figure 5.1: A summary of the different steps in a typical Monte Carlo simulation of the color-magnitude diagram of NGC 6791. See main text for details.

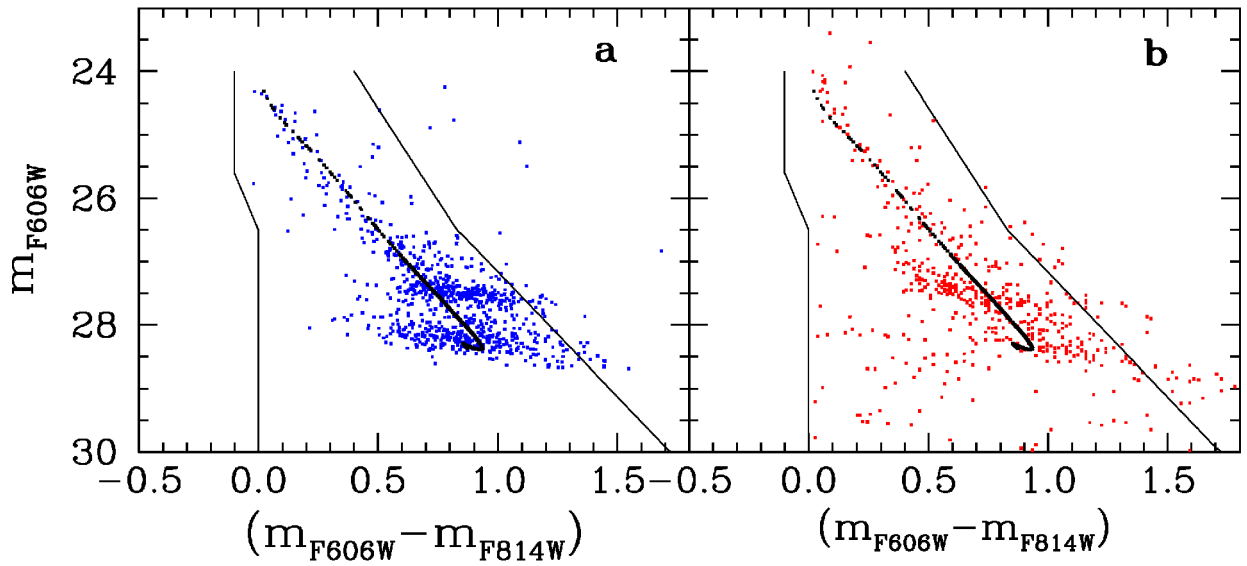

Figure 5.2: Color-magnitude diagrams of the white dwarfs in NGC 6791. The left panel shows a typical Monte Carlo realization of the colour-magnitude diagram of NGC 6791. The blue dots are synthetic white dwarfs obtained using the procedure outlined in the main text and, thus, incorporating the photometric errors. A total of $\approx$ 850 white dwarfs with magnitude smaller than $m_{\rm F606W} = 28.55^{\rm mag}$ have been generated, the same number of white dwarfs observationally found (Bedin et al., 2005, 2008a,b). The black dots show a theoretical white dwarf isochrone for 8 Gyr. Note the blue hook caused by the most massive white dwarfs of the cluster. The black lines are the observational selection area (Bedin et al., 2008b), white dwarfs outside this area are not considered. The right panel shows the observational white dwarf colour-magnitude diagram.

plasma consisting of the average by number of the real carbon and oxygen one (Segretain & Chabrier, 1993), plus traces of neon. The diffusion coefficient adopted here is the theoretical one (Deloye & Bildsten, 2002). The energy contribution arising from the core chemical redistribution upon crystallization has also been computed self-consistently with the oxygen enrichment of the core and the white dwarf evolution, keeping constant the abundance of neon. The adopted carbon-oxygen phase diagram is of the spindle form (Segretain & Chabrier, 1993). Finally, our calculations rely on realistic boundary conditions for evolving cool white dwarfs, as given by non-grey model atmospheres (Rohrmann et al., 2011).

5.3 Results

5.3.1 The luminosity function of NGC 6791

Fig. 5.3 shows both the observed and the theoretical white dwarf luminosity functions. The solid line shows the average of 10^4 Monte Carlo realizations corresponding to the age (8 Gyr), metallicity ([Fe/H]$\sim +0.4$) and distance modulus (13.44) of the cluster. Note the existence of two peaks in the white dwarf luminosity function, which are the direct consequence of the two previously discussed clumps in the colour-magnitude diagram. Moreover, the main sequence turn-off and white dwarf ages are exactly the same, solving the age discrepancy of NGC 6791. Additionally, a χ^2 analysis of the luminosity function reveals that, due to the narrowness of its two peaks, the cooling age determined in this way is very precise, being the age uncertainty $\sigma_{\rm WD} = \pm 0.1$ Gyr, significantly smaller than the uncertainty in the age derived from main sequence stars, $\sigma_{\rm MS} \pm 0.2$ Gyr. The reason for this small age uncertainty is that the white dwarf luminosity function presents two narrow peaks. To illustrate the importance of physical separation processes in Fig. 5.3 we also show, as a dotted line, the luminosity function obtained assuming that no physical separation processes occur and adopting the main-sequence turn-off age (8 Gyr). Clearly, the resulting luminosity function does not agree with the observational data. It could be argued that in this case the theoretical luminosity function could be reconciled with the observational data by simply decreasing the distance modulus by about 0.5 magnitudes. However, the same distance modulus should be then adopted to fit the main-sequence turn-off. If this were the case, we estimate that the main-sequence turn-off age would be ~ 12 Gyr, worsening the age discrepancy. Additionally, a distance modulus of 13.46 ± 0.1 has been recently derived for NGC 6791 using eclipsing binaries (Grundahl et al., 2008), a totally independent and reliable method that does not make use of theoretical models. Thus, a large error in the distance modulus is quite implausible. Hence, the only possibility left to minimize the age discrepancy is to consider larger values of the metallicity, since isochrones with an enhanced metallicity have a fainter main sequence turn-off and, consequently, would result in a lower cluster turn-off age. However, to solve the age

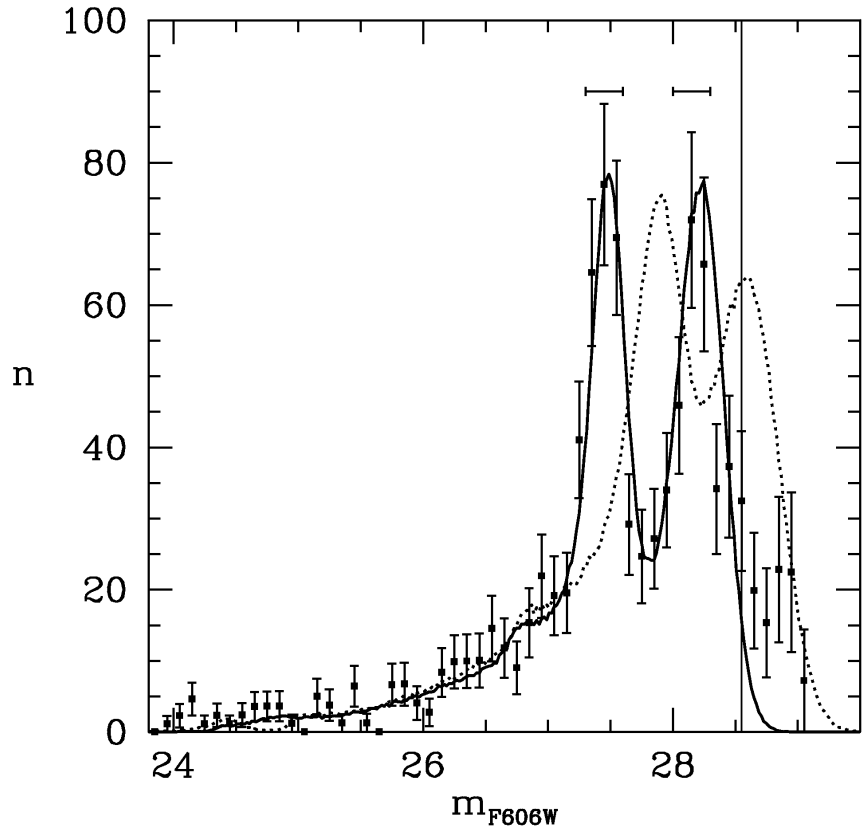

Figure 5.3: White dwarf luminosity function of NGC 6791. The observational white dwarf luminosity function is shown as filled squares. The 1σ error bars correspond to the standard deviation (Bedin et al., 2008a). The solid line is the average of 10^4 Monte Carlo realizations corresponding to the age (8 Gyr), metallicity (0.04) and distance modulus (13.44) of NGC 6791. To illustrate the importance of physical separation processes, we also show the white dwarf luminosity function for the same age and assuming that no ^{22}Ne sedimentation and no phase separation upon crystallisation occur (dotted line). The theoretical luminosity function is shifted to lower luminosities (larger magnitudes) to an extent that is incompatible with the observational data. The distance modulus required to fit the observations would be 13.0, a value considerably smaller than those observationally reported (Bedin et al., 2005, 2008a; Grundahl et al., 2008). This distance modulus would imply a main-sequence turn-off age of 12 Gyr, worsening the age discrepancy (Bedin et al., 2005). Also shown at the top of the figure are the photometric error bars. Changes in the exponent of the initial mass function (of ± 0.1) translate into small changes in the positions of the peaks (≤ 0.02 mag), well below the photometric errors (0.15 mag). As for the relationship between the mass of white dwarfs and the mass of their progenitors, the differences are also small (≤ 0.04 mag) when other recent relationships are adopted (Catalán et al., 2008a). The same holds for reasonable choices of main-sequence lifetimes (Pietrinferni et al., 2004), in which case the differences are smaller than 0.02 mag, or the duration of the burst of star formation (≤ 0.04 mag when the duration of the burst is decreased to 0.1 Gyr).

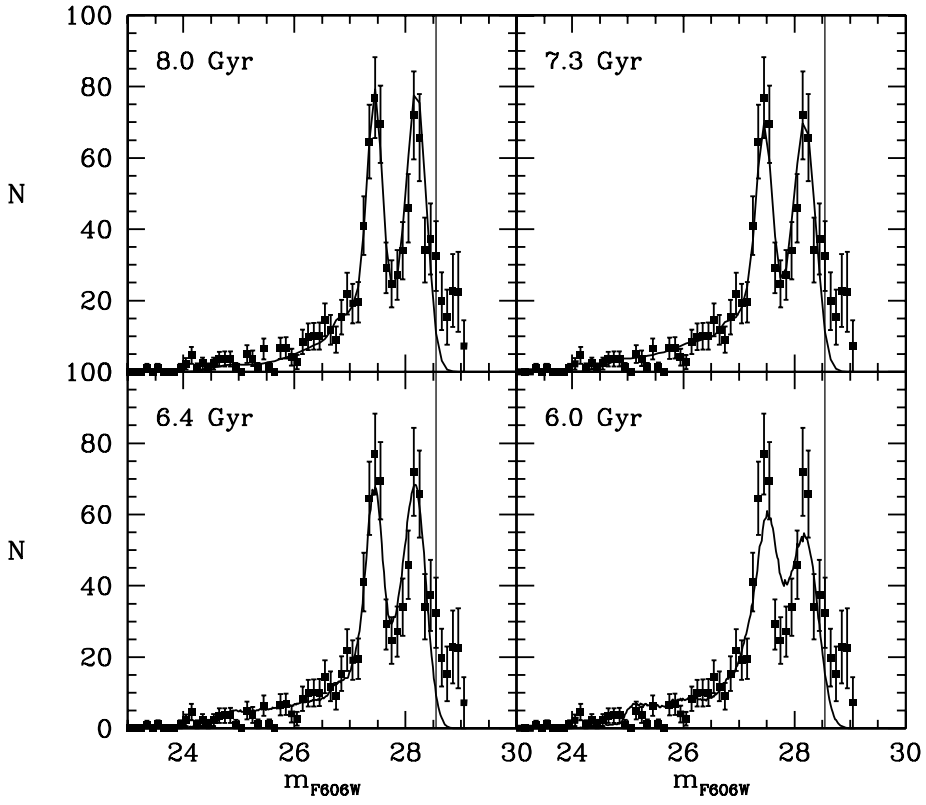

Figure 5.4: The theoretical white dwarf luminosity functions assuming that both ^{22}Ne diffusion and carbon-oxygen phase separation occur (upper left panel), when only ^{22}Ne sedimentation is taken into account (upper right panel), when only carbon-oxygen phase separation is assumed to occur (bottom left panel), and when no physical separation processes occur. The observational data, with the corresponding error bars, are also shown. The thin vertical line shows the magnitude limit above which the observations are severely incomplete

discrepancy a metallicity [Fe/H]$\sim +0.7$ would be needed. This metallicity is $\sim 3\sigma$ from the most recent spectroscopic value (Gratton et al., 2006). Additionally, at this exceptionally high metallicity the predicted shape and star counts along the turn-off and sub-giant branch would be at odds with observations.

In Fig. 5.4 we show the white dwarf luminosity function of NGC 6791 for different cooling sequences, which take into account or disregard the two physical separation processes, as well as the observed white dwarf luminosity function. This figure clearly illustrates the leading role of chemical fractionation processes, since the luminosity functions which do not take into account these processes do not match the observations, and moreover the white dwarf cooling ages (shown in the upper left corner of each of these panels) significantly differ from the main sequence turn-off age of the cluster. Based exclusively on the location of the cool end of the white dwarf sequence and not on the shape of the luminosity function we find that when both carbon-oxygen phase separation and ^{22}Ne gravitational sedimentation are not taken into account, the age of the cluster turns out to be 6.0 ± 0.2 Gyr. Thus, this type of cooling sequences, which are the most commonly used ones, can be safely discarded at the $\sim 5\sigma$ confidence level, where $\sigma \sim 0.4$ Gyr is the uncertainty in the main sequence turn-off age. If only carbon-oxygen phase separation is considered the computed age of the cluster is 6.4 ± 0.2 Gyr, so these sequences can also be excluded at the $\sim 4\sigma$ confidence level, whereas if only ^{22}Ne sedimentation is taken into account we derive an age of 7.0 ± 0.3 Gyr, which falls $\sim 2.5\sigma$ off the main sequence turn-off age.

To sum up, we find that the cooling sequences computed without taking into account carbon-oxygen phase separation and ^{22}Ne gravitational sedimentation can be safely discarded at the $\sim 10\sigma_{\rm WD}$ or at the $\sim 5\sigma_{\rm MS}$ confidence level. The cooling sequences in which only carbon-oxygen phase separation is considered can also be excluded at the $\sim 8\sigma_{\rm WD}$ ($\sim 4\sigma_{\rm MS}$) confidence level, whereas the cooling sequences in which only ^{22}Ne sedimentation is taken into account fall $\sim 5\sigma_{\rm WD}$ ($\sim 2.5\sigma_{\rm MS}$) off the main sequence turn-off age.

5.4 Summary and conclusions

We have computed white dwarf cooling sequences appropriate for the metallicity of the Galactic open cluster NGC 6791. These cooling sequences include self-consistently the effects of both ^{22}Ne diffusion in the liquid phase and carbon-oxygen phase separation upon crystallization (see Chap. 4 for more details). We have shown that the only way to reconcile the ages derived from the position of the main sequence turn-off and from the position of the cut-off of the white dwarf luminosity function is to include both physical processes. Consequently, our results confirm unambiguously the occurrence of ^{22}Ne sedimentation and of carbon-oxygen phase separation in the deep interiors of white dwarfs. These findings have important consequences,

as they prove the correctness of our understanding of the theory of dense plasmas and confirm that white dwarfs can be used as independent reliable chronometers.

Chapter 6

Constraining important characteristics of NGC 6791

In this chapter we obtain useful information about the open cluster NGC 6791. This was started in chapter 5, but here we extend the study. Specifically, use observations of the white dwarf cooling sequence to constrain important properties of the NGC 6791 cluster stellar population, such as the existence of a putative population of massive helium-core white dwarfs, and the properties of a large population of unresolved binary white dwarfs. We also investigate the use of white dwarfs to disclose the presence of cluster subpopulations with a different initial chemical composition, and we obtain an upper bound to the fraction of hydrogen-deficient white dwarfs.

6.1 Introduction

The use of white dwarfs as cosmochronometers relies on the accuracy of the theoretical cooling sequences. In chapter 5, as well as in García-Berro et al. (2010), we demonstrated that the slow down of the white dwarf cooling rate owing to the release of gravitational energy from ^{22}Ne sedimentation (Bravo et al., 1992; Bildsten & Hall, 2001; Deloye & Bildsten, 2002) and carbon-oxygen phase separation upon crystallization (Garcia-Berro et al., 1988b; Segretain et al., 1994) is of fundamental importance to reconcile the age discrepancy of the very old, metal-rich open cluster NGC 6791. This raises the possibility of using the white-dwarf luminosity function of this cluster to constrain its fundamental properties.

As already mentioned, NGC 6791 is one of the oldest Galactic open clusters — see, for instance, Bedin et al. (2005) and Kalirai et al. (2007), and references therein — and it is so close to us that it can be imaged down to very faint luminosities. A deep luminosity function of its well populated white dwarf sequence has been recently determined from HST observations (Bedin et al., 2008a) and displays a sharp cut-off at slow luminosities, caused by the finite age of the cluster, plus a secondary

peak at larger luminosities, most likely produced by a population of unresolved binary white dwarfs (Bedin et al., 2008b). These characteristics make this cluster a primary target to use the white dwarf cooling sequence to constrain the presence of a population of massive helium-core white dwarfs, the properties of the binary white dwarf population, the hypothetical presence of cluster subpopulations of different metallicity, and the fraction of hydrogen-deficient (non-DA) white dwarfs. Here we address these issues by means of Monte Carlo based techniques aimed at producing synthetic color-magnitude diagrams and luminosity functions for NGC 6791 white dwarfs, which can be compared with the observational data.

Firstly, we investigate in detail the nature of the secondary peak of the white dwarf luminosity function. This peak has been atributted to a population of unresolved binary white dwarfs (Bedin et al., 2008b) or to the existence of a population of single helium-core white dwarfs (Hansen, 2005). This is a crucial question because if the first hypothesis is true, the amplitude of the secondary peak is such that leads to an unusual fraction of binary white dwarfs, thus challenging our understanding of the physical processes that rule the formation of binary white dwarfs, especially at high metallicities. Consequently, we also study other explanations for the existence of a secondary peak in the white dwarf luminosity function, like the existence of a population of single helium-core white dwarfs. This explanation was first put forward by Hansen (2005) and Kalirai et al. (2007) and later was challenged, among others, by van van Loon et al. (2008). However, as we will show below, this explanation results in a white dwarf luminosity function that is at odds with the observed one, and hence the most likely explanation for the secondary bright peak is the population of unresolved binaries. Indeed, there is a strong reason to suspect that the bright peak of the white dwarf luminosity function of NGC 6791 is caused by a population of unresolved binary white dwarfs, namely, that the two peaks of the white dwarf luminosity function are separated by $0.75^{\rm mag}$. This is just exactly what it should be expected if the bright peak is caused by equal mass binaries. Hence, if this explanation for the bright peak of the white dwarf luminosity function is true this, in turn, enables us to study the properties of the population of such binary white dwarfs. Specifically, we study how different distributions of secondary masses of the unresolved binary white dwarfs affect the color-magnitude diagram and the white dwarf luminosity function.

Additionally, we test whether the white dwarf luminosity function can provide an independent way to check for the existence of subpopulations within a stellar system. The presence of these subpopulations has been found in several Galactic globular clusters of which ω Cen is, perhaps, the most representative one (Calamida et al., 2009). The appearance of NGC 6791 color-magnitude diagram, and the lack of any significant chemical abundance spread (Carraro et al., 2006) points toward a very homogeneous stellar population. However, a recent paper by Twarog et al. (2011) raises the possibility that there could be a 1 Gyr age difference between inner and outer regions of the cluster. Nevertheless, within the field covered by the white

dwarf photometry used in our analysis the age difference should be negigible. This is different from the case of individual Galactic globular clusters that host at least two distinct populations with approximately the same age and different abundance patterns of the C-N-O-Na elements — see Milone et al. (2010) for a recent brief review. Taking advantage of the well-populated cooling sequence in the observed color-magnitude diagram, we test whether modeling the cluster white dwarf color-magnitude alone can exclude the presence of subpopulations generated by progenitors with a metallicity different from the one measured spectroscopically.

As a final study, we use the luminosity function of NGC 6791 (Bedin et al., 2008a), and the fact that white dwarfs with hydrogen-rich atmospheres (of the DA type) and non-DA white dwarfs cool at a different rate, to place constraints on the fraction of these objects. This is an important point because Kalirai et al. (2005) have found that in the young open star cluster NGC 2099 there is a dearth of non-DA white dwarfs. These authors attributed the lack of non-DA objects to the fact that possibly the hot, high-mass cluster white dwarfs — white dwarfs in this cluster are estimated to be more massive than field objects in the same temperature range — do not develop sufficiently extended helium convection zones to allow helium to be brought to the surface and turn a hydrogen-rich white dwarf into a helium-rich one. Studying the fraction of non-DA white dwarfs in a different open cluster could provide additional insight into this question. Moreover, Kalirai et al. (2007) analyzed a sample of ~ 15 white dwarfs in NGC 6791, and although the sample was far from being complete, all them were of the DA type.

The chapter is organized as follows. Sect. 6.2.1 summarizes the main ingredients of our Monte Carlo code plus the other basic assumptions and procedures necessary to evaluate the characteristics of the white dwarf population for the different simulations presented here. Specifically, we discuss the most important ingredients used to construct reliable color-magnitude diagrams and the corresponding white dwarf luminosity functions. Sect. 6.3 presents the main results of our simulations for all points already mentioned in this section. Finally, Sect. 6.4 closes the chapter with a summary of our conclusions.

6.2 Modeling NGC 6791

6.2.1 The Monte-Carlo simulator

The photometric properties of NGC 6791 was simulated using a Monte Carlo technique in a similar way as it was done in Chap 5.2.1. Synthetic main-sequence stars are randomly drawn according to a Salpeter-like initial mass function that in the mass range relevant to NGC 6791 white dwarf progenitors ($M > 1.0\,M_{\odot}$) is essentially identical to the "universal" initial mass function of Kroupa (2001), and a burst of star formation starting 8 Gyr ago (as computed in chapter 5), lasting 0.1 Gyr (the exact value is not critical for our analysis). If not otherwise stated,

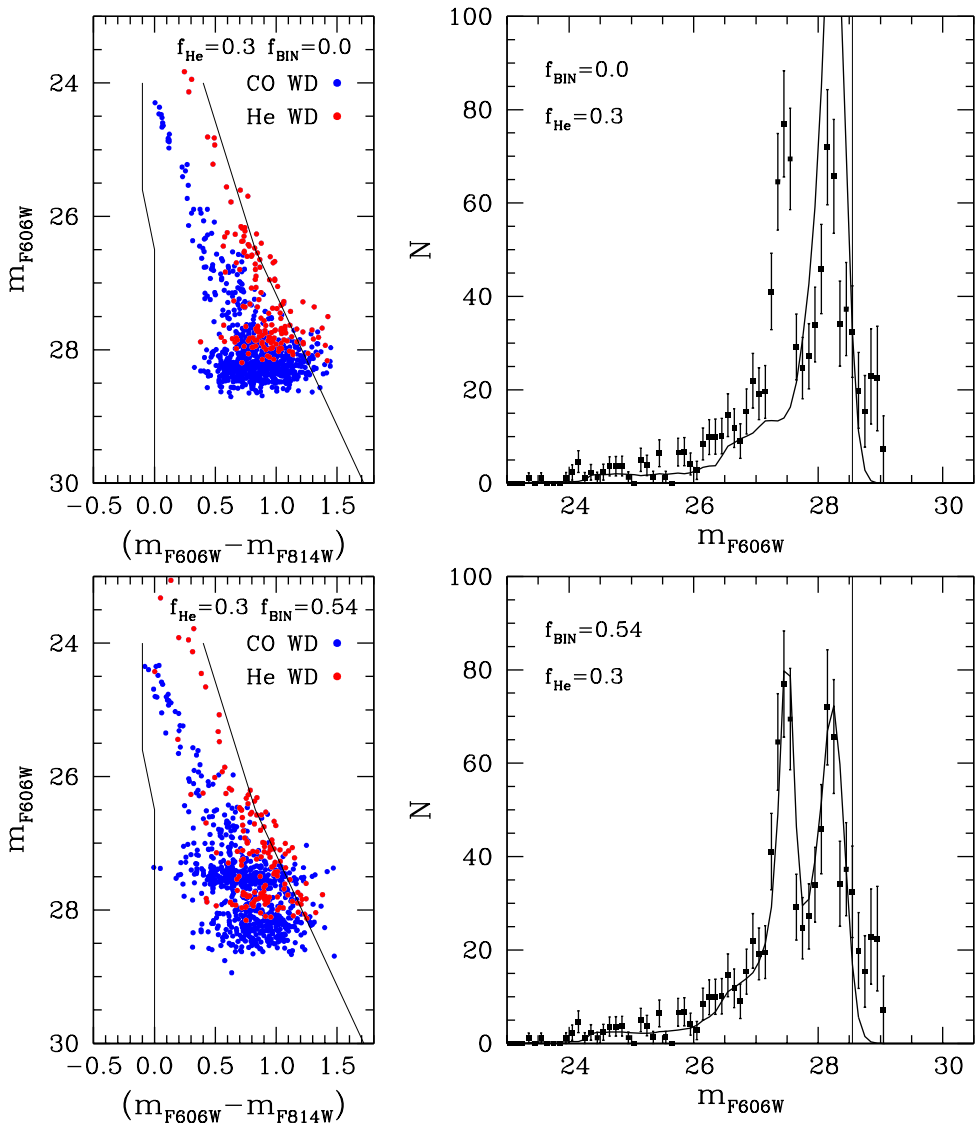

Figure 6.1: Color-magnitude diagrams (left panels) of the synthetic population of carbon-oxygen white dwarfs (blue symbols) and of helium-core white dwarfs (red symbols) and the corresponding white-dwarf luminosity functions (right panels). The observational selection area in the color-magnitude diagram of Bedin et al. (2005) is also shown using thin lines. These boundaries in the color-magnitude exclude low-mass helium-core white dwarfs. The observational white-dwarf luminosity function of Bedin et al. (2008b), which was corrected for incompleteness, is shown using black squares. Each theoretical luminosity function corresponds to an average of 10^4 Monte Carlo realizations. The vertical thin line marks the magnitude limit $\simeq 28.5^{\rm mag}$ above which the completeness level of the photometry falls below 50%. The top panels correspond to the case in which $f_{\rm He} = 0.3$ and $f_{\rm bin} = 0.0$ are adopted, while for the bottom ones we adopted $f_{\rm He} = 0.3$ and $f_{\rm bin} = 0.54$.

we account for a population of unresolved detached binary white dwarfs adopting a fraction $f_{\rm bin} = 0.54$ of binary systems in the main sequence, which leads to a fraction of unresolved white dwarf binaries of 36%. In our fiducial model we use the distribution of secondary masses previously employed by Bedin et al. (2008b), but other distributions were also used (see Sect. 6.3.2) to constrain the properties of the binary population. We employ main-sequence lifetimes from the calculations by Weiss & Ferguson (2009) for $Z = 0.04$, $Y = 0.325$ models, which correspond to [Fe/H]$\sim$0.4, a metallicity consistent with the recent spectroscopic determinations of Carraro et al. (2006), Gratton et al. (2006) and Origlia et al. (2006). For the white dwarf initial-final mass relationship we used that of Ferrario et al. (2005), which is appropriate for metal-rich stars, although our results are fairly insensitive to the precise choice of this function. For instance, when the up-to-date semiempirical initial-final mass function of Catalán et al. (2008a) is adopted, the results are almost indistinguishable from those obtained with the former relationship.

Given the cluster age, the time at which each synthetic star was born and its associated main sequence lifetime, we kept track of the stars able to evolve to the white dwarf stage, and we interpolated their colors and luminosities using the theoretical cooling sequences described in the following subsection. For unresolved binary systems we performed the same calculation for the secondary and we added the fluxes and computed the corresponding colors. The photometric errors were drawn according to Gaussian distributions, using the Box-Müller algorithm as described in Press et al. (1986). The standard photometric errors in magnitude and color were assumed to increase linearly with the magnitude following Bedin et al. (2005, 2008a). Finally, we added the distance modulus of NGC 6791, $(m-M)_{\rm F606W} = 13.44$, and its color excess E(F606W-F814W) = 0.14 (Bedin et al., 2008a,b) to obtain a synthetic white dwarf color-magnitude diagram, and from this we computed the corresponding white-dwarf luminosity function. The distance modulus adopted here agrees with the recent estimate of Grundahl et al. (2008), which is based on a cluster eclipsing binary system.

6.2.2 The cooling sequences

The cooling sequences adopted in this chapter were those previously employed in chapter 5 — see also García-Berro et al. (2010) — which were extensively discussed in chapter 4 — see also Althaus et al. (2010c). These cooling sequences are appropriate for white dwarfs with hydrogen-rich atmospheres, and were computed from stellar models with the metallicity of NGC 6791. For non-DA white dwarfs a new set of cooling sequences was computed from the same set of progenitors, using the same physical inputs as adopted in Althaus et al. (2010c), the only difference being the chemical composition of the atmosphere, for which we adopted pure helium. The bolometric corrections and color transformations for this set of cooling sequences were those of Bergeron et al. (1995).

6.3 Results

6.3.1 A population of single helium-core white dwarfs?

As mentioned, the bright peak of the white-dwarf luminosity function of NGC 6791 has been attributed either to a huge population of binary white dwarfs (Bedin et al., 2008b) or to the existence of population of single helium-core white dwarfs(Hansen (2005); Kalirai et al. (2007)). This would indicate that at the very high metallicity of this cluster mass-loss at the tip of the red giant branch would be largely enhanced. This possibility has been recently investigated, among others, by Meng et al. (2008), who found — on the basis of specific assumptions about the minimum envelope mass of red or asymptotic giant-branch stars – that for $Z \gtrsim 0.02$ helium white dwarfs are likely the result of the evolution of stars with masses smaller than 1.0 $M_{\odot}$. However, Prada Moroni & Straniero (2009) have demonstrated that when the star loses the envelope and departs from the red giant branch with a core mass slightly smaller than that required for helium ignition, a non-negligible possibility of a late helium ignition exists, and low-mass carbon-oxygen white dwarfs, rather than helium-core white dwarfs, are produced. Thus, more studies to constrain a hypothetical population of single helium-core white dwarfs are needed.

To this end we have proceeded as follows. At the metallicity of NGC 6791, the helium-core mass at the helium flash is $\sim 0.45\,M_{\odot}$, practically constant with initial mass, up to the transition to non-degenerate cores (Weiss & Ferguson, 2009). Also, adopting an age of 8 Gyr, the mass at the turn-off is $\sim 1.15\,M_{\odot}$ and the maximum mass of progenitors that could have made a helium-core white dwarf is $\sim 1.8\,M_{\odot}$. This means that the range of masses of possible progenitors of single white dwarfs with helium cores is between ~ 1.15 and $\sim 1.8\,M_{\odot}$. Accordingly, we draw a pseudo-random number for the mass of the progenitor using our initial mass function and we consider that a fraction $f_{\rm He}$ of stars between 1.15 and $2.0\,M_{\odot}$ have lost the envelope near the tip of the red giant branch and produce helium-core white dwarfs with masses 0.2 and $0.5\,M_{\odot}$. The adopted cooling sequences for helium-core white dwarfs are those of Althaus et al. (2009d).

The results of our simulations are displayed in the top panels of Fig. 6.1, where we show the synthetic color-magnitude diagram and white-dwarf luminosity function of the cluster for the case in which we adopt $f_{\rm He} = 0.3$ and $f_{\rm bin} = 0$. Clearly, this scenario is unable to reproduce the bright peak of the white-dwarf luminosity function and the corresponding clump in the color-magnitude diagram. Indeed, most helium-core white dwarfs are located in the same region of the color-magnitude diagram where regular carbon-oxygen white dwarfs are placed, the only difference is the position of the cut-off. In fact, helium-core white dwarfs pile-up at higher luminosities than carbon-oxygen ones, as expected, but at luminosities slightly fainter than that of the observational bright peak. The net result of this is that the population of helium-core white dwarfs partially overlaps with the peak produced by normal

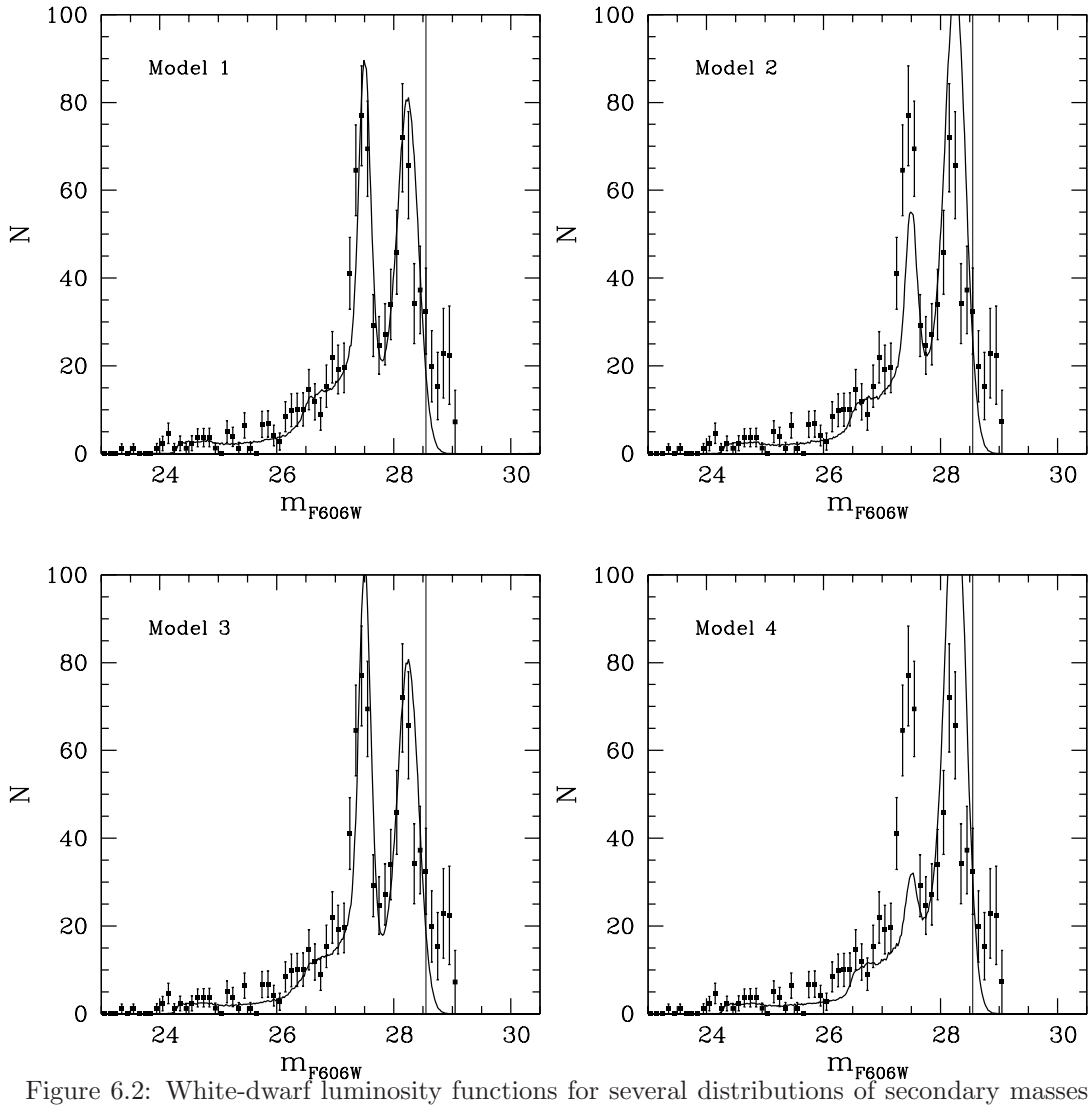

Figure 6.2: White-dwarf luminosity functions for several distributions of secondary masses of the progenitor binary system, see text for details.

carbon-oxygen white dwarfs and, consequently, the faint peak of the white-dwarf luminosity function broadens.

Now that we have established that single helium-core white dwarfs cannot explain the bright peak of the white-dwarf luminosity function, a natural question arises. Namely, which is the maximum fraction of these white dwarfs compatible with observations? To answer this question we performed additional simulations

using our fiducial model, in which a population of unresolved detached binaries is adopted — see Sect. 6.2.1 — and we added a small fraction $f_{\rm He}$ of helium-core white dwarfs, keeping the fraction of binary white dwarfs of the cluster constant. For illustrative purposes, the bottom panels of Fig. 6.1 show the case in which $f_{\rm He} = 0.3$ and $f_{\rm bin} = 0.54$ are adopted. A χ^2 test shows that the maximum fraction of single massive helium-core white dwarfs allowed by the observations is $f_{\rm He} = 0.05$.

6.3.2 The properties of the binary population

If the bright peak of the white-dwarf luminosity function of NGC 6791 can only be explained by a population of unresolved binary white dwarfs, their properties can be constrained using the white-dwarf luminosity function. There are other clusters (either open or globular) for which we have observational white-dwarf luminosity functions — M67 (Richer et al., 1998), NGC 2099 (Kalirai et al., 2001), NGC 188 (Andreuzzi et al., 2002), M4 (Hansen et al., 2004), and NGC 6397 (Hansen et al., 2007; Richer et al., 2008)) — and none of them shows a secondary peak in the white-dwarf luminosity function with the characteristics of that of NGC 6791. Perhaps the best studied of these clusters is NGC 6397. This cluster has been imaged down to very faint luminosities allowing Hansen et al. (2007) and Richer et al. (2008) to obtain a reliable white-dwarf luminosity function. The white-dwarf luminosity function of this very old — about 12 Gyr (di Criscienzo et al., 2010) — and metal-poor ([Fe/H]$\simeq -2.03 \pm 0.05$) globular cluster does not show any evidence of a large population of binary white dwarfs. There is another open cluster for which a large number of binaries has been found, M67 (Richer et al., 1998). The age of this cluster is 4.0 Gyr, and its metallicity is almost solar, [Fe/H]$\simeq -0.04$, but unfortunately the small number of white dwarfs with reliable photometry does not allow to perform a thorough study of its population of binary white dwarfs. All in all, NGC 6791 offers us the unique possibility to study the properties of the population of binaries in an open, very old and metal-rich cluster. In particular, we study how the white-dwarf luminosity function allows to constrain the distribution of secondary masses. However, before performing our analysis we note that blending may have the same effect than true unresolved binaries, although in the case of an open cluster, it is expected to be less frequent, owing to the lower density of stars. To quantify this, we distributed 900 synthetic white dwarfs (the observed number of stars) in the field of view of the HST CCD (4052×4052 pixels) and we evaluated the probability of chance superposition. We found that this probability is $\sim 0.8\%$ if the distance necessary to resolve two stars is ~ 10 pixels. Thus, for the case of NGC 6791 this possibility is quite unlikely, and the unresolved binary white dwarfs are most probably real systems.

We used four different models for the distribution of secondary masses in the progenitor bynary system, under the assumption — the same as in Bedin et al. (2008b) — that binary white dwarfs are produced by a primordial binary system.

Our first distribution is that already used by Bedin et al. (2008b), $n(q) = 0.0$ for $q < 0.5$ and $n(q) = 1.0$ otherwise, where $q = M_2/M_1$, being M_1 and M_2 the mass of the primary and of the secondary, respectively. We refer to this distribution as model 1. In model 2 we assume $n(q) = 1.0$, independently of the mass ratio. For model 3 we adopted $n(q) \propto q$. Finally, for our last set of simulations, corresponding to model 4, we adopted $n(q) \propto q^{-1}$.

We display the results of this set of simulations in Fig. 6.2. Evidently, the corresponding white-dwarf luminosity functions show dramatic differences. The distribution of secondary masses of Bedin et al. (2008b), top left panel, perfectly matches the observational white-dwarf luminosity function of NGC 6791. When model 2 is adopted, the secondary peak of the simulated luminosity function does not match the observational data, and the amplitude of the faintest peak is very much increased. It might be argued that this incongruence could be fixed by simply changing the fraction of binary white dwarfs, and indeed this could be done, but then one would need a present total percentage of binary stars well above 60%, which is probably unrealistic. Thus, we conclude that a flat distribution of secondary masses can be discarded. When the third distribution of secondary masses is used, we obtain a good fit to the observational data, although the quality of the fit is not as good as that of model 1. This is not surprising, since both distributions of secondary masses increase for increasing values of q. Finally, when model 4 is employed, the simulated white-dwarf luminosity function is totally incompatible with the observational data. The same arguments used when discussing the flat distribution of secondary masses apply here, and thus we can safely discard this distribution. We conclude that most likely only distributions of secondary masses that increase as the mass ratio of the two components of the binary increases are compatible with the existing observational data for NGC 6791.

6.3.3 Identification of cluster subpopulations: a test case

Our understanding of Galactic open and globular clusters has dramatically changed in recent years owing to the wealth of precise photometric data. This has allowed us to unveil the presence of multiple main sequences or subgiant branches — see, for instance, Piotto et al. (2007) and Milone et al. (2008) — in several globular clusters. Nowadays there is a handful of Galactic globular clusters in which the presence of several subpopulations is notorious. The best known of these clusters is ω Cen, for which four different metallicity regimes have been so far identified (Calamida et al., 2009). However, ω Cen is not the only example. For instance, Piotto et al. (2007) have convincingly shown that the main sequence of the globular cluster NGC 2808 contains three distinct subpopulations, while Milone et al. (2008) have demonstrated that NGC 1851 hosts a double subgiant branch, and di Criscienzo et al. (2010) have shown that NGC 6397 may contain a large number of second-generation stars. Thus, the presence of multiple populations in globular clusters is not an infrequent

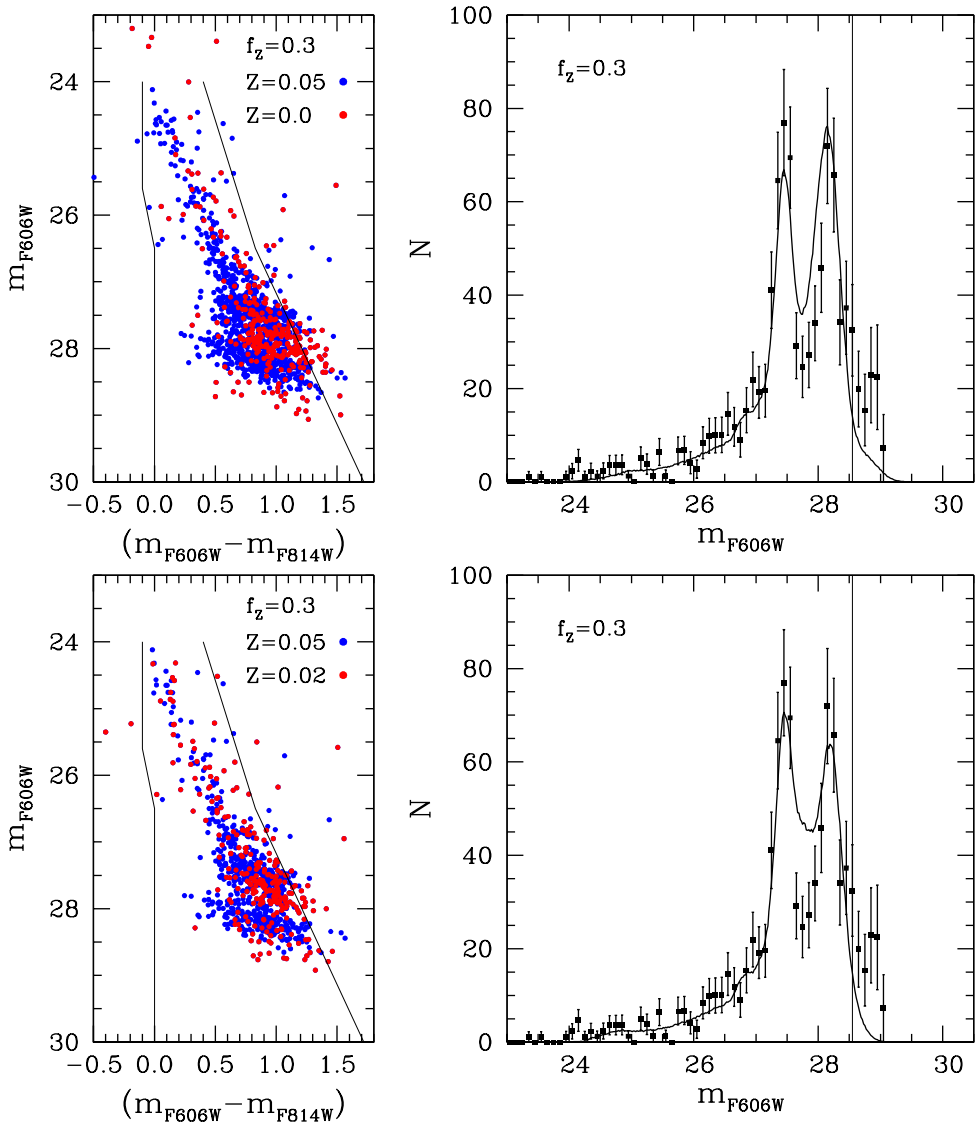

Figure 6.3: Color-color diagrams (left panels) of the simulated subpopulations of white dwarfs with metal-rich progenitors (blue circles) and metal-poor progenitors (red circles), for two metallicites of the subpopulations, $Z = 0.0$ (top panel) and $Z = 0.02$ (bottom) panel. In both cases we show the results for a fraction of the subpopulation $f_Z = 0.3$. The resulting white-dwarf luminosity functions (solid lines) are compared to the observational one (squares) in the right panels.

phenomenon.

To the best of our knowledge there is no evidence for the occurrence of this phenomenon in old open clusters. NGC 6791 is particularly well suited to study this possibility. Firstly, it is very old, a characteristic shared with globular clusters. Secondly, NGC 6791 is extremely metal-rich. The origin of this metallicity enhancement is still unknown, but arguably could be due to the existence of a previous generation of metal-poor stars. Nevertheless, we stress that in other clusters these subpopulations are observed as multiple values of [Fe/H] (and also helium), but a recent spectroscopical analysis of NGC 6791 by Origlia et al. (2006) shows that there is no spread in [Fe/H], and no spread in carbon or oxygen, which are two of the elements involved in the related subpopulations. Also, the well-defined red giant branch argues against this hypothesis. However, there are other clusters, of which NGC 6397 is the best example, which show remarkably clean color-magnitude diagrams with very tight main sequences and compact blue horizontal branches — that is, with no obvious photometric signs of multiple populations — for which subpopulations have already been identified (Lind et al., 2011). Finally, nobody has yet explored the possibility of using the white-dwarf luminosity function to put constraints on multiple subpopulations in clusters, although Prada Moroni & Straniero (2007) already noted that the white dwarf isochrones are considerably affected by metallicity variations. Thus, it is interesting to carry out this sensitivity study taking advantage of the well-populated white dwarf color-magnitude diagram, to test whether just modeling the white dwarf population can exclude the presence of subpopulations generated by progenitors with a metallicity different from the one measured spectroscopically.

To perform this study, we first considered varying fractions f_Z of an extreme subpopulation with zero metallicity. The pre-white dwarf lifetimes were taken from Marigo et al. (2001), whilst the carbon-oxygen stratification in the white dwarf models was kept unchanged, given the small effect of the progenitor initial chemical composition on the final carbon-oxygen profiles and cooling times at fixed white dwarf mass — see, for instance, Salaris et al. (2010) and Renedo et al. (2010). We also neglected the delay introduced by ^{22}Ne sedimentation, to account for the negiglible abundance of this element in $Z = 0$ models. The reason for this is the following. ^{22}Ne is produced during the helium burning phase by the chain of reactions $^{14}\mathrm{N}(\alpha,\gamma)^{18}\mathrm{F}(\beta^+)^{18}\mathrm{O}(\alpha,\gamma)^{22}\mathrm{Ne}$. The net effect is to transform essentially all ^{14}N into ^{22}Ne. In the extreme case of $Z = 0$ stars some ^{14}N is produced when the CNO cycle is activated by the ^{12}C produced by 3α reactions ignited by the high temperatures during the main sequence phase of metal free stars. However, its abundance mass fraction is $\lesssim 10^{-9}$ (Weiss et al., 2000).

The results of our simulations are shown in Fig. 6.3. We begin by discussing the color-magnitude diagram shown in upper left panel. Obviously, white dwarfs resulting from metal-poor progenitors detach from the bulk of the population, and several of these synthetic white dwarfs can be found below the well-defined cut-off of the observed cooling sequence, as expected, because the lack of ^{22}Ne causes a faster

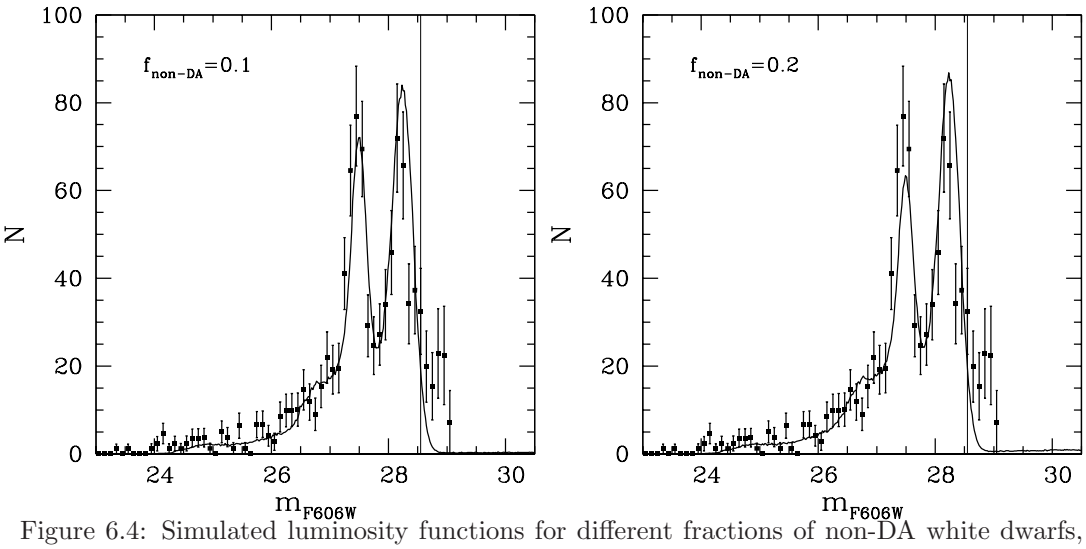

Figure 6.4: Simulated luminosity functions for different fractions of non-DA white dwarfs, as shown in the corresponding panel.

cooling. The upper right panel of this figure shows the corresponding luminosity function. The overall agreement with the observed luminosity function is poor, especially in the region between the two peaks. An increase of the binary fraction to reproduce the bright peak better would not improve the modeling of the region between the peaks. The natural question to address is then which is the maximum fraction of metal-poor white dwarf progenitors that can be accommodated within the observational white-dwarf luminosity function? To this purpose we have computed synthetic white dwarf samples with decreasing fractions of metal-poor progenitors, and we ran a χ^2 test. We found that the maximum allowed fraction of metal-poor progenitors is $f_Z = 0.12$. Obviously, the assumption that this subpopulation has zero metallicity is probably to extreme. Consequently, we repeated the same calculation for a subpopulation of solar metallicity – see the bottom panels of Fig. 6.3. In this case the maximum fraction of solar-metallicity progenitors is $f_Z = 0.08$.

6.3.4 The fraction of non-DA white dwarfs

We now focus on the possibility of determining the fraction of non-DA white dwarfs in NGC 6791. The spectral evolution of white dwarf atmospheres is still a controversial question, and although the ratio of white dwarfs with pure hydrogen atmosphere versus white dwarfs with hydrogen-deficient atmospheres is known for the local field, very few determinations exist for open and globular clusters. Moreover, although for the field white dwarf population the canonical percentage is around 80%, observations show that this ratio depends on the effective temperature — see, for instance,

Tremblay & Bergeron (2008) and references therein. However, the only reliable determinations for open clusters are those of Kalirai et al. (2005) for the rich, young cluster NGC 2099, and Rubin et al. (2008) for NGC 1039. Kalirai et al. (2005) found a clear deficit of non-DA white dwarfs in NGC 2099, whereas Rubin et al. (2008) found that the fraction of non-DA white dwarfs in the open cluster NGC 1039 is $\sim$ 10%, at most. Clearly, investigating the DA to non-DA ratio in another open cluster is therefore of greatest interest.

We addressed this question by simulating the cluster population of white dwarfs with an increasing fraction of non-DA stars. The non-DA fractions adopted here are $f_{\rm non-DA} = 0.0$, 0.1, 0.2 and 0.4, respectively. For the sake of conciseness, we only show the results for $f_{\rm non-DA} = 0.1$ — left panel — and 0.2 — right panel. As shown in Fig. 6.4 the white-dwarf luminosity function is sensitive to the ratio of non-DA to DA white dwarfs. We find that when the fraction of non-DA white dwarfs is increased, the agreement with the observational white-dwarf luminosity function rapidly degrades. To be precise, when the fraction of non-DA white dwarfs is $f_{\rm non-DA} = 0.1$, the agreement is quite poor, and when the fraction of non-DA white dwarfs is that of field white dwarfs, $f_{\rm non-DA} = 0.2$, the quality of the fit to the observational white-dwarf luminosity function is unacceptable. This is because for the age of NGC 6791 non-DA and DA white dwarfs pile-up at similar luminosities. As a consequence, adding single non-DA white dwarfs lowers the height of the bright peak compared to the faint one.

To quantify which the maximum fraction of non-DA white dwarfs that can be accommodated within the observational errors is, we conducted a χ^2 test, and we found that for fractions of non-DA white dwarfs larger than $\sim$ 0.1 the probability rapidly drops below $\sim$ 0.7, whereas for $f_{\rm non-DA} = 0.0$ the probability is $\sim$ 0.9. Consequently, the fraction of non-DA white dwarfs in NGC 6791 can roughly be at most half the value found for field white dwarfs. This result qualitatively agrees with the findings of Kalirai et al. (2005), who find that for NGC 2099 this deficit of non-DA white dwarfs is even higher. As a matter of fact, Kalirai et al. (2005) found that for this cluster all white dwarfs in their sample were of the DA type. Our results also point in the same direction, although a fraction of $\sim$ 5% is still compatible with the observed white-dwarf luminosity function of NGC 6791, in agreement with the findings of Kalirai et al. (2007).

Finally, we considered also the possibility that the fraction of non-DA white dwarfs changes with the effective temperature, which occurs with field white dwarfs. In particular, we assumed that for effective temperatures higher than 6 000 K, the fraction of non-DA white dwarfs is $f_{\rm non-DA} = 0.2$ and for temperatures ranging from 5 000 K to 6 000 K, $f_{\rm non-DA} = 0.0$, as suggested by observations of low-luminosity field white dwarfs. In this case we find that the simulated white-dwarf luminosity function and color-magnitude diagram are very similar to those in which $f_{\rm non-DA} =$ 0.0, and thus agree very well with the observational luminosity function of NGC 6791. Nevertheless, it is worth noting that using this prescription, the fraction of

non-DA white dwarfs expected in the cluster would be about 6%. Thus, on the basis of these simulations it cannot be discarded that this cluster could have originally produced a large percentage of non-DA white dwarfs, but at the present age of the cluster, most of them could have been transformed into DA white dwarfs as a result of accretion episodes.

These conclusions clearly depend on the assumed fraction of binary white dwarfs that populate the cluster. The fraction of white dwarf binaries necessary to explain the bright peak of the luminosity function (in absence of non-DA objects) requires that about 54% of the objects in NGC 6791 be binaries. An increased white dwarf binary percentage (75%) can in principle accommodate a higher percentage (20%) of non-DA objects by increasing the relative height of the bright peak in the synthetic sample, compared to the faint one, but it seems unrealistic to accept such a large percentage of cluster binaries, hence non-DA white dwarfs.

6.4 Summary and conclusions

In this chapter we have investigated several important properties of the stellar population hosted by the very old (8 Gyr), metal-rich ([Fe/H]$\simeq$ 0.4) open cluster NGC 6791. This cluster has been imaged below the luminosity of the termination of its white dwarf cooling sequence (Bedin et al., 2005, 2008a). The resulting white-dwarf luminosity function enables us not only to determine the cluster age (García-Berro et al., 2010), but other important properties as well. Among these, we mention the properties of the population of unresolved binary white dwarfs, the existence of cluster subpopulations, and the fraction of non-DA white dwarfs.

The origin of the bright peak of the white-dwarf luminosity function was investigated, exploring in detail the alternative massive helium-core white dwarf scenario. Our conclusion is that this peak cannot be attributed to a population of single helium-core white dwarfs. The more realistic possibility left to explain this feature is a population of unresolved binary white dwarfs. This huge population of unresolved binary white dwarfs has allowed us to study the properties of the parent population. To this purpose, we studied the properties of the distribution of secondary masses in the binary progenitor system and its effects in the white-dwarf luminosity function. Specifically, we tested four different distributions of secondary masses and we found that only those distributions that are monotonically increasing with the mass ratio are consistent with the observational data. Additionally, as a test case, we verified the ability of the white-dwarf luminosity function to assess the existence of subpopulations within a stellar system. We have found that the presence of a $Z = 0$ subpopulation is inconsistent with the white-dwarf luminosity function, the maximum fraction allowed by the data being 12%. If the metallicity of the subpopulation is solar, this fraction is 8%.

Finally, we found that the fraction of non-DA white dwarfs in this cluster is un-

usually small, on the order of 6% at most, and much smaller than the corresponding one for field white dwarfs, which is $\sim 20\%$. This shortage of non-DA white dwarfs is a characteristic shared with another open cluster, NGC 2099. However, the deficit of non-DA white dwarfs is even higher in the case of NGC 2099, given that for this cluster recent exhaustive observations have found no single white dwarf of the non-DA type (Kalirai et al., 2005).

Chapter 7

Summary and conclusions

In this last chapter we summarize the most important results reported in this thesis and we draw the main conclusions. This thesis has been structured in two different parts. We discuss them separately in the following sections.

7.1 Summary

7.1.1 Theory

We begin describing our theoretical approach. Specifically, we computed several set of up-to-date white dwarf evolutionary sequences, using latest generation physical inputs. This was done in chapters 2, 3 and 4.

In a first set of simulations we computed the cooling ages of a grid of white dwarf models. We adopted two different metallicities, a metallicity typical of most Galactic globular clusters, $Z = 0.001$, thus allowing to obtain accurate ages for metal-poor stellar systems, as well as solar metallicity, $Z = 0.01$, which allows us to obtain accurate ages for white dwarfs in the local Galactic disk. To compute these sequences ee employed the `LPCODE` evolutionary code, which is based on detailed and updated constitutive physics. We emphasize that our evolutionary sequences were self-consistently evolved from the zero age main sequence, through the core hydrogen and helium burning evolutionary phases to the thermally pulsing asymptotic giant branch and, ultimately, to the white dwarf stage. To the best of our knowledge, this is the first set of self-consistent evolutionary sequences covering different initial masses and metallicities.

We also analyzed this set of new white dwarf evolutionary sequences, which are appropriate for precision for asteroseismological studies of ZZ Ceti stars. In particular, we computed new chemical profiles for the core and envelope of white dwarfs which are intented for asteroseismological studies of ZZ Ceti stars that require realistic chemical profiles throughout the white dwarf interiors. These profiles were

derived from the full and complete evolution of progenitor stars, and were based on the calculations reported in chapter 2 — see also Renedo et al. (2010).

Finally, we studied the role of ^{22}Ne diffusion on the evolution of white dwarf stars with high-metallicity progenitors. We computed a grid of white dwarf evolutionary sequences that incorporates for the first time the energy contributions arising from both ^{22}Ne sedimentation and carbon-oxygen phase separation. The grid covers the entire mass range expected for carbon-oxygen white dwarfs, from 0.52 to 1.0 $M_{\odot}$, and it is based on a detailed and self-consistent treatment of these energy sources. Except for the 1.0 $M_{\odot}$ sequence, the history of progenitor stars was taken into account by evolving initial stellar configurations in the mass range 1 to 5 $M_{\odot}$ from the ZAMS all the way through the thermally pulsing AGB and mass loss phases. Because of the full calculation of the evolution of progenitor stars, the white dwarf sequences incorporates realistic and consistent carbon-oxygen profiles — of relevance for an accurate computation of the energy released by carbon-oxygen phase separation. In addition, detailed non-gray model atmospheres are used to derive the outer boundary condition for the evolving sequences. This is important because at the low luminosities where the process of ^{22}Ne sedimentation becomes relevant, the outer boundary conditions influence the cooling times.

7.1.2 Applications

In the second part of this work we employed all the theoretical advances presented previously to model the population of white dwarfs of the well-studied metal-rich, open cluster NGC 6791 (Bedin et al., 2005). This was done in chapters 5 and 6. This cluster is so close to us that can be imaged down to luminosities fainter than that of the termination of its white-dwarf cooling sequence (Bedin et al., 2008a), thus allowing for an in-depth study of its white dwarf population. We used a Monte Carlo simulator that employs up-to-date evolutionary cooling sequences for white dwarfs with hydrogen-rich and hydrogen-deficient atmospheres, with carbon-oxygen and helium cores. The cooling sequences for carbon-oxygen cores account for the delays introduced by both ^{22}Ne sedimentation in the liquid phase and by carbon-oxygen phase separation upon crystallization. We use observations of the white-dwarf cooling sequence to constrain important properties of the cluster stellar population, such as the age, the existence of a putative population of massive helium-core white dwarfs, and the properties of a large population of unresolved binary white dwarfs. We also investigate the use of white dwarfs to disclose the presence of cluster subpopulations with a different initial chemical composition, and we obtain an upper bound to the fraction of hydrogen-deficient white dwarfs.

7.2 Conclusions

As mentioned previously, this thesis has focused on the study of white dwarfs from two different approaches, which are complementary. Again we draw our conclusions and discuss their significance separately.

7.2.1 Theory

With respect to the computation of new cooling sequences for hydrogen-rich DA white dwarfs our main findings can be summarized as follows. We correctly reproduced the observed initial-to-final mass relationship of white dwarfs, in excellent agreement with the recent results of Salaris et al. (2009) for white dwarfs with solar metallicity progenitors. We also corroborated the importance of convective coupling at low luminosity in the cooling of white dwarfs, as originally suggested by Fontaine et al. (2001). We demonstrated as well the importance of residual hydrogen burning in white dwarfs resulting from low-metallicity progenitors. We confirmed the importance of carbon-oxygen phase separation upon crystallization, in good qualitative agreement with the results of Garcia-Berro et al. (1988a,b), Segretain et al. (1994), Salaris et al. (1997) and Salaris et al. (2000). Although the computed delays are smaller than those previously estimated by Segretain et al. (1994), they are larger than those computed by Salaris et al. (2000), and are by no means negligible if precision white dwarf cosmochronology is to be done. However, we would like to mention that these delays depend crucially on the previous evolutionary history of white dwarf progenitors and, particularly, on the rate of the $^{12}C(\alpha,\gamma)^{16}O$ nuclear reaction, as well as on the adopted treatment for convective mixing. We also reproduced the well-known blue hook of very old hydrogen-rich white dwarfs caused by H_2-H_2 collision-induced absorption (Hansen, 1999). Finally, we showed the impact of Lyα quasi-molecular opacity on the evolution of cool white dwarfs in the color-magnitude diagram.

We would like to emphasize that our full treatment of the entire evolutionary history of white dwarfs has allowed us to obtain consistent white dwarf initial configurations. Specifically, we computed self-consistently the mass of the hydrogen-rich envelope and of the helium buffer. That is, they were obtained from evolutionary calculations, instead of using typical values and artificial initial white dwarf models. This has implications for the cooling rates of old white dwarfs, as the thicknesses of these outer layers control the cooling speed of such white dwarfs. We also obtained self-consistent interior chemical profiles. this has relevance for the cooling of white dwarfs, as the release of latent heat and gravitational energy due to carbon-oxygen phase separation upon crystallization crucially depend on the previous evolutionary history of white dwarfs. Also, the chemical stratification of white dwarf progenitors is important for correctly computing the specific heat of white dwarf interiors.

All these results were computed with the most accurate physical inputs and with

a high degree of detail and realism. In particular, our calculations include nuclear burning at the very early phases of white dwarf evolution — which is important to determine the final thickness of the hydrogen-rich envelope — diffusion and gravitational settling — which are important to shape the profiles of the outer layers — accurate neutrino emission rates — which control the cooling at high luminosities — a correct treatment of crystallization and phase separation of carbon and oxygen — which dominate the cooling times at low luminosities — a very detailed equation of state — which is important in all the evolutionary phases — and improved non-gray model atmospheres — which allow for a precise determination of white dwarf colors and outer boundary conditions for the evolving models.

With regards to the computation of chemical profiles for the asteroseismology of ZZ Ceti stars we discussed the importance of the initial-final mass relationship for carbon-oxygen white dwarfs. A reduction of the efficiency of extra-mixing episodes during the thermally-pulsing AGB phase, supported by different pieces of theoretical and observational evidence, yields a gradual increase of the hydrogen-free core mass as evolution proceeds during this phase. As a result, the initial-final mass relationship by the end of the thermally-pulsing AGB is markedly different from that resulting from considering the mass of the hydrogen free core right before the first thermal pulse. We found that this issue has implications for the carbon-oxygen composition expected in a white dwarf. In particular, the central oxygen abundance may be underestimated by about 15% if the white dwarf mass is assumed to be the hydrogen-free core mass before the first thermal pulse. We stress that the chemical profiles expected in the outermost layers of ZZ Ceti stars are sensitive to the computation of the thermally-pulsing AGB phase and of the phase in which element diffusion is relevant. We find a strong dependence of the outer layer chemical stratification on the stellar mass. In the less massive models, the double-layered structure in the helium layer built up during the thermally-pulsing AGB phase is not removed by diffusion by the time the ZZ Ceti stage is reached. This has profound implications since our new chemical profiles has consequences in the pulsational properties of ZZ Ceti stars when performing adiabatic pulsation calculations. Specifically, the whole $g-$mode period spectrum and the mode-trapping properties of these pulsating white dwarfs as derived from our new chemical profiles are substantially different from those based on the most widely used chemical profiles in existing asteroseismological studies. Accordingly, we expect the best fit parameters of asteroseismological studies using the `LPCODE` chemical profiles to differ significantly from those found in studies made so far (Bischoff-Kim et al. (2008), and Castanheira & Kepler (2008)). Further studies will show in what way.

Concerning the role of ^{22}Ne diffusion on the evolution of white dwarf stars with high-metallicity progenitors we found that the evolution of cool white dwarfs stemming from those progenitor stars is strongly modified by the energy released from ^{22}Ne sedimentation. The related energy release strongly delays their cooling. The precise value of the delays depends on the mass of the white dwarf, its luminosity

and on the metal content. The impact of ^{22}Ne sedimentation starts earlier in more massive white dwarfs because of their larger gravities. Appreciable delays in the cooling rates start to manifest themselves at luminosities of $\log(L/L_{\odot}) \approx -3.5$ to -4.2. The magnitude of the delays in the cooling rates resulting from ^{22}Ne sedimentation is comparable (or even larger in the case of $Z = 0.06$) to the delays induced by carbon-oxygen phase separation.

7.2.2 Applications

With respect to the use of white dwarf theoretical cooling evolutionary sequences we stress that this offers us a unique tool to study both open and globular clusters. In this sense, we constrained the main properties of NGC 6791, which is a well studied metal-rich ([Fe/H]$\simeq 0.4$) open cluster (Bedin et al., 2005) that it is so close to us that can be imaged down to very faint luminosities (Bedin et al., 2008a). The resulting white-dwarf luminosity function enables us not only to determine the cluster age, solving the age discrepancy between the main sequence turn-off age (~ 8 Gyr) and the age derived from the termination of the white dwarf cooling sequence (~ 6 Gyr). At the approximate location of the faint peak in the white dwarf luminosity function of this open cluster, delays between 1 and 1.5 Gyr are expected as a result of ^{22}Ne sedimentation only. At lower temperatures, white dwarfs are expected to crystallize and phase separation of the main constituents of the core of a typical white dwarf, ^{12}C and ^{16}O, is expected to occur (Garcia-Berro et al., 1988b,a). This sequence of events introduces significant delays in the cooling times (Segretain et al., 1994; García-Berro et al., 2008), but was not hitherto been proven until now. That is, as theoretically anticipated (Deloye & Bildsten, 2002; Garcia-Berro et al., 1988b)), physical separation processes occur in the cores of white dwarfs.

The properties of the population of unresolved binary white dwarfs of this cluster have been also investigated. The origin of the bright peak of the white-dwarf luminosity function was studied, exploring in detail the alternative massive helium-core white dwarf scenario. Our conclusion is that this peak cannot be attributed to a population of single helium-core white dwarfs. The more realistic possibility left to explain this feature is a population of unresolved binary white dwarfs. We also studied the properties of the distribution of secondary masses in the binary progenitor system and its effects in the white-dwarf luminosity function. Specifically, we tested four different distributions of secondary masses and we found that only those distributions that are monotonically increasing with the mass ratio are consistent with the observational data. With regards to the existence of cluster subpopulations, we have found that the presence of a $Z = 0$ subpopulation is inconsistent with the white-dwarf luminosity function, the maximum fraction allowed by the data being 12%. If the metallicity of the subpopulation is solar, this fraction is 8%. We also found that the fraction of non-DA white dwarfs in this particular cluster is surprinsingly small, on the order of 6% at most, and much smaller than the corresponding one for field

white dwarfs, which is $\sim 20\%$.

Appendix A

Stellar evolutionary and pulsational codes

This appendix describes briefly two different numerical codes used in this thesis. The first of these is the stellar evolutionary code LPCODE (Althaus et al., 2003, 2005c), which is described in Sect. A.1. This code was used to compute all evolutionary sequences described in the main body of this work. In Sect. A.2 we introduce the pulsational code — see more details in Córsico et al. (2001b), and Córsico & Althaus (2006) — which was used to study the properties of ZZ Ceti stars.

A.1 Stellar evolutionary code: (LPCODE)

The evolutionary calculations presented in this thesis were done with an updated version of the LPCODE stellar evolutionary code — see Althaus et al. (2005c) and references therein. This code was developed several years ago (Althaus et al., 2003), and yields very reliable results. In recent years, the LPCODE stellar evolutionary code has been employed to study different aspects of the evolution of low-mass stars, such as the formation and evolution of H-deficient white dwarfs, PG 1159 and extreme horizontal branch stars (Althaus et al., 2005c; Miller Bertolami & Althaus, 2006; Miller Bertolami et al., 2008; Althaus et al., 2009a) and, more recently, it has also been used to study the formation of hot DQ white dwarfs (Althaus et al., 2009b), the evolution of He-core white dwarfs with high metallicity progenitors (Althaus et al., 2009d), and the evolution of hydrogen-deficient white dwarfs (Althaus et al., 2009c). Moreover, this code has also been used to study the white dwarf initial-final mass relationship (Salaris et al., 2009). A recent test of the code and a thorough comparison of the results obtained using LPCODE with those obtained using other evolutionary codes has recently been made in (Salaris et al., 2009). Details of LPCODE can be found in these works and in Althaus et al. (2009c). For these reasons, in what follows, we only introduce the code and the main physical input physics, namely,

those that are relevant for the evolutionary calculations presented in this thesis.

LPCODE is based on the Henyey method for calculating stellar evolution presented in Kippenhahn et al. (1967). A system of equations of structure and evolution (hydrostatic equilibrium, conservation of mass, conservation of energy, and transport of energy) in a spheric symmetry is solved iteratively using a Newton-Raphson technique. The independent variable is a Lagrangian variable defined by $\xi = \ln(1 - M_r/M_*)$, and the dependent variables are: radius (r), pressure (P), luminosity (l) and temperature (T). Envelope integrations from photospheric starting values inward to a fitting outer mass fraction (close to the photosphere) are performed to specify the outer boundary conditions. The following change of variables is considered in LPCODE:

$$\begin{aligned} \theta^{(n+1)} &= \theta^{(n)} + \ln(1 + u_\theta) \\ p^{(n+1)} &= p^{(n)} + \ln(1 + u_p) \\ x^{(n+1)} &= x^{(n)} + \ln(1 + u_x) \\ l^{(n+1)} &= l^{(n)} + u_l \end{aligned} \tag{A.1}$$

with u_θ, u_p, u_x and u_l being the quantities to be iterated that are given by

$$u_\theta = \frac{\Delta T}{T^{(n)}},$$

$$u_p = \frac{\Delta P}{P^{(n)}},$$

$$u_x = \frac{\Delta r}{r^{(n)}},$$

and

$$u_l = \Delta l$$

, where superscripts n and $n+1$ denote the beginning and end of time interval (where $t_{n+1} = t_n + \Delta t$). Moreover, $\theta = \ln T$, $x = \ln r$ and $p = \ln P$ are the dependent variables in the dimensionless form of the code.

The evolution of the chemical composition is described by a simultaneous time-dependent set of equations where is taking into account chemical changes in all chemical elements considered caused by nuclear burning and mixing, such as convection, microscopic diffusion or Rayleigh-Taylor's instabilities. Note that different physical processes take place different evolutionary phases, which are taken into account in LPCODE. The structure and chemical equations are not solved instantaneous simultaneously. Briefly our iterative method can describe as: given a certain values to structure variables (T, P, r and l) at time t_n, the chemical composition is calculated at time t_{n+1}; those chemical variables at t_{n+1} are used to calculate structure variables t_{n+1}, which in turn are used to calculate the chemical variables at t_{n+2} and so on and so forth. We want to mention that LPCODE is able to follow the complete evolution of the star model from the main sequence to the white dwarf end phase.

A.1.1 Input physics

To begin with, we recall that the radiative opacities employed in our calculations were those of the OPAL project (Iglesias & Rogers, 1996), including carbon- and oxygen-rich compositions, supplemented at low temperatures with the Alexander & Ferguson (1994) molecular opacities. For the present calculations, we have not considered carbon-enriched molecular opacities (Marigo, 2002), which are expected to reduce effective temperatures at the AGB (Weiss & Ferguson, 2009). We adopted the conductive opacities of Cassisi et al. (2007), which cover the entire regime where electron conduction is relevant. Neutrino emission rates for pair, photo, and bremsstrahlung processes were those of Itoh et al. (1996), while for plasma processes we included the treatment presented in Haft et al. (1994).

LPCODE considers a simultaneous treatment of non-instantaneous mixing and burning of elements. Specifically, abundance changes are described by the set of equations

$$\left(\frac{d\vec{X}}{dt}\right) = \left(\frac{\partial\vec{X}}{\partial t}\right)_{\rm nuc} + \frac{\partial}{\partial M_r}\left[(4\pi r^2\rho)^2 D\frac{\partial\vec{X}}{\partial M_r}\right], \tag{A.2}$$

where $\vec{X}$ is a vector containing the abundances of all the elements. In this equation, the first term describes the nuclear evolution, and it is fully coupled to the current composition change due to mixing processes, as represented by the second term. In particular, the efficiency of convective mixing is described by the diffusion coefficient D, which in this thesis is given by the mixing length theory. The nuclear network accounts explicitly for the following 16 elements: ^{1}H, ^{2}H, ^{3}He, ^{4}He, ^{7}Li, ^{7}Be, ^{12}C, ^{13}C, ^{14}N, ^{15}N, ^{16}O, ^{17}O, ^{18}O, ^{19}F, ^{20}Ne and ^{22}Ne, together with 34 thermonuclear reaction rates of the pp chains, CNO bi-cycle, helium burning, and carbon ignition that are identical to those described in Althaus et al. (2005c), with the exception of the reaction $^{12}\mathrm{C} + p \rightarrow {}^{13}\mathrm{N} + \gamma \rightarrow {}^{13}\mathrm{C} + e^{+} + \nu_{\rm e}$ and ^{13}C(p, γ)^{14}N, for which we adopted the rate of Angulo et al. (1999). In particular, it is worth noting that the $^{12}\mathrm{C}(\alpha,\gamma)^{16}\mathrm{O}$ reaction rate — which is of special relevance for the carbon-oxygen stratification of the emerging white dwarf core — adopted here was also that of Angulo et al. (1999).

In passing, we mention that a detailed inner composition is required for a proper computation of the energy released by the redistribution of chemical elements during crystallization of the white dwarf core. Specifically, the energy released during this process, and the resulting impact on the cooling ages of faint white dwarfs, increases for larger carbon abundances (Isern et al., 1997, 2000). The standard mixing length theory for convection — with the free parameter $\alpha = 1.61$ — was adopted. With this value, the present luminosity and effective temperature of the Sun, $\log T_{\rm eff} = 3.7641$ and $L_{\odot} = 3.842 \times 10^{33}$ erg s^{-1}, at an age of 4 570 Myr, are reproduced by LPCODE when $Z = 0.0164$ and $X = 0.714$ are adopted — in agreement with the Z/X value

of Grevesse & Sauval (1998).

During the evolutionary stages prior to the thermally pulsing AGB (TP-AGB) phase, we allowed the occurrence of extra-mixing episodes beyond each convective boundary following the prescription of Herwig et al. (1997). As well known, the occurrence of extra-mixing episodes is of relevance for the final chemical stratification of the white dwarfs, particularly during the late stage of core helium burning phase — see Prada Moroni & Straniero (2002) and Straniero et al. (2003). We treated extra-mixing as a time-dependent diffusion process — by assuming that mixing velocities decay exponentially beyond each convective boundary — with a diffusion coefficient given by $D_{\rm EM} = D_{\rm O}\ \exp(-2z/fH_{\rm P})$, where $H_{\rm P}$ is the pressure scale height at the convective boundary, $D_{\rm O}$ is the diffusion coefficient of unstable regions close to the convective boundary, and z is the geometric distance from the edge of the convective boundary (Herwig et al., 1997). The free parameter f describes the efficiency of the extra-mixing process. For all our sequences we adopted $f = 0.016$, a value inferred from the width of the upper main sequence. Except in the case of the sequence of $1.25\,M_{\odot}$ with $Z = 0.001$ (see Chapter 2), the size of the convective core on the main sequence is small. In this case we used $f = 0.008$ during the core hydrogen burning phase. Abundance changes resulting from extra-mixing were fully coupled to nuclear evolution, following Eq. (A.2). For the white dwarf regime, convection was treated in the formalism of the mixing length theory, as given by the ML2 parameterization (Tassoul et al., 1990).

In the present study, extra-mixing episodes were disregarded during the TP-AGB phase. In particular, a strong reduction (a value of f much smaller than 0.016) of extra-mixing episodes at the base of the pulse-driven convection zone seems to be supported by simulations of the $s-$process abundance patterns (Lugaro et al., 2003) and, more recently, by observational inferences of the initial-final mass relation (Salaris et al., 2009). As a result, it is expected that the mass of the hydrogen-free core of our sequences gradually grows as evolution proceeds through the TP-AGB. This is because a strong reduction or suppression of extra-mixing at the base of the pulse-driven convection zone strongly inhibits the occurrence of third dredge-up, thus favoring the growth of the hydrogen-free core. The implications of this treatment for the theoretical initial-final mass relation had been discussed in chapter 2 — see also Renedo et al. (2010), Salaris et al. (2009) and Weiss & Ferguson (2009). The breathing pulse instability occurring towards the end of core helium burning was suppressed — see Straniero et al. (2003) for a discussion of this point.

Mass loss was considered during core helium burning and red giant branch phases following Schröder & Cuntz (2005). During the AGB and TP-AGB phases, we considered the prescription of Vassiliadis & Wood (1993). In the case of a strong reduction of third dredge-up, as occurred in our sequences, mass loss plays a major role in determining the final mass of the hydrogen-free core at the end of the TP-AGB evolution, and thus the initial-final mass relation. In particular, mass loss erodes the hydrogen-rich envelope of the star and limits the additional growth of the core mass

during the TP-AGB. This is quite different from the situation in which appreciable third dredge-up takes place, in which case the final core mass at the TP-AGB phase is not very different from the mass at the first thermal pulse (Weiss & Ferguson, 2009), and the role of mass loss becomes less relevant.

For the white dwarf regime, the physical inputs considered in LPCODE were completely revised and updated from those considered in our previous studies, particularly regarding the treatment of crystallization. With regard to the microphysics, for the high-density regime, we used the equation of state of Segretain et al. (1994), which accounts for all the important contributions for both the liquid and solid phases — see Althaus et al. (2007) and references therein. For the low-density regime, we used an updated version of the equation of state of Magni & Mazzitelli (1979). Radiative and conductive opacities are those described at the beginning of this section. In particular, conductive opacities are considered for densities larger than that at which the main chemical constituents are completely pressure-ionized. During the white dwarf regime, the metal mass fraction Z in the envelope is not assumed to be fixed, rather, it is specified consistently acording to the prediction of element diffusion. To account for this, we considered radiative opacities tables from OPAL for arbitrary metallicities. For effective temperatures less than 10 000K we include the effects of molecular opacity by assuming pure hydrogen composition from the computations of Marigo & Aringer (2009). This assumption is justified because element diffusion leads to pure hydrogen envelopes in cool white dwarfs.

As well known, there are several physical processes that change the chemical abundance distribution of white dwarfs along their evolution. In particular, element diffusion strongly modifies the chemical composition profile throughout their outer layers. In this thesis, we computed the white dwarf evolution in a consistent way with the changes of chemical abundance distribution caused by element diffusion along the entire cooling phase. As a result, our sequences developed pure hydrogen envelopes, the thickness of which gradually increases as evolution proceeds. We considered gravitational settling and thermal and chemical diffusion — but not radiative levitation, which is only relevant at high effective temperatures for determining the surface composition — of ^{1}H, ^{3}He, ^{4}He, ^{12}C, ^{13}C, ^{14}N and ^{16}O, see Althaus et al. (2003) for details. In particular, our treatment of time-dependent diffusion is based on the multicomponent gas treatment presented in Burgers (1969). In LPCODE, diffusion becomes operative once the wind limit is reached at high effective temperatures (Unglaub & Bues, 2000). We assume this to occur when the surface gravity of our models $g > g_{\rm diff}$, where $g_{\rm diff} = 7$ if $T_{\rm eff} > 90\,000K$ and $g_{\rm diff} = 6.4 + T_{\rm eff}/150\,000$ K if $T_{\rm eff} < 90\,000K$. For smaller gravities, wind mass-loss is high enough that prevents appreciable element diffusion from occurring. This prescription represents reasonably well the detailed simulations of Unglaub & Bues (2000) for the occurrence of wind limits in hydrogen-rich white dwarfs. Other physical process responsible for changes in the chemical profile of white dwarfs that we took into account is related to carbon-oxygen phase separation during crystallization. In this case, the resulting

release of gravitational energy considerably impacts the white dwarf cooling times. Abundance changes resulting from residual nuclear burning — mostly during the hot stages of white dwarf evolution — and convective mixing, were also taken into account in our simulations. In particular, the release of energy by proton burning was considered down to $\log(L/L_{\odot}) \approx -4$. The role of residual hydrogen burning in evolving white dwarfs is by no means negligible, particularly in the case of those white dwarfs resulting from low-metallicity progenitors. Finally, we considered the chemical rehomogenization of the inner carbon-oxygen profile induced by Rayleigh-Taylor instabilities following Salaris et al. (1997). These instabilities arise because the positive molecular weight gradients that remain above the flat chemical profile left by convection during helium core burning.

An important aspect of the present work was the inclusion of energy sources resulting from the crystallization of the white dwarf core. This comprises the release of latent heat and the release of gravitational energy associated with changes in the carbon-oxygen profile induced by crystallization. In this study, the inclusion of these two energy sources was done self-consistently and locally coupled to the full set of equations of stellar evolution. That is, we computed the structure and evolution of white dwarfs with the changing composition profile and with the luminosity equation appropriately modified to account for both the local contribution of energy released from the core chemical redistribution and latent heat. This constitutes an improvement over previous attempts (Salaris et al., 2000) to include the release of energy from phase separation in stellar evolutionary codes. Details about the numerical procedure to compute the energy sources from crystallization will be presented in a forthcoming work. Briefly, at each evolutionary timestep we computed the crystallization temperature and the change of chemical composition resulting from phase separation using the spindle-type phase diagram of Segretain & Chabrier (1993). This phase diagram provides the crystallization temperature (which depends on the chemical composition of the liquid phase) as a function of the crystallization temperature of a one component plasma. In our calculations, the one component plasma crystallization temperature is computed by imposing $\Gamma = 180$, where $\Gamma \equiv \langle Z^{5/3} \rangle e^2/a_{\rm e} k_{\rm B} T$ is the ion coupling constant, and $a_{\rm e}$ is the interelectronic distance. After computing the chemical compositions of both the solid and liquid phases we evaluated the net energy released in the process as in Isern et al. (1997), and added to it the latent heat contribution, of the order of $0.77 k_{\rm B} T$ per ion, which is usually smaller. Both energy contributions were distributed over a small mass range around the crystallization front. We mention that the magnitude of both energy sources was calculated at each iteration during the convergence of the model.

A.2 Pulsational code

The pulsational calculations presented in this thesis were done with an updated version of the pulsational stellar code, which is coupled to the LPCODE stellar evolutionary code — see Córsico (2003). In recent years, this pulsational code has been employed in Córsico et al. (2001a) and Córsico & Benvenuto (2002). A modified version of this code has been used to study GW Virgins (Córsico & Althaus, 2006). This code is based on a modification of the general Newton-Raphson technique presented in Kippenhahn et al. (1967). Our numerical pulsation code solves the fourth-order set of equations governing linear, nonradial, adiabatic stellar pulsations in the formulation given in Unno et al. (1989), where x is the independent variable (defined as $x = r/R$ where r is the radial coordinate and R is the stellar radius) and the dependent variables are defined as:

$$y_1 = \frac{\xi_r}{r},$$

$$y_2 = \frac{1}{g\ r}\left(\frac{p^{'}}{\rho} + \Phi^{'}\right),$$

$$y_3 = \frac{1}{g\ r}\ \Phi^{'},$$

$$y_4 = \frac{1}{g}\ \frac{d\Phi^{'}}{dr},$$

$$\omega^2 = \frac{\sigma^2\ R^3}{G\ M_\star}$$

and

$$\begin{aligned}
x\frac{dy_1}{dr} &= (V_g - 3)\ y_1 + \left[\frac{\ell(\ell+1)}{C_1\omega^2} - V_g\right]\ y_2 + V_g\ y_3 \\
x\frac{dy_2}{dr} &= \left(C_1\omega^2 - A^*\right)\ y_1 + (A^* - U + 1)\ y_2 - A^*\ y_3 \\
x\frac{dy_3}{dr} &= (1 - U)\ y_3 + \ y_4 \\
x\frac{dy_4}{dr} &= UA^*\ y_1 + UV_g\ y_2 + [\ell(\ell+1) - UV_g]\ y_3 - U\ y_4.
\end{aligned} \tag{A.3}$$

The boundary conditions are, at the stellar center ($x = 0$):

$$y_1\ C_1\ \omega^2 - \ell\ y_2 = 0, \ell\ y_3 - y_4 = 0, \tag{A.4}$$

and at the stellar surface ($x = 1$):

$$y_1 - y_2 + y_3 = 0, (\ell + 1)\ y_3 + y_4 = 0, \tag{A.5}$$

being the normalization $y_1 = 1$ at $x = 1$ ($x = r/R_*$). The dimensionless Dziembowski's variables (eigenvalue and eigenfunctions) are defined as:

$$\omega_k^2 = \frac{R_*^3}{GM_*}\sigma_k^2, \tag{A.6}$$

and

$$y_1 = \frac{\xi_r}{r},\ y_2 = \frac{1}{gr}\left(\frac{p'}{\rho} + \Phi'\right), \tag{A.7}$$

$$y_3 = \frac{1}{gr}\Phi',\ y_4 = \frac{1}{g}\frac{d\Phi'}{dr}. \tag{A.8}$$

Here, ξ_r is the radial Lagrangian displacement, and p', Φ' are the Eulerian perturbation of the pressure and the gravitational potential, respectively. Pertinent dimensionless coefficients of the pulsation equations are:

$$V_g = \frac{gr}{c^2},\ U = \frac{4\pi\rho r^3}{M_r}, \tag{A.9}$$

$$C_1 = \left(\frac{r}{R}\right)^3\left(\frac{M_*}{M_r}\right),\ A^* = \frac{r}{g}N^2, \tag{A.10}$$

where c is the adiabatic local sound speed and N the Brunt-Väisälä frequency. The remainder symbols are self-explanatory. Once the eigenvalue and eigenfunctions are computed, the code proceeds to evaluate a number of important pulsation quantities, such as the pulsation period, Π_k,

$$\Pi_k = 2\pi/\sigma_k, \tag{A.11}$$

the oscillation kinetic energy, K_k,

$$K_k = \frac{1}{2}(GM_*R_*^2)\omega_k^2 \times \int_0^1 x^2\rho\left[x^2y_1^2 + x^2\frac{\ell(\ell+1)}{(C_1\omega_k^2)^2}y_2^2\right]dx, \tag{A.12}$$

the weight function, W_k,

$$W_k(x) = (4\pi GR_*^2)\frac{x^2\rho^2}{U} \times \left[A^*y_1^2 + V_g\left(y_2 - y_3\right)^2 - \frac{1}{U}\{\ell\left(\ell+1\right)y_3 + y_4\}^2\right], \tag{A.13}$$

the variational period, Π_k^v,

$$\Pi_k^v = \sqrt{\frac{8\pi^2}{GM_*}}\ \frac{K_k^{1/2}}{\omega_k}\left[\int_0^1 W_k(x)\ x^2 dx\right]^{-1/2}, \tag{A.14}$$

and finally, the first-order rotation splitting coefficients, C_k,

$$C_k = \frac{(GM_*R_*^2)}{2K_k}\int_0^1 \frac{x^2\rho}{C_1}\left[2x^2 y_1 y_2 + \frac{x^2}{C_1\omega_k^2}y_2^2\right] dx, \tag{A.15}$$

The rotation splitting of the eigenfrequencies (assuming slow, rigid rotation) can be assesed by means of

$$\sigma_{k,m} = \sigma_k + m(1 - C_k)\Omega \tag{A.16}$$

where Ω is the angular speed of rotation and m the azimutal quantum number.

We refer the reader to Córsico & Benvenuto (2002) and Córsico (2003) for a full description of this technique.

A.2.1 The modified Ledoux treatment

The prescription we follow to assess the run of the Brunt-Väisälä frequency (N) is the so-called "Modified Ledoux treatment" — see Tassoul et al. (1990) — appropriately generalized to include the effects of having three nuclear species (oxygen, carbon and helium) varying in abundance — see Kawaler & Bradley (1994) for additional details. In this numerical treatment the contribution to N from any change in composition is almost completely contained in the Ledoux term B. This fact renders the method particularly useful to infer the relative weight that each chemical transition region have on the mode-trapping properties of the model (Córsico & Althaus, 2006). Specifically, the Brunt-Väisälä frequency is computed as:

$$N^2 = \frac{g^2\ \rho}{p}\ \frac{\chi_{\rm T}}{\chi_\rho}\ (\nabla_{\rm ad} - \nabla + B) \tag{A.17}$$

where

$$B = -\frac{1}{\chi_{\rm T}}\sum_{i=1}^{n-1}\chi_{{\rm X}_i}\frac{d\ln X_i}{d\ln p}, \tag{A.18}$$

being

$$\chi_{\rm T} = \left[\frac{\partial\ln p}{\partial\ln T}\right]_\rho \quad \chi_\rho = \left[\frac{\partial\ln p}{\partial\ln \rho}\right]_T \quad \chi_{{\rm X}_i} = \left[\frac{\partial\ln p}{\partial\ln X_i}\right]_{\rho,T,X_{j\neq i}} \tag{A.19}$$

Bibliography

Alexander, D. R. & Ferguson, J. W., 1994. Low-temperature Rosseland opacities. *ApJ*, **437**, 879–891.

Althaus, L. G. & Benvenuto, O. G., 2000. Diffusion in helium white dwarf stars. *MNRAS*, **317**, 952–964.

Althaus, L. G., Córsico, A. H., Bischoff-Kim, A., Romero, A. D., Renedo, I., García-Berro, E. & Miller Bertolami, M. M., 2010a. New Chemical Profiles for the Asteroseismology of ZZ Ceti Stars. *ApJ*, **717**, 897–907.

Althaus, L. G., Córsico, A. H., Isern, J. & García-Berro, E., 2010b. Evolutionary and pulsational properties of white dwarf stars. *A&A Rev.*, **18**, 471–566.

Althaus, L. G., Córsico, A. H., Torres, S. & García-Berro, E., 2009a. On the origin of white dwarfs with carbon-dominated atmospheres: the case of H1504+65. *A&A*, **494**, 1021–1024.

Althaus, L. G., García-Berro, E., Córsico, A. H., Miller Bertolami, M. M. & Romero, A. D., 2009b. On the Formation of Hot DQ White Dwarfs. *ApJ*, **693**, L23–L26.

Althaus, L. G., García-Berro, E., Isern, J. & Córsico, A. H., 2005a. Mass-radius relations for massive white dwarf stars. *A&A*, **441**, 689–694.

Althaus, L. G., García-Berro, E., Isern, J., Córsico, A. H. & Rohrmann, R. D., 2007. The age and colors of massive white dwarf stars. *A&A*, **465**, 249–255.

Althaus, L. G., García-Berro, E., Renedo, I., Isern, J., Córsico, A. H. & Rohrmann, R. D., 2010c. Evolution of White Dwarf Stars with High-metallicity Progenitors: The Role of ^{22}Ne Diffusion. *ApJ*, **719**, 612–621.

Althaus, L. G., Miller Bertolami, M. M., Córsico, A. H., García-Berro, E. & Gil-Pons, P., 2005b. The formation of DA white dwarfs with thin hydrogen envelopes. *A&A*, **440**, L1–L4.

Althaus, L. G., Panei, J. A., Miller Bertolami, M. M., García-Berro, E., Córsico, A. H., Romero, A. D., Kepler, S. O. & Rohrmann, R. D., 2009c. New Evolutionary Sequences for Hot H-Deficient White Dwarfs on the Basis of a Full Account of Progenitor Evolution. *ApJ*, **704**, 1605–1615.

Althaus, L. G., Panei, J. A., Romero, A. D., Rohrmann, R. D., Córsico, A. H., García-Berro, E. & Miller Bertolami, M. M., 2009d. Evolution and colors of helium-core white dwarf stars with high-metallicity progenitors. *A&A*, **502**, 207–216.

Althaus, L. G., Serenelli, A. M., Córsico, A. H. & Montgomery, M. H., 2003. New evolutionary models for massive ZZ Ceti stars. I. First results for their pulsational properties. *A&A*, **404**, 593–609.

Althaus, L. G., Serenelli, A. M., Panei, J. A., Córsico, A. H., García-Berro, E. & Scóccola, C. G., 2005c. The formation and evolution of hydrogen-deficient post-AGB white dwarfs: The emerging chemical profile and the expectations for the PG 1159-DB-DQ evolutionary connection. *A&A*, **435**, 631–648.

Andreuzzi, G., Richer, H. B., Limongi, M. & Bolte, M., 2002. The white dwarf cooling sequence in the old open cluster NGC 188. *A&A*, **390**, 961–965.

Angulo, C., Arnould, M., Rayet, M., Descouvemont, P., Baye, D. et al., 1999. A compilation of charged-particle induced thermonuclear reaction rates. *Nuclear Physics A*, **656**, 3–183.

Arcoragi, J.-P. & Fontaine, G., 1980. Acoustic fluxes in white dwarfs. *ApJ*, **242**, 1208–1225.

Barrado y Navascués, D., Stauffer, J. R., Bouvier, J. & Martín, E. L., 2001. From the Top to the Bottom of the Main Sequence: A Complete Mass Function of the Young Open Cluster M35. *ApJ*, **546**, 1006–1018.

Bedin, L. R., King, I. R., Anderson, J., Piotto, G., Salaris, M., Cassisi, S. & Serenelli, A., 2008a. Reaching the End of the White Dwarf Cooling Sequence in NGC 6791. *ApJ*, **678**, 1279–1291.

Bedin, L. R., Salaris, M., Piotto, G., Cassisi, S., Milone, A. P., Anderson, J. & King, I. R., 2008b. The Puzzling White Dwarf Cooling Sequence in NGC 6791: A Simple Solution. *ApJ*, **679**, L29–L32.

Bedin, L. R., Salaris, M., Piotto, G., King, I. R., Anderson, J., Cassisi, S. & Momany, Y., 2005. The White Dwarf Cooling Sequence in NGC 6791. *ApJ*, **624**, L45–L48.

Benvenuto, O. G. & Althaus, L. G., 1999. Grids of white dwarf evolutionary models with masses from M=0.1 to 1.2 m_solar. *MNRAS*, **303**, 30–38.

Benvenuto, O. G., Córsico, A. H., Althaus, L. G. & Serenelli, A. M., 2002a. On mode trapping in pulsating DA white dwarf stars. *MNRAS*, **335**, 480–486.

Benvenuto, O. G., Córsico, A. H., Althaus, L. G. & Serenelli, A. M., 2002b. Time-dependent diffusion in pulsating white dwarf stars: asteroseismology of G117-B15A. *MNRAS*, **332**, 399–408.

Benvenuto, O. G., García-Berro, E. & Isern, J., 2004. Asteroseismological bound on Gdot/G from pulsating white dwarfs. *Phys. Rev. D*, **69**(8), 082002.

Bergeron, P., Ruiz, M. T. & Leggett, S. K., 1997. The Chemical Evolution of Cool White Dwarfs and the Age of the Local Galactic Disk. *ApJS*, **108**, 339.

Bergeron, P., Saumon, D. & Wesemael, F., 1995. New model atmospheres for very cool white dwarfs with mixed H/He and pure He compositions. *ApJ*, **443**, 764–779.

Bildsten, L. & Hall, D. M., 2001. Gravitational Settling of ^{22}NE in Liquid White Dwarf Interiors. *ApJ*, **549**, L219–L223.

Bischoff-Kim, A., 2009. Asteroseismological Analysis of Rich Pulsating White Dwarfs. In J. A. Guzik & P. A. Bradley, eds., *American Institute of Physics Conference Series*, vol. 1170 of *American Institute of Physics Conference Series*, 621–624.

Bischoff-Kim, A., Montgomery, M. H. & Winget, D. E., 2008. Fine Grid Asteroseismology of G117-B15A and R548. *ApJ*, **675**, 1505–1511.

Bognár, Z., Paparó, M., Bradley, P. A. & Bischoff-Kim, A., 2009. Characterizing the pulsations of the ZZ Ceti star KUV 02464+3239. *MNRAS*, **399**, 1954–1963.

Bradley, P. & Kleinman, S. J., 1997. Preliminary asteroseismology of G 29-38. In J. Isern, M. Hernanz & E. Garcia-Berro, eds., *White dwarfs*, vol. 214 of *Astrophysics and Space Science Library*, 445.

Bradley, P. A., 1996. Theoretical Models for Asteroseismology of DA White Dwarf Stars. *ApJ*, **468**, 350.

Bradley, P. A., 1998. Asteroseismological Constraints on the Structure of the ZZ Ceti Stars G117-B15A and R548. *ApJS*, **116**, 307.

Bradley, P. A., 2001. Asteroseismological Constraints on the Structure of the ZZ Ceti Stars L19-2 and GD 165. *ApJ*, **552**, 326–339.

Bradley, P. A., 2006. Preliminary seismology of the DA white dwarf G 185-32 . *MmSAI*, **77**, 437.

Brassard, P., Fontaine, G., Wesemael, F. & Hansen, C. J., 1992a. Adiabatic properties of pulsating DA white dwarfs. II - Mode trapping in compositionally stratified models. *ApJS*, **80**, 369–401.

Brassard, P., Fontaine, G., Wesemael, F., Kawaler, S. D. & Tassoul, M., 1991. Adiabatic properties of pulsating DA white dwarfs. I - The treatment of the Brunt-Vaisala frequency and the region of period formation. *ApJ*, **367**, 601–611.

Brassard, P., Fontaine, G., Wesemael, F. & Tassoul, M., 1992b. Adiabatic properties of pulsating DA white dwarfs. IV - an extensive survey of the period structure of evolutionary models. *ApJS*, **81**, 747–794.

Bravo, E., Isern, J., Canal, R. & Labay, J., 1992. On the contribution of Ne-22 to the synthesis of Fe-54 and Ni-58 in thermonuclear supernovae. *A&A*, **257**, 534–538.

Brickhill, A. J., 1991. The pulsations of ZZ Ceti stars. III - The driving mechanism. *MNRAS*, **251**, 673–680.

Burgers, J. M., 1969. *Flow Equations for Composite Gases*.

Calamida, A., Bono, G., Stetson, P. B., Freyhammer, L. M., Piersimoni, A. M. et al., 2009. Strömgren Photometry of Galactic Globular Clusters. II. Metallicity Distribution of Red Giants in ω Centauri. *ApJ*, **706**, 1277–1298.

Carraro, G., Villanova, S., Demarque, P., McSwain, M. V., Piotto, G. & Bedin, L. R., 2006. NGC 6791: An Exotic Open Cluster or the Nucleus of a Tidally Disrupted Galaxy? *ApJ*, **643**, 1151–1159.

Casagrande, L., Flynn, C., Portinari, L., Girardi, L. & Jimenez, R., 2007. The helium abundance and $\Delta Y/\Delta Z$ in lower main-sequence stars. *MNRAS*, **382**, 1516–1540.

Cassisi, S., Potekhin, A. Y., Pietrinferni, A., Catelan, M. & Salaris, M., 2007. Updated Electron-Conduction Opacities: The Impact on Low-Mass Stellar Models. *ApJ*, **661**, 1094–1104.

Castanheira, B. G. & Kepler, S. O., 2008. Seismological studies of ZZ Ceti stars - I. The model grid and the application to individual stars. *MNRAS*, **385**, 430–444.

Castanheira, B. G. & Kepler, S. O., 2009. Seismological studies of ZZ Ceti stars - II. Application to the ZZ Ceti class. *MNRAS*, **396**, 1709–1731.

Catalán, S., Isern, J., García-Berro, E. & Ribas, I., 2008a. The initial-final mass relationship of white dwarfs revisited: effect on the luminosity function and mass distribution. *MNRAS*, **387**, 1693–1706.

Catalán, S., Isern, J., García-Berro, E., Ribas, I., Allende Prieto, C. & Bonanos, A. Z., 2008b. The initial-final mass relationship from white dwarfs in common proper motion pairs. *A&A*, **477**, 213–221.

Caughlan, G. R., Fowler, W. A., Harris, M. J. & Zimmerman, B. A., 1985. Tables of Thermonuclear Reaction Rates for Low-Mass Nuclei ($1 \leq Z \leq 14$). *Atomic Data and Nuclear Data Tables*, **32**, 197.

Córsico, A. H., 2003. *Pulsaciones en estrellas enanas blancas variables ZZ Ceti*. Ph.D. thesis, UNPL.

Córsico, A. H. & Althaus, L. G., 2006. Asteroseismic inferences on GW Virginis variable stars in the frame of new PG 1159 evolutionary models. *A&A*, **454**, 863–881.

Córsico, A. H., Althaus, L. G., Benvenuto, O. G. & Serenelli, A. M., 2002a. The mode trapping properties of full DA white dwarf evolutionary models. *A&A*, **387**, 531–549.

Córsico, A. H., Althaus, L. G., Montgomery, M. H., García-Berro, E. & Isern, J., 2005. New evolutionary models for massive ZZ Ceti stars. II. The effects of crystallization on their pulsational properties. *A&A*, **429**, 277–290.

Córsico, A. H. & Benvenuto, O. G., 2002. A New Code for Nonradial Stellar Pulsations and its Application to Low-Mass, Helium White Dwarfs. *Ap&SS*, **279**, 281–300.

Córsico, A. H., Benvenuto, O. G., Althaus, L. G., Isern, J. & García-Berro, E., 2001a. The potential of the variable DA white dwarf G117-B15A as a tool for fundamental physics. *New Astron.*, **6**, 197–213.

Córsico, A. H., Benvenuto, O. G., Althaus, L. G., Isern, J. & García-Berro, E., 2001b. The potential of the variable DA white dwarf G117-B15A as a tool for fundamental physics. *New Astron.*, **6**, 197–213.

Córsico, A. H., Benvenuto, O. G., Althaus, L. G. & Serenelli, A. M., 2002b. The effects of element diffusion on the pulsational properties of variable DA white dwarf stars. *MNRAS*, **332**, 392–398.

Córsico, A. H., García-Berro, E., Althaus, L. G. & Isern, J., 2004. Pulsations of massive ZZ Ceti stars with carbon/oxygen and oxygen/neon cores. *A&A*, **427**, 923–932.

Deloye, C. J. & Bildsten, L., 2002. Gravitational Settling of ^{22}Ne in Liquid White Dwarf Interiors: Cooling and Seismological Effects. *ApJ*, **580**, 1077–1090.

di Criscienzo, M., D'Antona, F. & Ventura, P., 2010. A detailed study of the main sequence of the globular cluster NGC 6397: can we derive constraints on the existence of multiple populations? *A&A*, **511**, A70.

Diaz-Pinto, A., Garcia-Berro, E., Hernanz, M., Isern, J. & Mochkovitch, R., 1994. The luminosity function of massive white dwarfs. *A&A*, **282**, 86–92.

Dolez, N. & Vauclair, G., 1981. Gravity modes instability in DA white dwarfs. *A&A*, **102**, 375–385.

Dominguez, I., Chieffi, A., Limongi, M. & Straniero, O., 1999. Intermediate-Mass Stars: Updated Models. *ApJ*, **524**, 226–241.

Dominguez, I., Straniero, O., Tornambe, A. & Isern, J., 1996. On the Formation of Massive C-O White Dwarfs: The Lifting Effect of Rotation. *ApJ*, **472**, 783.

Dufour, P., Fontaine, G., Liebert, J., Schmidt, G. D. & Behara, N., 2008. Hot DQ White Dwarfs: Something Different. *ApJ*, **683**, 978–989.

Dufour, P., Liebert, J., Fontaine, G. & Behara, N., 2007. White dwarf stars with carbon atmospheres. *Nature*, **450**, 522–524.

Eisenstein, D. J., Liebert, J., Harris, H. C., Kleinman, S. J., Nitta, A., Silvestri, N., Anderson, S. A., Barentine, J. C., Brewington, H. J., Brinkmann, J., Harvanek, M., Krzesiński, J., Neilsen, Jr., E. H., Long, D., Schneider, D. P. & Snedden, S. A., 2006. A Catalog of Spectroscopically Confirmed White Dwarfs from the Sloan Digital Sky Survey Data Release 4. *ApJS*, **167**, 40–58.

Ferrario, L., Wickramasinghe, D., Liebert, J. & Williams, K. A., 2005. The open-cluster initial-final mass relationship and the high-mass tail of the white dwarf distribution. *MNRAS*, **361**, 1131–1135.

Flynn, C., 2004. Cosmic Helium Production. *PASA*, **21**, 126–128.

Fontaine, G. & Brassard, P., 2008. The Pulsating White Dwarf Stars. *Pub. Ast. Soc. Pacific*, **120**, 1043–1096.

Fontaine, G., Brassard, P. & Bergeron, P., 2001. The Potential of White Dwarf Cosmochronology. *Pub. Ast. Soc. Pacific*, **113**, 409–435.

Fontaine, G., Brassard, P., Bergeron, P. & Wesemael, F., 1992. The case of G226-29 - Evidence for a pulsating DA white dwarf with a thick hydrogen layer? *ApJ*, **399**, L91–L94.

García-Berro, E., Althaus, L. G., Córsico, A. H. & Isern, J., 2008. Gravitational Settling of ^{22}Ne and White Dwarf Evolution. *ApJ*, **677**, 473–482.

Garcia-Berro, E., Hernanz, M., Isern, J. & Mochkovitch, R., 1988a. Properties of high-density binary mixtures and the age of the universe from white dwarf stars. *Nature*, **333**, 642–644.

Garcia-Berro, E., Hernanz, M., Isern, J. & Mochkovitch, R., 1995. The rate of change of the gravitational constant and the cooling of white dwarfs. *MNRAS*, **277**, 801–810.

Garcia-Berro, E., Hernanz, M., Mochkovitch, R. & Isern, J., 1988b. Theoretical white-dwarf luminosity functions for two phase diagrams of the carbon-oxygen dense plasma. *A&A*, **193**, 141–147.

García-Berro, E., Torres, S., Althaus, L. G., Renedo, I., Lorén-Aguilar, P., Córsico, A. H., Rohrmann, R. D., Salaris, M. & Isern, J., 2010. A white dwarf cooling age of 8Gyr for NGC 6791 from physical separation processes. *Nature*, **465**, 194–196.

García-Berro, E., Torres, S., Isern, J. & Burkert, A., 1999. Monte Carlo simulations of the disc white dwarf population. *MNRAS*, **302**, 173–188.

García-Berro, E., Torres, S., Isern, J. & Burkert, A., 2004. Monte Carlo simulations of the halo white dwarf population. *A&A*, **418**, 53–65.

García-Berro, E., Torres, S., Renedo, I., Camacho, J., Althaus, L. G., Córsico, A. H., Salaris, M. & Isern, J., 2011. The white-dwarf cooling sequence of NGC 6791: a unique tool for stellar evolution. *A&A*, **533**, A31.

Goldreich, P. & Wu, Y., 1999. Gravity Modes in ZZ Ceti Stars. I. Quasi-adiabatic Analysis of Overstability. *ApJ*, **511**, 904–915.

Gratton, R., Bragaglia, A., Carretta, E. & Tosi, M., 2006. The Metallicity of the Old Open Cluster NGC 6791. *ApJ*, **642**, 462–469.

Grevesse, N. & Sauval, A. J., 1998. Standard Solar Composition. *Space Sci. Rev.*, **85**, 161–174.

Grundahl, F., Clausen, J. V., Hardis, S. & Frandsen, S., 2008. A new standard: age and distance for the open cluster NGC 6791 from the eclipsing binary member V20. *A&A*, **492**, 171–184.

Guandalini, R., Busso, M., Ciprini, S., Silvestro, G. & Persi, P., 2006. Infrared photometry and evolution of mass-losing AGB stars. I. Carbon stars revisited. *A&A*, **445**, 1069–1080.

Guerrero, J., García-Berro, E. & Isern, J., 2004. Smoothed Particle Hydrodynamics simulations of merging white dwarfs. *A&A*, **413**, 257–272.

Haft, M., Raffelt, G. & Weiss, A., 1994. Standard and nonstandard plasma neutrino emission revisited. *ApJ*, **425**, 222–230.

Hansen, B. M. S., 1998. Old and blue white-dwarf stars as a detectable source of microlensing events. *Nature*, **394**, 860–862.

Hansen, B. M. S., 1999. Cooling Models for Old White Dwarfs. *ApJ*, **520**, 680–695.

Hansen, B. M. S., 2005. White Dwarfs in NGC 6791: Avoiding the Helium Flash. *ApJ*, **635**, 522–526.

Hansen, B. M. S., Anderson, J., Brewer, J., Dotter, A., Fahlman, G. G., Hurley, J., Kalirai, J., King, I., Reitzel, D., Richer, H. B., Rich, R. M., Shara, M. M. & Stetson, P. B., 2007. The White Dwarf Cooling Sequence of NGC 6397. *ApJ*, **671**, 380–401.

Hansen, B. M. S., Brewer, J., Fahlman, G. G., Gibson, B. K., Ibata, R., Limongi, M., Rich, R. M., Richer, H. B., Shara, M. M. & Stetson, P. B., 2002. The White Dwarf Cooling Sequence of the Globular Cluster Messier 4. *ApJ*, **574**, L155–L158.

Hansen, B. M. S. & Liebert, J., 2003. Cool White Dwarfs. *ARA&A*, **41**, 465–515.

Hansen, B. M. S., Richer, H. B., Fahlman, G. G., Stetson, P. B., Brewer, J., Currie, T., Gibson, B. K., Ibata, R., Rich, R. M. & Shara, M. M., 2004. Hubble Space Telescope Observations of the White Dwarf Cooling Sequence of M4. *ApJS*, **155**, 551–576.

Hernanz, M., Garcia-Berro, E., Isern, J., Mochkovitch, R., Segretain, L. & Chabrier, G., 1994. The influence of crystallization on the luminosity function of white dwarfs. *ApJ*, **434**, 652–661.

Herwig, F., Bloecker, T., Schoenberner, D. & El Eid, M., 1997. Stellar evolution of low and intermediate-mass stars. IV. Hydrodynamically-based overshoot and nucleosynthesis in AGB stars. *A&A*, **324**, L81–L84.

Iben, Jr., I. & MacDonald, J., 1985. The effects of diffusion due to gravity and due to composition gradients on the rate of hydrogen burning in a cooling degenerate dwarf. I - The case of a thick helium buffer layer. *ApJ*, **296**, 540–553.

Iben, Jr., I. & MacDonald, J., 1986. The effects of diffusion due to gravity and due to composition gradients on the rate of hydrogen burning in a cooling degenerate dwarf. II - Dependence on initial metallicity and on buffer mass. *ApJ*, **301**, 164–176.

Iglesias, C. A. & Rogers, F. J., 1996. Updated Opal Opacities. *ApJ*, **464**, 943.

Isern, J., García-Berro, E., Althaus, L. G. & Córsico, A. H., 2010. Axions and the pulsation periods of variable white dwarfs revisited. *A&A*, **512**, A86.

Isern, J., García-Berro, E., Hernanz, M. & Chabrier, G., 2000. The Energetics of Crystallizing White Dwarfs Revisited Again. *ApJ*, **528**, 397–400.

Isern, J., Garcia-Berro, E., Hernanz, M., Mochkovitch, R. & Torres, S., 1998. The Halo White Dwarf Population. *ApJ*, **503**, 239.

Isern, J., García-Berro, E., Torres, S. & Catalán, S., 2008. Axions and the Cooling of White Dwarf Stars. *ApJ*, **682**, L109–L112.

Isern, J., Hernanz, M. & Garcia-Berro, E., 1992. Axion cooling of white dwarfs. *ApJ*, **392**, L23–L25.

Isern, J., Hernanz, M., Mochkovitch, R. & Garcia-Berro, E., 1991. The role of the minor chemical species in the cooling of white dwarfs. *A&A*, **241**, L29–L32.

Isern, J., Mochkovitch, R., Garcia-Berro, E. & Hernanz, M., 1997. The Physics of Crystallizing White Dwarfs. *ApJ*, **485**, 308.

Itoh, N., Hayashi, H., Nishikawa, A. & Kohyama, Y., 1996. Neutrino Energy Loss in Stellar Interiors. VII. Pair, Photo-, Plasma, Bremsstrahlung, and Recombination Neutrino Processes. *ApJS*, **102**, 411.

Kalirai, J. S., Bergeron, P., Hansen, B. M. S., Kelson, D. D., Reitzel, D. B., Rich, R. M. & Richer, H. B., 2007. Stellar Evolution in NGC 6791: Mass Loss on the Red Giant Branch and the Formation of Low-Mass White Dwarfs. *ApJ*, **671**, 748–760.

Kalirai, J. S., Hansen, B. M. S., Kelson, D. D., Reitzel, D. B., Rich, R. M. & Richer, H. B., 2008. The Initial-Final Mass Relation: Direct Constraints at the Low-Mass End. *ApJ*, **676**, 594–609.

Kalirai, J. S., Richer, H. B., Hansen, B. M. S., Reitzel, D. & Rich, R. M., 2005. The Dearth of Massive, Helium-rich White Dwarfs in Young Open Star Clusters. *ApJ*, **618**, L129–L132.

Kalirai, J. S., Ventura, P., Richer, H. B., Fahlman, G. G., Durrell, P. R., D'Antona, F. & Marconi, G., 2001. The CFHT Open Star Cluster Survey. III. The White Dwarf Cooling Age of the Rich Open Star Cluster NGC 2099 (M37). *AJ*, **122**, 3239–3257.

Kanaan, A., Nitta, A., Winget, D. E., Kepler, S. O., Montgomery, M. H. et al., 2005. Whole Earth Telescope observations of BPM 37093: A seismological test of crystallization theory in white dwarfs. *A&A*, **432**, 219–224.

Kawaler, S. D. & Bradley, P. A., 1994. Precision asteroseismology of pulsating PG 1159 stars. *ApJ*, **427**, 415–428.

Kepler, S. O., Kleinman, S. J., Nitta, A., Koester, D., Castanheira, B. G., Giovannini, O., Costa, A. F. M. & Althaus, L., 2007. White dwarf mass distribution in the SDSS. *MNRAS*, **375**, 1315–1324.

Kippenhahn, R. & Weigert, A., 1990. *Stellar Structure and Evolution*.

Kippenhahn, R., Weigert, A. & Hofmeister, E., 1967. *Methods in computational physics*.

Kołos, W. & Wolniewicz, L., 1965. Potential-Energy Curves for the $X^1\Sigma^+{}_g$ $b^3\Sigma^+{}_u$ and $C^1\Pi_u$ States of the Hydrogen Molecule. *JChPh*, **43**, 2429–2441.

Kowalski, P. M. & Saumon, D., 2006. Found: The Missing Blue Opacity in Atmosphere Models of Cool Hydrogen White Dwarfs. *ApJ*, **651**, L137–L140.

Kroupa, P., 2001. On the variation of the initial mass function. *MNRAS*, **322**, 231–246.

Kulander, K. C. & Guest, M. F., 1979. Excited electronic states of H_3 and their role in the dissociative recombination of $H_3{}^+$. *Journal of Physics B Atomic Molecular Physics*, **12**, L501–L504.

Lamb, D. Q. & van Horn, H. M., 1975. Evolution of crystallizing pure C-12 white dwarfs. *ApJ*, **200**, 306–323.

Landolt, A. U., 1968. A New Short-Period Blue Variable. *ApJ*, **153**, 151.

Liebert, J., Bergeron, P. & Holberg, J. B., 2005. The Formation Rate and Mass and Luminosity Functions of DA White Dwarfs from the Palomar Green Survey. *ApJS*, **156**, 47–68.

Lind, K., Charbonnel, C., Decressin, T., Primas, F., Grundahl, F. & Asplund, M., 2011. Tracing the evolution of NGC 6397 through the chemical composition of its stellar populations. *A&A*, **527**, A148.

Lorén-Aguilar, P., Isern, J. & García-Berro, E., 2009. High-resolution smoothed particle hydrodynamics simulations of the merger of binary white dwarfs. *A&A*, **500**, 1193–1205.

Lugaro, M., Herwig, F., Lattanzio, J. C., Gallino, R. & Straniero, O., 2003. s-Process Nucleosynthesis in Asymptotic Giant Branch Stars: A Test for Stellar Evolution. *ApJ*, **586**, 1305–1319.

Magni, G. & Mazzitelli, I., 1979. Thermodynamic properties and equations of state for hydrogen and helium in stellar conditions. *A&A*, **72**, 134–147.

Marigo, P., 2002. Asymptotic Giant Branch evolution at varying surface C/O ratio: effects of changes in molecular opacities. *A&A*, **387**, 507–519.

Marigo, P. & Aringer, B., 2009. Low-temperature gas opacity. ÆSOPUS: a versatile and quick computational tool. *A&A*, **508**, 1539–1569.

Marigo, P., Girardi, L., Chiosi, C. & Wood, P. R., 2001. Zero-metallicity stars. I. Evolution at constant mass. *A&A*, **371**, 152–173.

Meng, X., Chen, X. & Han, Z., 2008. Initial-final mass relationship for stars of different metallicities. *A&A*, **487**, 625–635.

Mestel, L., 1952. On the theory of white dwarf stars. I. The energy sources of white dwarfs. *MNRAS*, **112**, 583.

Metcalfe, T. S., 2003. White Dwarf Asteroseismology and the $^{12}C(\alpha,\gamma)^{16}O$ Rate. *ApJ*, **587**, L43–L46.

Metcalfe, T. S., Montgomery, M. H. & Kanaan, A., 2004. Testing White Dwarf Crystallization Theory with Asteroseismology of the Massive Pulsating DA Star BPM 37093. *ApJ*, **605**, L133–L136.

Metcalfe, T. S., Montgomery, M. H. & Kawaler, S. D., 2003. Probing the core and envelope structure of DBV white dwarfs. *MNRAS*, **344**, L88–L92.

Miller Bertolami, M. M. & Althaus, L. G., 2006. Full evolutionary models for PG 1159 stars. Implications for the helium-rich O(He) stars. *A&A*, **454**, 845–854.

Miller Bertolami, M. M., Althaus, L. G., Unglaub, K. & Weiss, A., 2008. Modeling He-rich subdwarfs through the hot-flasher scenario. *A&A*, **491**, 253–265.

Milone, A. P., Bedin, L. R., Piotto, G., Anderson, J., King, I. R., Sarajedini, A., Dotter, A., Chaboyer, B., Marín-Franch, A., Majewski, S., Aparicio, A., Hempel, M., Paust, N. E. Q., Reid, I. N., Rosenberg, A. & Siegel, M., 2008. The ACS Survey of Galactic Globular Clusters. III. The Double Subgiant Branch of NGC 1851. *ApJ*, **673**, 241–250.

Milone, A. P., Piotto, G., Bedin, L. R., Bellini, A., Marino, A. F. & Momany, Y., 2010. Multiple stellar populations in Galactic globular clusters: observational evidence. In S. Boissier, M. Heydari-Malayeri, R. Samadi & D. Valls-Gabaud, eds., *SF2A-2010: Proceedings of the Annual meeting of the French Society of Astronomy and Astrophysics*, 319.

Montgomery, M. H., Klumpe, E. W., Winget, D. E. & Wood, M. A., 1999. Evolutionary Calculations of Phase Separation in Crystallizing White Dwarf Stars. *ApJ*, **525**, 482–491.

Mullally, F., Winget, D. E., De Gennaro, S., Jeffery, E., Thompson, S. E., Chandler, D. & Kepler, S. O., 2008. Limits on Planets around Pulsating White Dwarf Stars. *ApJ*, **676**, 573–583.

Origlia, L., Valenti, E., Rich, R. M. & Ferraro, F. R., 2006. High-Resolution Infrared Spectroscopy of the Old Open Cluster NGC 6791. *ApJ*, **646**, 499–504.

Pech, D. & Vauclair, G., 2006. The ZZ Ceti star G 185-32: new insight from asteroseismology. *A&A*, **453**, 219–227.

Pech, D., Vauclair, G. & Dolez, N., 2006. Asteroseismological constraints on the structure of the ZZ Ceti star HL Tau 76. *A&A*, **446**, 223–235.

Petsalakis, I. D., Theodorakopoulos, G., Wright, J. S. & Hamilton, I. P., 1988. The Rydberg states of FH_2. *JChPh*, **88**, 7633–7637.

Pfeiffer, B., Vauclair, G., Dolez, N., Chevreton, M., Fremy, J.-R. et al., 1996. Whole Earth Telescope observations and seismological analysis of the cool ZZ Ceti star GD 154. *A&A*, **314**, 182–190.

Pietrinferni, A., Cassisi, S., Salaris, M. & Castelli, F., 2004. A Large Stellar Evolution Database for Population Synthesis Studies. I. Scaled Solar Models and Isochrones. *ApJ*, **612**, 168–190.

Piotto, G., Bedin, L. R., Anderson, J., King, I. R., Cassisi, S., Milone, A. P., Villanova, S., Pietrinferni, A. & Renzini, A., 2007. A Triple Main Sequence in the Globular Cluster NGC 2808. *ApJ*, **661**, L53–L56.

Prada Moroni, P. G. & Straniero, O., 2002. Calibration of White Dwarf Cooling Sequences: Theoretical Uncertainty. *ApJ*, **581**, 585–597.

Prada Moroni, P. G. & Straniero, O., 2007. White dwarf cooling sequences. II. Luminosity functions. *A&A*, **466**, 1043–1051.

Prada Moroni, P. G. & Straniero, O., 2009. Very low-mass white dwarfs with a C-O core. *A&A*, **507**, 1575–1583.

Press, W. H., Flannery, B. P. & Teukolsky, S. A., 1986. *Numerical recipes. The art of scientific computing*.

Renedo, I., Althaus, L. G., Miller Bertolami, M. M., Romero, A. D., Córsico, A. H., Rohrmann, R. D. & García-Berro, E., 2010. New Cooling Sequences for Old White Dwarfs. *ApJ*, **717**, 183–195.

Richer, H. B., Dotter, A., Hurley, J., Anderson, J., King, I., Davis, S., Fahlman, G. G., Hansen, B. M. S., Kalirai, J., Paust, N., Rich, R. M. & Shara, M. M., 2008. Deep Advanced Camera for Surveys Imaging in the Globular Cluster NGC 6397: the Cluster Color-Magnitude Diagram and Luminosity Function. *AJ*, **135**, 2141–2154.

Richer, H. B., Fahlman, G. G., Ibata, R. A., Pryor, C., Bell, R. A., Bolte, M., Bond, H. E., Harris, W. E., Hesser, J. E., Holland, S., Ivanans, N., Mandushev, G., Stetson, P. B. & Wood, M. A., 1997. White Dwarfs in Globular Clusters: Hubble Space Telescope Observations of M4. *ApJ*, **484**, 741.

Richer, H. B., Fahlman, G. G., Rosvick, J. & Ibata, R., 1998. The White Dwarf Cooling Age of M67. *ApJ*, **504**, L91.

Ritossa, C., Garcia-Berro, E. & Iben, Jr., I., 1996. On the Evolution of Stars That Form Electron-degenerate Cores Processed by Carbon Burning. II. Isotope Abundances and Thermal Pulses in a 10 M_{sun} Model with an ONe Core and Applications to Long-Period Variables, Classical Novae, and Accretion-induced Collapse. *ApJ*, **460**, 489.

Ritossa, C., García-Berro, E. & Iben, Jr., I., 1999. On the Evolution of Stars that Form Electron-degenerate Cores Processed by Carbon Burning. V. Shell Convection Sustained by Helium Burning, Transient Neon Burning, Dredge-out, URCA Cooling, and Other Properties of an 11 M_solar Population I Model Star. *ApJ*, **515**, 381–397.

Roach, A. C. & Kuntz, P. J., 1986. Unified large basis set diatomics-in-molecules models for ground and excited states of H_3. *JChPh*, **84**, 822–832.

Rohrmann, R. D., Althaus, L. G. & Kepler, S. O., 2011. Lyman α wing absorption in cool white dwarf stars. *MNRAS*, **411**, 781–791.

Rohrmann, R. D., Serenelli, A. M., Althaus, L. G. & Benvenuto, O. G., 2002. Improved synthetic spectra of helium-core white dwarf stars. *MNRAS*, **335**, 499–511.

Rubin, K. H. R., Williams, K. A., Bolte, M. & Koester, D., 2008. The White Dwarf Population in NGC 1039 (M34) and the White Dwarf Initial-Final Mass Relation. *AJ*, **135**, 2163–2176.

Salaris, M., Cassisi, S., Pietrinferni, A., Kowalski, P. M. & Isern, J., 2010. A Large Stellar Evolution Database for Population Synthesis Studies. VI. White Dwarf Cooling Sequences. *ApJ*, **716**, 1241–1251.

Salaris, M., Dominguez, I., Garcia-Berro, E., Hernanz, M., Isern, J. & Mochkovitch, R., 1997. The Cooling of CO White Dwarfs: Influence of the Internal Chemical Distribution. *ApJ*, **486**, 413.

Salaris, M., García-Berro, E., Hernanz, M., Isern, J. & Saumon, D., 2000. The Ages of Very Cool Hydrogen-rich White Dwarfs. *ApJ*, **544**, 1036–1043.

Salaris, M., Serenelli, A., Weiss, A. & Miller Bertolami, M., 2009. Semi-empirical White Dwarf Initial-Final Mass Relationships: A Thorough Analysis of Systematic Uncertainties Due to Stellar Evolution Models. *ApJ*, **692**, 1013–1032.

Sarna, M. J., Antipova, J. & Ergma, E., 1999. Cooling curves and initial models for low-mass white dwarfs ($< 0.25 M_{\odot}$) with helium core. In S.-E. Solheim & E. G. Meistas, eds., *11th European Workshop on White Dwarfs*, vol. 169 of *Astronomical Society of the Pacific Conference Series*, 400.

Schröder, K.-P. & Cuntz, M., 2005. A New Version of Reimers' Law of Mass Loss Based on a Physical Approach. *ApJ*, **630**, L73–L76.

Segretain, L., 1996. Three-body crystallization diagrams and the cooling of white dwarfs. *A&A*, **310**, 485–488.

Segretain, L. & Chabrier, G., 1993. Crystallization of binary ionic mixtures in dense stellar plasmas. *A&A*, **271**, L13.

Segretain, L., Chabrier, G., Hernanz, M., Garcia-Berro, E., Isern, J. & Mochkovitch, R., 1994. Cooling theory of crystallized white dwarfs. *ApJ*, **434**, 641–651.

Siess, L., 2007. Evolution of massive AGB stars. II. model properties at non-solar metallicity and the fate of Super-AGB stars. *A&A*, **476**, 893–909.

Stevenson, D. J., 1980. The condensed matter physics of planetary interiors. *Journal de Physique*, **41**, C53.

Straniero, O., Domínguez, I., Imbriani, G. & Piersanti, L., 2003. The Chemical Composition of White Dwarfs as a Test of Convective Efficiency during Core Helium Burning. *ApJ*, **583**, 878–884.

Tassoul, M., Fontaine, G. & Winget, D. E., 1990. Evolutionary models for pulsation studies of white dwarfs. *ApJS*, **72**, 335–386.

Torres, S., García-Berro, E., Burkert, A. & Isern, J., 2002. High-proper-motion white dwarfs and halo dark matter. *MNRAS*, **336**, 971–978.

Tremblay, P.-E. & Bergeron, P., 2008. The Ratio of Helium- to Hydrogen-Atmosphere White Dwarfs: Direct Evidence for Convective Mixing. *ApJ*, **672**, 1144–1152.

Twarog, B. A., Carraro, G. & Anthony-Twarog, B. J., 2011. Evidence for Extended Star Formation in the Old, Metal-Rich Open Cluster, NGC 6791? *ApJ*, **727**, L7.

Unglaub, K. & Bues, I., 2000. The chemical evolution of hot white dwarfs in the presence of diffusion and mass loss. *A&A*, **359**, 1042–1058.

Unno, W., Osaki, Y., Ando, H., Saio, H. & Shibahashi, H., 1989. *Nonradial oscillations of stars*.

van Horn, H. M., 1968. Crystallization of White Dwarfs. *ApJ*, **151**, 227.

van Loon, J. T., Boyer, M. L. & McDonald, I., 2008. Spitzer Space Telescope Evidence in NGC 6791: No Super Mass Loss at Supersolar Metallicity to Explain Helium White Dwarfs? *ApJ*, **680**, L49–L52.

Vassiliadis, E. & Wood, P. R., 1993. Evolution of low- and intermediate-mass stars to the end of the asymptotic giant branch with mass loss. *ApJ*, **413**, 641–657.

von Hippel, T. & Gilmore, G., 2000. The White Dwarf Cooling Age of the Open Cluster NGC 2420. *AJ*, **120**, 1384–1395.

von Hippel, T., Jefferys, W. H., Scott, J., Stein, N., Winget, D. E., De Gennaro, S., Dam, A. & Jeffery, E., 2006. Inverting Color-Magnitude Diagrams to Access Precise Star Cluster Parameters: A Bayesian Approach. *ApJ*, **645**, 1436–1447.

Weiss, A., Cassisi, S., Schlattl, H. & Salaris, M., 2000. Evolution of Low-Mass Metal-Free Stars including Effects of Diffusion and External Pollution. *ApJ*, **533**, 413–423.

Weiss, A. & Ferguson, J. W., 2009. New asymptotic giant branch models for a range of metallicities. *A&A*, **508**, 1343–1358.

Winget, D. E., Hansen, C. J., Liebert, J., van Horn, H. M., Fontaine, G., Nather, R. E., Kepler, S. O. & Lamb, D. Q., 1987. An independent method for determining the age of the universe. *ApJ*, **315**, L77–L81.

Winget, D. E. & Kepler, S. O., 2008. Pulsating White Dwarf Stars and Precision Asteroseismology. *ARA&A*, **46**, 157–199.

Winget, D. E., Kepler, S. O., Campos, F., Montgomery, M. H., Girardi, L., Bergeron, P. & Williams, K., 2009. The Physics of Crystallization From Globular Cluster White Dwarf Stars in NGC 6397. *ApJ*, **693**, L6–L10.

Winget, D. E., van Horn, H. M. & Hansen, C. J., 1981. The nature of the ZZ Ceti oscillations - Trapped modes in compositionally stratified white dwarfs. *ApJ*, **245**, L33–L36.

Winget, D. E., van Horn, H. M., Tassoul, M., Fontaine, G., Hansen, C. J. & Carroll, B. W., 1982. Hydrogen-driving and the blue edge of compositionally stratified ZZ Ceti star models. *ApJ*, **252**, L65–L68.

Wood, M. A., 1992. Constraints on the age and evolution of the Galaxy from the white dwarf luminosity function. *ApJ*, **386**, 539–561.

Wood, M. A., 1995. Theoretical White Dwarf Luminosity Functions: DA Models. In D. Koester & K. Werner, ed., *White Dwarfs*, vol. 443 of *Lecture Notes in Physics, Berlin Springer Verlag*, 41.